

2016-01-01

Investigation Of TI-6AL-4V Alloy Response To Atmospheric Re-Entry Exposure

Jessica Lynn Buckner

University of Texas at El Paso, jlmorris90@gmail.com

Follow this and additional works at: https://digitalcommons.utep.edu/open_etd



Part of the [Materials Science and Engineering Commons](#), and the [Mechanics of Materials Commons](#)

Recommended Citation

Buckner, Jessica Lynn, "Investigation Of TI-6AL-4V Alloy Response To Atmospheric Re-Entry Exposure" (2016). *Open Access Theses & Dissertations*. 613.

https://digitalcommons.utep.edu/open_etd/613

This is brought to you for free and open access by DigitalCommons@UTEP. It has been accepted for inclusion in Open Access Theses & Dissertations by an authorized administrator of DigitalCommons@UTEP. For more information, please contact lweber@utep.edu.

INVESTIGATION OF TI-6AL-4V ALLOY RESPONSE TO ATMOSPHERIC
RE-ENTRY EXPOSURE

JESSICA LYNN BUCKNER

Doctoral Program in Materials, Science, and Engineering

APPROVED:

Stephen Stafford, Ph.D., Chair

David Roberson, Ph.D.

Stella Quinones, Ph.D.

Russell Chianelli, Ph.D.

Charles Ambler, Ph.D.
Dean of the Graduate School

Copyright ©

by

Jessica Lynn Buckner

2016

Dedication

For my parents and brother.

INVESTIGATION INTO TI-6AL-4V ALLOY RESPONSE TO ATMOSPHERIC RE-ENTRY EXPOSURE

by

JESSICA LYNN BUCKNER, B.S. Metallurgical and Materials Engineering

DISSERTATION

Presented to the Faculty of the Graduate School of

The University of Texas at El Paso

in Partial Fulfillment

of the Requirements

for the Degree of

DOCTOR OF PHILOSOPHY

Department of Metallurgical, Materials, and Biomedical Engineering

THE UNIVERSITY OF TEXAS AT EL PASO

December 2016

Acknowledgements

It has been my honor to work with Dr. Stephen Stafford as my dissertation chair as I progressed through my research. His patience, input, and support have been a huge part of my success, and I cannot thank him enough. His expertise in titanium and failure analysis were instrumental during my tenure at UTEP, on par with his kind words and welcoming nature. I would also like to thank John “Danny” Olivas for bringing this exciting work to UTEP, and reminding me to always “lean forward”. Darren Cone contributed tremendously to this work, sharing his knowledge of materials and space conditions, and acting as a technical review through the stages of my research and writing. I would like to thank him for the countless hours spent in meetings and always maintaining an open door policy, which led me to many “a-ha” moments. I would like to thank Dr. Roberson, Dr. Quinones, and Dr. Chianelli for serving on my committee. I would like to acknowledge the Metallurgical, Materials, and Biomedical Engineering (MMBME) Department, which I have called home for the past several years, for their support and guidance. I would like to thank the MMBME department, the SMART grant sponsored through the American Society for Engineering Education (ASEE), the Center for Advancement of Space Safety and Mission Assurance Research (CASSMAR), and the various private organizations that provided funding and financial support for tuition, research, and conferences. Thank you to the Herrera, Stafford, and Associates (HSA) team for assistance with laboratory services. I would also like to acknowledge Mike Ciannilli and Rick Russell at Kennedy Space Center who provided support and access to *Columbia* artifacts.

Personally, I would like to thank my parents and older brother for always teaching me that education was important and to always fight for my goals. Last but not least, I would like to thank my husband, who has supported me and lifted me up, even when I was at my wits end. It was with his understanding and support that I pushed past a masters and completed a Ph.D.

Abstract

Ti-6Al-4V is a widely used aerospace alloy for its high strength-to-weight ratio and high operating temperature properties. Despite widespread use, titanium and its alloys have been shown to ignite in oxygen and nitrogen rich test streams. The reactivity of titanium is attributed to the high solubility for oxygen that increases with temperature, accelerating the oxidation rate and resulting in a combustion reaction. When introduced to the monatomic oxygen rich and high enthalpy re-entry environment, Ti-6Al-4V X-link components from the space shuttle *Columbia* exhibited accelerated oxidation and combustion behavior. Ti-6Al-4V metal plates tested in the simulated re-entry environment of an arc-jet facility have also exhibited ignition and combustion responses. A forensic material characterization study of the X-links and arc-jet samples is necessary to gain a better understanding of the material response in the dynamic and extreme environment of re-entry.

Materials characterization methods, in the form of microstructural analysis, scanning electron microscopy, energy dispersive X-ray spectroscopy, X-ray diffraction, and microhardness testing, are used to identify the current state of the degraded Ti-6Al-4V material and glean knowledge about the alloy response during re-entry. Data from X-link components is compared to the Ti-6Al-4V samples previously tested in the simulated re-entry arc-jet facility conditions. Several similarities in microstructural features and oxide compound detection suggest that qualitative and quantitative conclusions can be drawn from comparison of actual and simulated re-entry conditions. Furthermore, subtleties between oxidation, ignition, and combustion reaction thresholds were identified. A thorough materials characterization of these materials will yield insight into the discrimination between different material responses of titanium alloys. Widespread use of titanium alloys in space vehicles warrants a thorough characterization of their potential failure modes to help ensure the safe and reliable operation of future spaceflight vehicles.

Table of Contents

Acknowledgements	v
Abstract	vi
Table of Contents	vii
List of Tables	ix
List of Figures	x
Chapter 1: Introduction and Presented Published Papers	1
1.1 Background	1
1.2 Justification	5
1.3 Published Works	7
Chapter 2: Literature Review	10
2.1 Characteristics of Ti-6Al-4V	10
2.2 Oxidation of Titanium.....	15
2.3 Ignition and combustion of Titanium	18
2.4 Particulate Combustion of Titanium	26
Chapter 3: Experimental Methods	31
3.1 Primary Sectioning of X-links	31
3.2 Secondary Sectioning of X-links	32
3.3 Sectioning of arc-jet samples	34
6.1.1 Arc-jet Supplementary Data	35
3.4 Heat Treatment Study	39
Chapter 4: Materials Characterization of the Oxidation and Combustion Behavior of Ti-6Al-4V X-links from the Space Shuttle <i>Columbia</i>	40
4.1 Introduction	40
4.2 Methods.....	43
4.3 Results and Discussion	43
4.4 Conclusions	53
4.5 Acknowledgements	54

Chapter 5: Investigation into the response of Ti-6Al-4V alloy to atmospheric	
re-entry exposure	55
5.1 Introduction	55
5.2 Methods	59
5.3 Results	61
5.4 Conclusions	78
5.5 Acknowledgements	80
Chapter 6: Results and Discussion	81
6.1 X-link Results	81
6.2 Arc-jet Results	96
Chapter 7: Heat Treatment Study Results	109
7.1. Microstructural Features	110
7.2 Microhardness Testing	113
7.3 Summary/Findings	115
Chapter 8: Conclusions	116
8.1 Summary and Conclusions	116
8.2 Recommendations and Future Work	123
References	125
Appendix A	131
Appendix B	133
Vita	135

List of Tables

Table 2.1. Properties of Ti-6Al-4V as they relate to combustion. Data for pure titanium retrieved from [23], Ti-6Al-4V from [9].....	14
Table 2.2. Physical properties of common titanium oxides. Data retrieved from matweb.com...	17
Table 2.3. Ignition temperatures of bulk Ti and Ti alloys.	25
Table 3.1. Test matrix for chosen samples.	35
Table 5.1. Nomenclature of samples discussed in paper.	60
Table 5.2. Average microhardness and population standard deviation for samples 1-4.	78
Table 6.1. Locations of data discussion of X-link and arc-jet samples in dissertation.....	81
Table 6.2. Averages microhardness values and population standard deviation for sections D.2, E.2, and G.1.	96
Table 7.1. Test matrix for heat treatment study.	110

List of Figures

Figure 1.1. Schematic of configuration of X-links within the shuttle. Adapted from [3].	3
Figure 1.2. Top view as-received photographic documentation of the recovered X-links.	3
Figure 1.3. The three different classifications of material response observed in arc-jet testing.	4
Figure 1.4. Arc-jet classifications of material response as they relate to enthalpy and dynamic pressure. Adapted from [7].	5
Figure 2.1. Illustration of the HCP α and BCC β unit cells. Adapted from [20].	13
Figure 2.2. The pseudo-binary phase diagram of Ti-6%Al with additions of vanadium. Vertical line corresponds to a composition of Ti-6%Al-4%V, indicating approximate β -transus temperature of 1950°F. Adapted from [21].	13
Figure 2.3. Microstructure of two-phase Ti-6Al-4V alloy: a) martensitic, b) globular, c) necklace, d) lamellar, e) bimodal. Adapted from [22].	14
Figure 2.4. The titanium rich portion of the titanium-oxygen phase diagram. Adapted from [32].	17
Figure 2.5. The titanium rich portion of the titanium-nitrogen phase diagram. Adapted from [33].	18
Figure 3.1. Primary sectioning of port (a) and starboard (b) X-links, top view.	32
Figure 3.2. High resolution images of starboard pieces D (a), E (b), and G (c).	33
Figure 3.3. High resolution images of arc-jet specimens 8 (a), 16 (b), 17 (c), and 28 (d).	35
Figure 3.4. Test article configuration schematic. Adapted from [7].	36
Figure 3.5. Insertion time vs. sample temperature data for Run 1806, Specimen 8. Adapted from data files from [7].	37
Figure 3.6. Insertion time vs. sample temperature data for Run 1808, Specimen 16. Adapted from data files from [7].	37
Figure 3.7. Insertion time vs. sample temperature data for Run 1811, Specimen 17. Adapted from data files from [7].	38
Figure 3.8. Insertion time vs. sample temperature data for Run 1813, Specimen 28. Adapted from data files from [7].	38
Figure 4.1. The X-links as recovered, top view, with box indicating burn through in the flange. From [3].	41
Figure 4.2. Top view of Regions A (left) and B (right).	43
Figure 4.3. a) Secondary electron image of blue-tinted region with boxed area indicating EDS scan area; b) EDS spectrum obtained from the blue-tinted region	44
Figure 4.4. Inboard (a) and outboard (b) microstructures. Kroll's reagent.	45
Figure 4.5. a) Optical image of deposition layer (Kroll's); and, b) Backscattered electron image of deposition layering in Region A (boxes indicating selected areas for EDS spot analysis).	47
Figure 4.6. EDS spectra from a) Scan One, and b) Scan Two from Region A.	48
Figure 4.7. a) Secondary electron image of porous surfaces resembling shrinkage porosity from surface, top surface and b) Secondary electron image of porosity, top surface.	49
Figure 4.8. Inboard (a) and outboard (b) microstructures from Region B. Kroll's reagent.	51
Figure 4.9. Backscattered electron image of outboard deposit (b), with higher magnification image of porous layer surrounding the large inclusion particles.	52
Figure 4.10. EDS spectra from a) Scan One, and b) Scan Two from Region B.	53

Figure 5.1. As-received photographic documentation of the port and starboard X-links.....	59
Figure 5.2. The three different classifications of material response observed from arc-jet testing.	59
Figure 5.3. Starboard X-link region of interest with numbered sections.....	60
Figure 5.4. Class II (a) and Class III (b) arc-jet samples.	60
Figure 5.5. Complementary microstructures through thickest section of port (a) and starboard (b) X-links.....	65
Figure 5.6. Initial microstructural state of the arc-jet samples.	66
Figure 5.7. Forward facing flow microstructures for starboard X-link section 1 (a), starboard X- link section 2 (b), arc-jet sample Class II (c), and arc-jet sample Class III (d).	68
Figure 5.8. Back facing flow microstructures for starboard X-link section 1 (a), starboard X-link section 2 (b), arc-jet sample Class II (c), and arc-jet sample Class III (d).....	70
Figure 5.9. Backscattered electron images of granular features coalescing to form a solid layer in X-link sample 2 (a) and arc-jet sample 3 (b).	72
Figure 5.10. EDS spectrum of granular features in X-link sample 1 (a) and arc-jet sample 3 (b).	73
Figure 5.11. X-ray diffraction patterns for the less thermally degraded X-link sample 2 and arc- jet sample 3 (a) and the more thermally degraded X-link sample 1 and arc-jet sample 4 (b).	75
.....	77
Figure 5.12. Microhardness values traversing from forward to back facing flow side for samples 1 and 2 (a) and samples 3 and 4 (b).	77
Figure 6.1. Secondary sectioning of section E.....	82
Figure 6.2. Secondary sectioning of section G.	83
Figure 6.3. Microstructure of section E.3, showing martensitic α within large prior β grains. ...	84
Figure 6.4. Microstructural features of section G.1 at the inboard (a) and outboard (b) sides.	86
Figure 6.5. Microstructure of the Ti-6Al-4V material at the titanium/MP35N fastener interface.	87
Figure 6.6. Backscattered electron image of silicon rich embedded particle in section E.3 (a) and EDS spectrum of boxed area (b).	88
Figure 6.7. Backscattered electron image of section G.1 inboard side deposit (a), with white boxed area indicating location of zoomed image in (b). Black boxes indicate locations of EDS scans.	90
Figure 6.8. EDS spectra of section G.1 for box 1, porous material in Figure 6.7a (a) and box 2, granular features in Figure 6.7b (b).	91
Figure 6.9. Location of XRD data collection (a) and diffraction patterns for section E.2 (b).	92
Figure 6.10. Diffraction pattern for section E.3.	93
Figure 6.11. Diffraction patterns for the inboard (bottom) and outboard (top) side of section G.1.	94
Figure 6.12. Traversing microhardness testing results for sections D.2, E.2, and G.1	95
Figure 6.13. Microstructural features of the leading edge (a) and trailing edge (b) of Class II arc- jet specimen 16.	97
Figure 6.14. Microstructural features of the leading edge (a) and trailing edge (b) of Class III arc- jet specimen 28.	98
Figure 6.15. Backscattered electron microscope images of Class II arc-jet specimen 16, with close-up of (a) in (b).	100

Figure 6.16. EDS spectra of Class II arc-jet specimen 16 with box 1, intergranular deposit (a) and box 2, granular features (b) in Figure 6.15b.....	101
Figure 6.17. Backscattered electron microscope images of Class II arc-jet specimen 17, with arrow in (a) indicating location of (b).....	103
Figure 6.18. . EDS spectra of Class II arc-jet specimen 17 with box 1, star-like features (a) and box 2, granular features (b) in Figure 6.15b.	104
Figure 6.19. Backscattered electron image of star-like morphology (a) granular features in both (a) and (b) in Class III arc-jet specimen 28.....	105
Figure 6.20. EDS spectra for Class III arc-jet specimen 28 of box 1, star-like solidification features in Figure 6.5a (a) and box 2, granular top layer in Figure 6.5b (b).....	106
Figure 6.21. Diffraction patterns for Class II arc-jet specimens 8 and 16.	107
Figure 6.22. Diffraction patterns Class III arc-jet specimens 17 and 28.	108
Figure 7.1. Microstructural features of samples in heat treatment study.....	113
Figure 7.2. Average microhardness readings of the heat treated samples.	114
Figure 7.3. Plot showing average microhardness readings versus low and high reading from the two samples analyzed per heat treatment.....	115
Figure 8.1. Suggested temperature map of the X-links based on microstructural features observed at the inboard side.	118
Figure 8.2. Suggested temperature map of the X-links based on microstructural features observed at the outboard side.	119

Chapter 1: Introduction and Presented Published Papers

1.1 BACKGROUND

On February 1st, 2003, NASA's Space Shuttle *Columbia* endured a catastrophic failure during re-entry into Earth's atmosphere. Ultimately, all seven crew members lost their lives in this tragic event. Root-cause analysis determined that a breach of the reinforced carbon-carbon (RCC) leading edge of the port wing was caused by a piece of insulating foam that detached from the external fuel tank during lift-off. This breach allowed superheated gas ingestion into the vehicle during re-entry, which ultimately degraded the substructural components and integrity of the space shuttle [1].

Following reconstruction of *Columbia*, evidence suggested that the widely used aerospace alloy, Ti-6Al-4V, exhibited an accelerated degradation believed to be caused by oxidation, ignition, and combustion reactions intensified by exposure to the monatomic oxygen rich, high enthalpy conditions of the re-entry environment. Scientific interest promoted the testing of Ti-6Al-4V plates in the simulated re-entry environment of the arc-jet. These experiments also demonstrated a propensity of Ti-6Al-4V to exhibit accelerated oxidation, ignition, and combustion behavior in extreme conditions. Little research into the material state and properties after exposure to these environments has been documented, thus a detailed materials characterization study was designed to better understand the complexities of material response. A forensic analysis of the material exposed to the actual re-entry environment *Columbia* endured and the simulated re-entry environment of the arc-jet is necessary to discriminate between specific re-entry conditions that can result in catastrophic material reactions and reduction in structural integrity of space vehicles.

1.1.1 Environmental Conditions

The re-entry environment is a monatomic oxygen rich, low pressure, and high enthalpy environment. It is highly aggressive and dynamic. Exact temperature and pressure conditions of the re-entry environment are dependent on altitude. In terms of vertical temperature, there are

four atmospheric layers [2]. In order of increasing altitude are the troposphere, stratosphere, mesosphere, and thermosphere. Modeling results published in the *Columbia* Crew Survival Report by NASA indicate that breakup of *Columbia* occurred in the mesosphere, between 180-210 thousand feet altitude [3]. In the mesosphere, low temperatures prevail and molecular oxygen and nitrogen still compose 99% of the air, with virtually the same mixings as air at sea level (78% N₂, 20.9% O₂, 1.1% other) [2]. The high velocities produced by vehicle deceleration can result in the dissociation of molecular O₂ and N₂ gases, converting the species to their atomic forms. Atomic nitrogen and oxygen are more reactive than their molecular forms and produce a more aggressive environment in which oxidation and combustion are accelerated.

1.1.2 X-link Background

The X-links, also known as crew module attachment fittings, are a substructural component composed of Ti-6Al-4V that connected the crew module, forward fuselage, and midbody structures of the vehicle in the longitudinal direction. There are two X-links, one each for the port and starboard side of the vehicle. Figure 1.1 illustrates the configuration of the X-links within the shuttle. The X-links were secured to the shuttle structures with fasteners made of MP35N, a nickel-cobalt-chromium-molybdenum alloy trademarked by SPS technologies. The top view of the as-received port and starboard X-links as configured within the shuttle are shown in Figure 1.2. Relative to the port X-link, the starboard X-link exhibited more mass loss, discoloration, and is missing the aft-most fastener. The fastener heads exhibit evidence of exposure to forward-to-aft flow conditions, while the webbing of both X-links contain evidence of exposure to aft-to-forward flow conditions. Structural debris analysis suggests that initial failure occurred immediately aft of the starboard X-link from a combination of structural loads and thermal degradation, and the vehicle proceeded to separate from starboard to port side [3]. Despite similar flow patterns, the starboard X-link was recovered in the forebody debris field and the port X-link in the midbody debris field; this physical separation is theorized to have occurred after the combustion event.

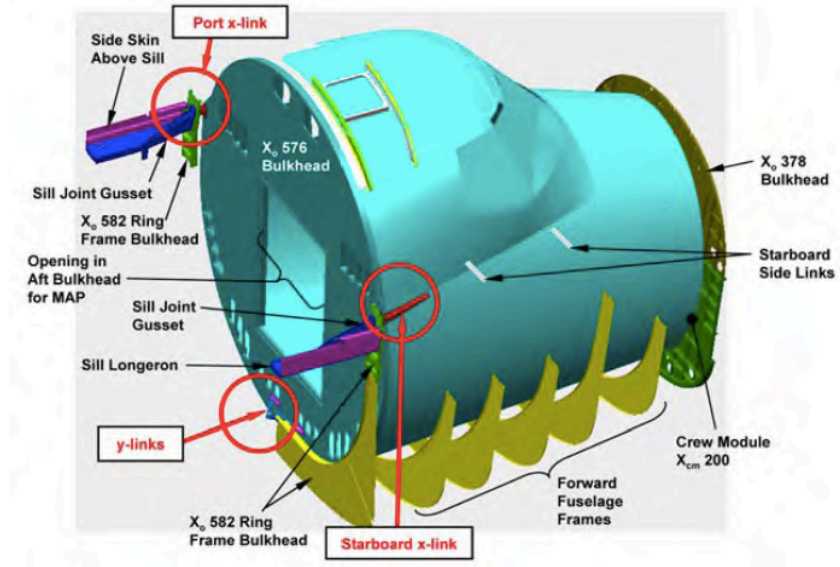


Figure 1.1. Schematic of configuration of X-links within the shuttle. Adapted from [3].



Figure 1.2. Top view as-received photographic documentation of the recovered X-links.

1.1.3 Arc-jet Testing Background

To better understand the physical features and history of the X-links, Ti-6Al-4V plates were tested in an arc-jet facility. Arc-jet testing currently represents the best ground-based simulation of a re-entry environment by providing the best ability to explore the oxidation behavior of materials under extreme conditions [4]. The arc-jet created the equivalent of a high altitude, hypersonic wind tunnel facility that heats and accelerates O_2 and N_2 gases through a nozzle and onto the surface of a sample [5]. Testing parameters, to include air content, angle of attack, and pressure, were designed to encompass conditions modeling predicted the X-links

were exposed to. Air content and angle of attack remained constant for all test specimens. Three different classifications of material response were observed from arc-jet testing (Figure 1.3). Class I represents material passivation, Class II represents ignition and initiation of melting without sustained combustion, and Class III represents ignition with sustained combustion. For explanation, Figure 1.4 shows where the classifications lie in a plot of inferred enthalpy versus dynamic pressure. The triangles indicated individual test samples. Note that higher dynamic pressure and inferred enthalpy contributed to a more aggressive environment and material reaction.

Testing was initially designed with a 30° angle of attack between incident air flow and metal plate, with the metal plate flush mounted on the stand. One sample was unknowingly installed with a slight protuberance from the mount. With this protuberance, and thus a higher effective ballistic number, ignition and combustion occurred. Without any protuberance, and thus a lower effective ballistic number, only oxidation with no ignition or combustion behavior was exhibited. The results of the arc-jet testing provided evidence that ignition and combustion are plausible phenomena for titanium alloys in the re-entry conditions the *Columbia* X-links were exposed to, though testing did not establish all conditions of re-entry supporting combustion.

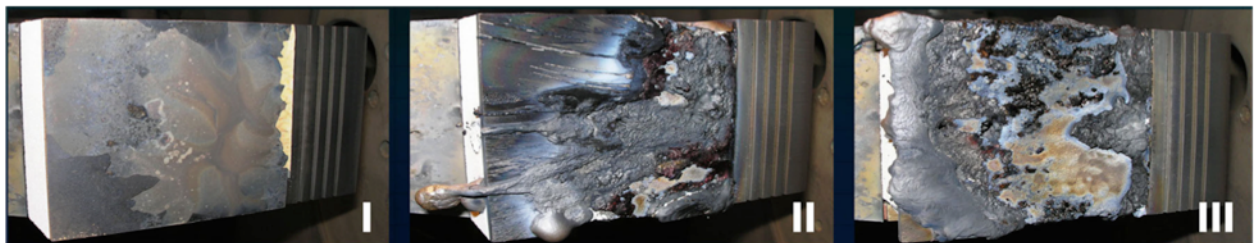


Figure 1.3. The three different classifications of material response observed in arc-jet testing.

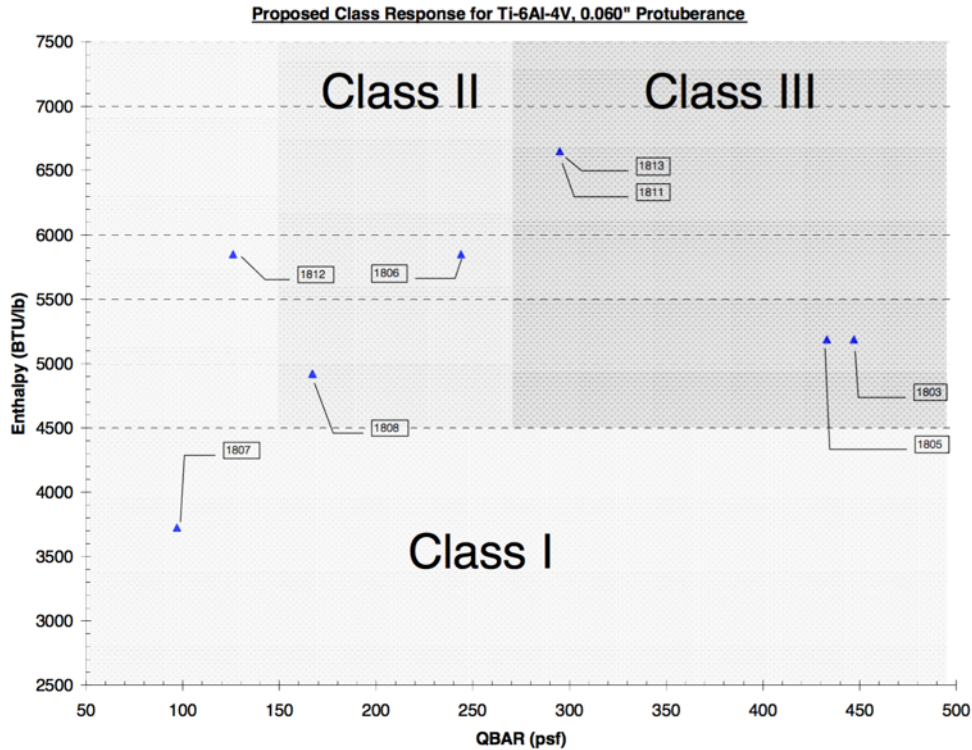


Figure 1.4. Arc-jet classifications of material response as they relate to enthalpy and dynamic pressure. Adapted from [6].

1.2 JUSTIFICATION

During accident reconstruction, NASA's Object Re-entry Survival Analysis Tool (ORSAT) predicted entry heating alone was not sufficient to explain the observed damage on the X-links, most notably the burn through in the flange area [3]. In order to cause the observed damage, analytical predictions from ORSAT estimated a required heat rate that was an order of magnitude higher than the maximum peak aero heating the vehicle could have experienced. These findings led to the consideration of other possible material interactions: shock-shock interaction and metal combustion. While it is understood that shock-shock interaction is a competing theory, the focus of this dissertation is on the latter. There are no shock-shock interactions in the arc-jet, and because the dissertation is a comparative analysis between arc-jet and actual re-entry conditions, shock- shock interaction is not considered.

During *Columbia* accident reconstruction, overhead windows from the forward fuselage were observed to contain a metallic deposit. This metallic ‘char’ layer was found to be largely composed of metal oxides, and an oxidized layer of Ti-6Al-4V was deposited prior to that of an aluminum alloy [7]. Simply from the standpoint of relative melting temperatures between aluminum and titanium alloys, and given the larger overall weight percentage of aluminum alloys comprising the shuttle construction, the observations from the overhead window char layer were puzzling. Thus, arc-jet testing was utilized in an attempt to explain these observations. As noted previously, Ti-6Al-4V exhibited three different material responses, with higher effective ballistic numbers producing more extreme material interactions. The complexity of the Ti-6Al-4V combustion reaction is demonstrated by the differing physical features of the X-links and arc-jet samples. Understanding the subtleties amongst oxidation, ignition, and combustion mechanisms of the alloy is instrumental in determining graceful degradation of titanium in the extreme environment of re-entry.

A forensic materials characterization study of two separate Ti-6Al-4V components that have been exposed to re-entry conditions, both actual and simulated, will further the understanding of bulk metal combustion in the extreme environment. Qualitative and quantitative correlations will be made between the X-links and the arc-jet samples in an effort to relate the known parameters of testing to the unknown parameters of the X-links re-entry into the atmosphere. This comparison will help to determine if ground-based testing methods are sufficiently representative of the actual environment to encompass conditions supportive of metal combustion. These results will also aid in differentiating separate material reactions in an effort to identify the mechanism of Ti-6Al-4V combustion in a re-entry environment.

Given the extensive use of titanium alloys as structural components in modern aerospace vehicles, consideration for the accelerated thermal degradation due to exposure of these alloys to the re-entry environment cannot be neglected. The aerospace community must be aware of a well-predicted degradation of materials being sent into space. It has been established that not every re-entry condition is supportive of combustion, but a catastrophic reaction has been

demonstrated as a very real possibility through arc-jet testing. Detailed materials characterization of the *Columbia* X-links and arc-jet samples will advance the understanding of titanium reactivity in the extreme environment of atmospheric re-entry.

This research is not applicable only to aerospace applications. Extreme environmental exposure is found in many industries, such as power generation and automotive [8]. The alloy is used extensively for the housings of turbine engines, a component of large proportions and complexity. Titanium alloys used in turbine engines have had occurrence of combustion [9]. Ti-6Al-4V is also used in the the automotive industry for special parts needing high temperature resistance. On air frames, Ti-6Al-4V is used as flow diverters, torque tubes for brakes, and helicopter rotor hubs. These extreme environments share many characteristics, namely high enthalpy and high flow conditions. Reliance on material integrity is paramount, and this research will aid in determining material reactions and characteristics in compromising environments.

1.3 PRESENTED WORKS

Two chapters in this dissertation are composed of published and presented works. The citations and abstracts for each published work along with corresponding chapters are listed as follows:

Chapter 4

The material in Chapter 4 was presented and published in the proceedings of the Materials, Science, and Technology (MS&T) 2015 conference, and is cited as follows:

J.L. Buckner, S.W. Stafford, D.M. Cone, “Materials Characterization of Ti-6Al-4V X-links from the Space Shuttle *Columbia*,” in Proceedings of MS&T 2015, Columbus, OH, October 4-8, 2015.

This work was a preliminary presentation of data gathered from materials characterization of two sections of *Columbia*. To supplement Chapter 4, further characterization of *Columbia* sections

will be discussed in Chapter 6. Permission to use the article cited above is documented in Appendix A.

Abstract

Recovered artifacts from the Space Shuttle *Columbia* provide a unique opportunity to examine a broad spectrum of materials exposed to the extreme environment of earth re-entry. The degradation states of these components offer a unique perspective into material behavior in this highly reactive environment. The crew module X-links, which are composed of Ti-6Al-4V and provided structural support to the crew module within the fuselage, exhibit evidence of both oxidation and combustion phenomena. The conditions supporting ignition and combustion of bulk metals are not fully understood, due to the many compounding factors affecting variable oxidation behavior of metals. Materials characterization of the *Columbia* X-links will yield further insight into the discrimination between the oxidation, ignition, and combustion response of titanium alloys. Widespread use of titanium alloys in space vehicles warrants a thorough characterization of their potential failure modes to help ensure the safe and reliable operation of future spaceflight vehicles.

Chapter 5

The material in Chapter 5 was presented and published in the proceedings of the International Association for Advancement of Space Safety (IAASS) 2016 conference, and is cited as follows:

J.L. Buckner, S.W. Stafford, D.M.Cone, J.D. Olivas, “Investigation of Ti-6Al-4V alloy response to atmospheric re-entry exposure,” in Proceedings of IAASS 2016, Melbourne, FL, May 18-20, 2016.

This paper serves as a comparison between arc-jet and X-link results. Supplementary X-link data is found in Chapter 6. Permission to use the material cited above is document in Appendix B.

Abstract

Ti-6Al-4V is a widely used aerospace alloy for its high strength-to-weight ratio and high operating temperature properties. Despite widespread use, titanium and its alloys have been shown to ignite in oxygen and nitrogen rich test streams. The reactivity of titanium is attributed to the high solubility for oxygen that increases with temperature, accelerating the oxidation rate and resulting in a combustion reaction. When introduced to the monatomic oxygen rich and high enthalpy re-entry environment, Ti-6Al-4V X-link components from the space shuttle *Columbia* exhibited accelerated oxidation and combustion behavior. Ti-6Al-4V metal plates tested in the simulated re-entry environment of an arc-jet facility have also exhibited ignition and combustion responses. A forensic material characterization study of the X-links and arc-jet samples is necessary to gain a better understanding of the material response in the dynamic and extreme environment of re-entry. Data from X-link components is compared to the Ti-6Al-4V samples previously tested in the simulated re-entry arc-jet facility conditions. The observation of similar microstructural and solidification features in conjunction with similar oxide compound detection suggest that arc-jet testing is representative of the re-entry environment effect on titanium and its alloys. A thorough materials characterization of these materials will yield insight into the discrimination between the oxidation, ignition, and combustion response of titanium alloys. Widespread use of titanium alloys in space vehicles warrants a thorough characterization of their potential failure modes to help ensure the safe and reliable operation of future spaceflight vehicles.

Chapter 2: Literature Review

The titanium alloy, Ti-6Al-4V, is commonly utilized as a structural material for its attractive properties, to include high operating temperature capabilities and excellent corrosion resistance. Yet, research has shown that nearly every commercial titanium alloy can ignite [10] [11]. Despite a relatively mature understanding of combustion involving gaseous and liquid fuels, knowledge regarding combustion of bulk metals is not as extensive. This is likely due to the many compounding factors affecting oxidation and combustion that complicate analysis, to include purity, gas composition, pressure, velocity past the surface, state of subdivision, and previous processing [12]. Several accidents involving metal-oxygen combustion in the space program have indicated that this phenomena deserves further consideration [13-14]. This literature review presents characteristics of the base element titanium and its $\alpha+\beta$ alloys as it relates to the oxidation, ignition, and combustion behavior. Ti-6Al-4V is not heavily alloyed, therefore several physical properties, oxide formation, and combustion mechanisms are similar to pure titanium metal.

2.1 CHARACTERISTICS OF Ti-6Al-4V

Ti-6Al-4V is a widely used aerospace alloy utilized for its high strength-to-weight ratio, corrosion resistance, and high operating temperature capabilities [15]. The microstructure is two phased, consisting of a Body Centered Cubic (BCC) beta (β) and Hexagonal Close Packed (HCP) alpha (α) (Figure 2.1). The addition of aluminum stabilizes the α phase, while the addition of vanadium stabilizes the β phase. Other α stabilizers include oxygen and nitrogen. An important parameter in Ti-6Al-4V processing is the β -transus temperature, defined as the temperature above which only the β phase is present at equilibrium [16]. HCP α exists below the β -transus, while BCC β exists above the β -transus. Figure 2.2 illustrates the pseudo-binary phase diagram of Ti-6%Al with additions of vanadium, indicating an approximate β -transus temperature of 1850°F-1950°F (1010°C-1065°C). The β -transus is dependent upon manufacturer, and literature widely disagrees on this value. Reference [16], focusing on heat

treatment and properties of nonferrous alloys, reports an approximate β -transus temperature of 980°C, while other sources report values around this.

Three distinctly different types of microstructures can be obtained dependent on the thermomechanical processing: 1) fully lamellar, 2) fully equiaxed, and 3) bimodal or duplex structures [17]. Some examples of these microstructures are shown in Figure 2.3. The thermomechanical treatments can be divided into four steps: I) homogenization, II) deformation, III) solutionizing or recrystallization, and IV) aging.

Lamellar structures encompass many of the microstructures to be discussed in this dissertation. Lamellar structures are established by cooling from the β phase field. The cooling rate from the β phase field in step III determines size of α colonies, width of α lamellae, and the presence of α at the grain boundary layer, with larger cooling rates producing smaller features. Many of the common structures shown in Figure 2.3 are lamellar structures. A slower cooling rate results in plate-like α , an intermediate cooling rate results in a Widmanstatten structure, and a quick cooling rate (as in quenching) results in a martensitic α' structure.

Equiaxed structures are obtained by slow cooling from the β phase field in step III and low temperature recrystallization processes, thus only primary α grains will grow with no α lamellae forming within the β grains. Equiaxed structures typically have the equilibrium β phase forming at triple points between the equiaxed α grains.

Solutionizing temperatures near the β -transus yield bimodal structures, containing equiaxed primary α in a lamellar $\alpha+\beta$. Bimodal structures exhibit the most balanced set of engineering properties and are most commonly applied in $\alpha+\beta$ titanium alloys. Width of α lamellae rely heavily on cooling rate in steps I and III, with higher cooling rates corresponding to decreased width of α lamellae. These three structures as they pertain to observed microstructural features will be discussed in Chapter 4.

It is acknowledged that FCC α' and HCP α'' exist as two separate entities, and that retained β is often converted into α' and α'' . In this work, these will be referred to as martensitic α , without a delineation between the separate α' structures. Alpha double prime (α'') is difficult

to resolve without very high magnifications, and is typically analyzed using transmission electron microscopy.

The strength of the material is higher at higher annealing temperatures and longer annealing times. This is because the martensite start and finish (M_s and M_f , respectively) temperatures are dependent on the annealing temperature. That is, at lower annealing temperatures below the β -transus, the M_s temperature is at room temperature due to increased vanadium in solid solution, thus a quench to room temperature does not allow for formation of martensite since the material will have to be cooled well below room temperature for formation.

Several physical properties to include melting temperature, thermal conductivity, and combustion rate are similar for titanium and Ti-6Al-4V [8]. Physical properties of titanium as they relate to oxidation and combustion for pure titanium and Ti-6Al-4V are shown in Table 1. Thermal conduction properties are relatively modest when compared to other structural aerospace alloys, like magnesium and aluminum-based alloys. Conduction of heat within a material as it affects surface temperature is an important factor in ignition [18]. With a lower thermal conduction and thus lower thermal inertia in the material, the surface temperature will rise more quickly and lead to the creation of a “hot spot”, in which a localized ignition reaction can occur. This “hot spot” was observed during arc-jet testing, in which localized regions of oxide would spall and eject molten material. Titanium also has a relatively low specific heat capacity compared to other structural aerospace materials such as magnesium and aluminum, requiring less heat input to produce a temperature increase. Thermal conductivity of Ti-6Al-4V is lower than that of pure titanium, though the thermal expansion and specific heat are comparable [8].

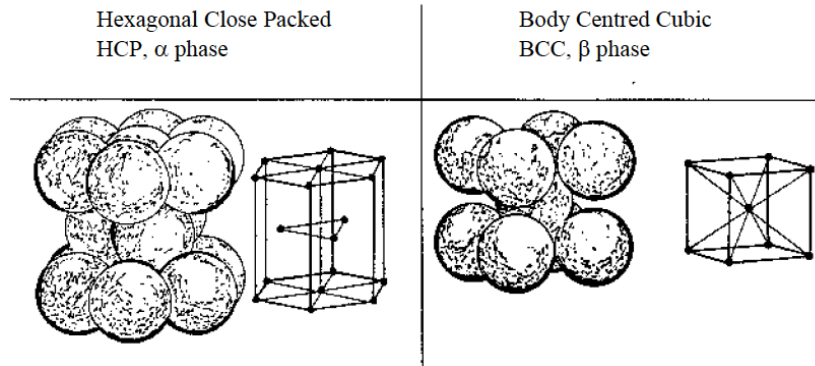


Figure 2.1. Illustration of the HCP α and BCC β unit cells. Adapted from [19].

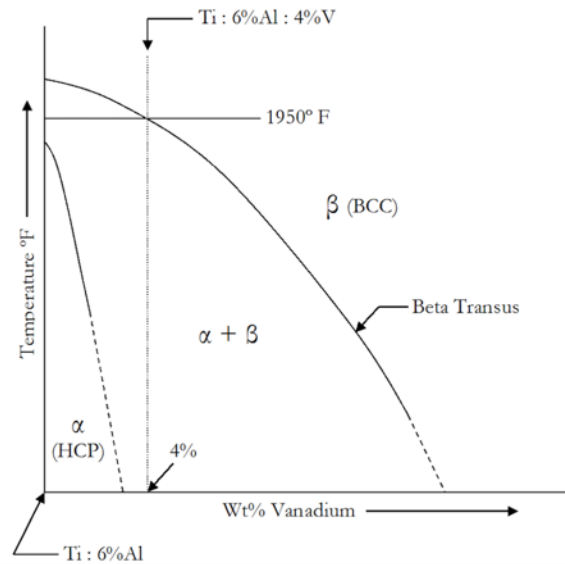


Figure 2.2. The pseudo-binary phase diagram of Ti-6%Al with additions of vanadium. Vertical line corresponds to a composition of Ti-6%Al-4%V, indicating approximate β -transus temperature of 1950°F. Adapted from [20].

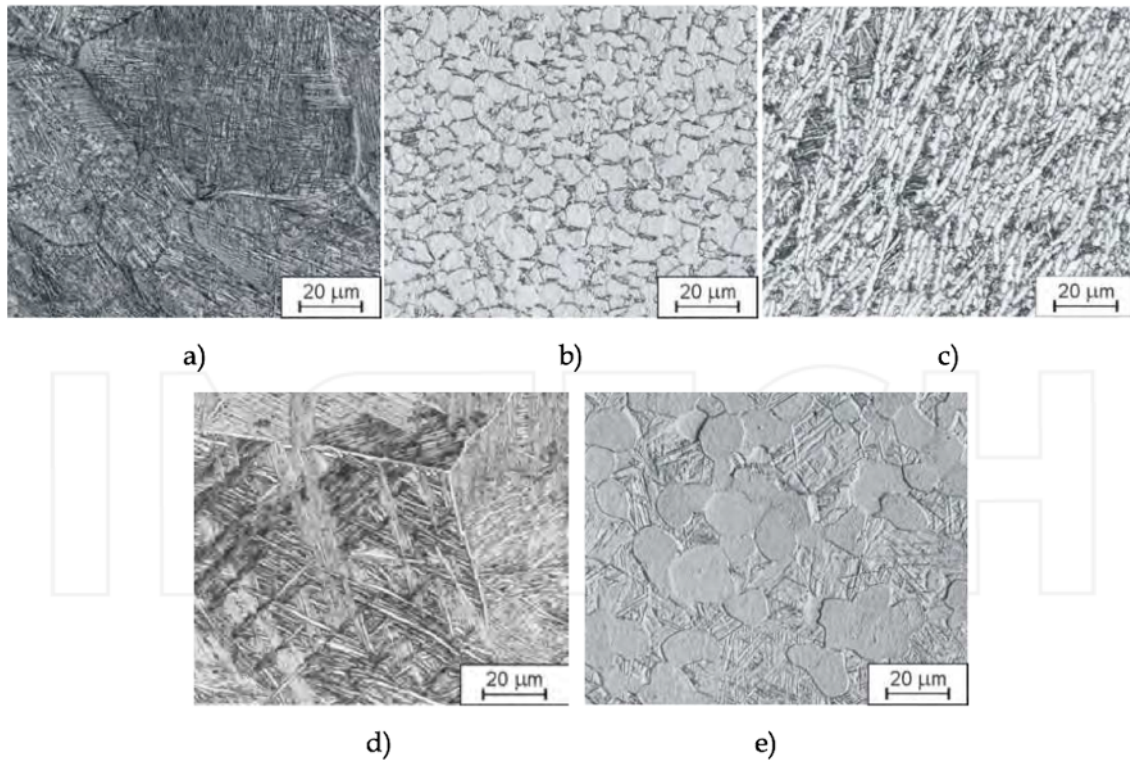


Figure 2.3. Microstructure of two-phase Ti-6Al-4V alloy: a) martensitic, b) globular, c) necklace, d) lamellar, e) bimodal. Adapted from [21].

Table 2.1. Properties of Ti-6Al-4V as they relate to combustion. Data for pure titanium retrieved from [22], Ti-6Al-4V from [8].

Physical Property	Ti-6Al-4V	Pure Titanium
Density (g/cc)	4.43	4.507
Thermal Conductivity at 20°C (W/m-K)	6.6-7.0	22
Specific Heat Capacity at 20°C (J/kg-°C)	580	522
Melting Point (°C)	1605-1660	1670
Boiling Point (°C)	3287	3289

2.2 OXIDATION OF TITANIUM

Previous research has focused on oxidation at low temperatures in steady state conditions, is not representative of the re-entry environment. The extreme nature of the re-entry environment would prohibit stable scale formation, resulting in the dynamic transport of material and deposit of multiple oxide layers when in the molten state. Literature pertaining to titanium oxidation typically represents molecular air or oxygen conditions, neither of which properly mimic conditions in a high velocity monatomic air or oxygen flow, which would yield a more reactive metal. Nonetheless, a review of titanium oxides is useful in understanding temperature regimes and composition ranges necessary for formation.

The oxidation behavior of Ti-6Al-4V is similar to that of unalloyed titanium [8]. Oxidation of titanium is complex, and several stable oxides exist (Figure 2.4). The complexity is related to the significant solubility for oxygen in titanium that increases with temperature. The stable oxides of titanium include Ti_2O , TiO , Ti_3O , Ti_2O_3 , Ti_3O_5 , Ti_nO_{2n-1} , and TiO_2 [23-24]. Physical properties of some titanium oxides are shown in Table 2.2. Note that titanium often has a higher density than its oxides, causing the metal to sink into the molten oxide as it accumulates. When the melting temperature of the oxide is lower than the ignition temperature, molten metal oxide is allowed to accumulate on the surface [12], as is the case with several of titanium's oxides. It is characteristic of titanium to be encompassed in a molten layer of oxidized material.

The most common titanium oxide form, TiO_2 (rutile), forms between 300°C to 1000°C [23,25]. Rutile is reduced at higher temperatures and is the least stable of titanium oxides. The conditions of re-entry do not often allow TiO_2 (rutile) to remain stable, as formation temperatures are surpassed and TiO_2 (rutile) readily volatilizes to form higher temperature oxides. Ti_2O_3 is a lower titanium oxide formed by reacting TiO_2 (rutile) with titanium metal at roughly 1650°C [26]. Oxygen deficient hexagonal oxides of the form Ti_xO are formed when oxygen orders in hexagonal α -Ti. These oxides are often formed at scale/metal interfaces. The oxide Ti_6O is a lower temperature oxide formed from the solid solution, and Ti_3O is a higher temperature oxide that crystallizes from the melt [27]. The higher oxide, Magneli-type phase, Ti_nO_{2n-1} ($3 < n < 10$),

forms when TiO_2 (rutile) is reduced [28]. Resources like an Ellingham diagram can be useful in determining which oxides will volatilize more readily. In order of increasing stability and difficulty of reduction, the oxides are as follows: TiO_2 , Ti_3O_5 , Ti_2O_3 , and TiO [29]. It is noted that this order also corresponds to increasing titanium content within the oxide. Generally, titanium nitrides are less stable and more easily volatilized than titanium oxides [30].

Rate laws followed by titanium vary at different temperatures, with temperatures above 1000°C following a linear, then decreasing parabolic rate [23]. The linear oxidation rate corresponds to an increased rate of oxide formation, and the transition to a parabolic rate occurs when growth of a compact layer of oxide acts as a solid-state diffusion barrier, decreasing the reaction rate. Once at a parabolic oxidation rate, the scale becomes thicker, and grains can begin to grow within the scale. Because it is unlikely that the X-links were able to form a stable, compact oxide layer, it is plausible that the reaction continued linearly at times, corresponding to an increased rate of oxidation.

Since X-link and arc-jet samples were in atomic air conditions, the titanium-nitrogen phase diagram (Figure 2.5) is included for reference. Titanium readily combusts in nitrogen, and will be discussed in more detail in later sections. Compared to oxygen in titanium, nitrogen has a limited solubility in titanium. Also, during combustion, the metal will be liquid, and nitrogen solubility is greatly affected by the presence of oxygen.

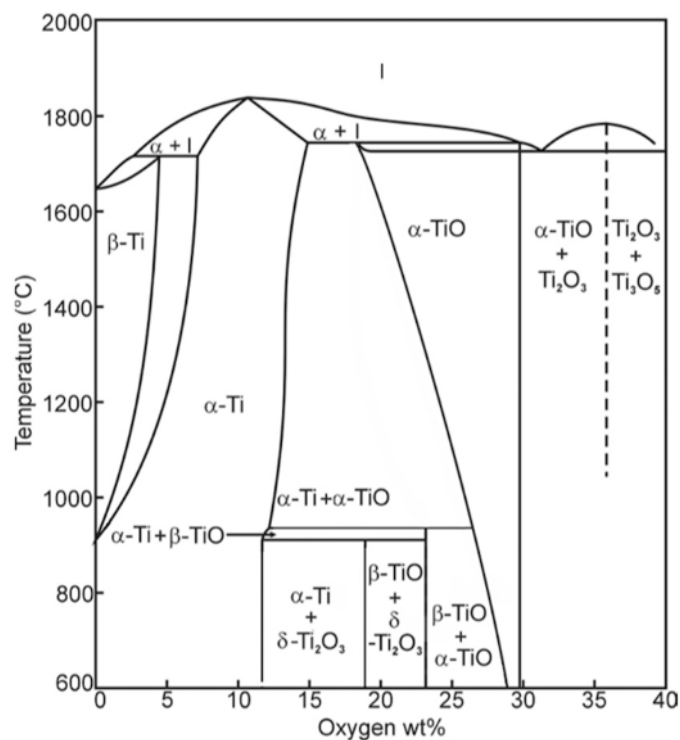


Figure 2.4. The titanium rich portion of the titanium-oxygen phase diagram. Adapted from [31].

Table 2.2. Physical properties of common titanium oxides. Data retrieved from matweb.com

Metal/Compound	Density (g/cc)	Melting Temperature (°C)	Molecular weight (g/mol)
Ti	4.5	1660-1670	47.9
TiO	4.95	1750	63.9
TiO₂	4.29	1850	79.86
Ti₂O₃	4.49	1842	143.7
Ti₃O₅	4.24	1777	223.6

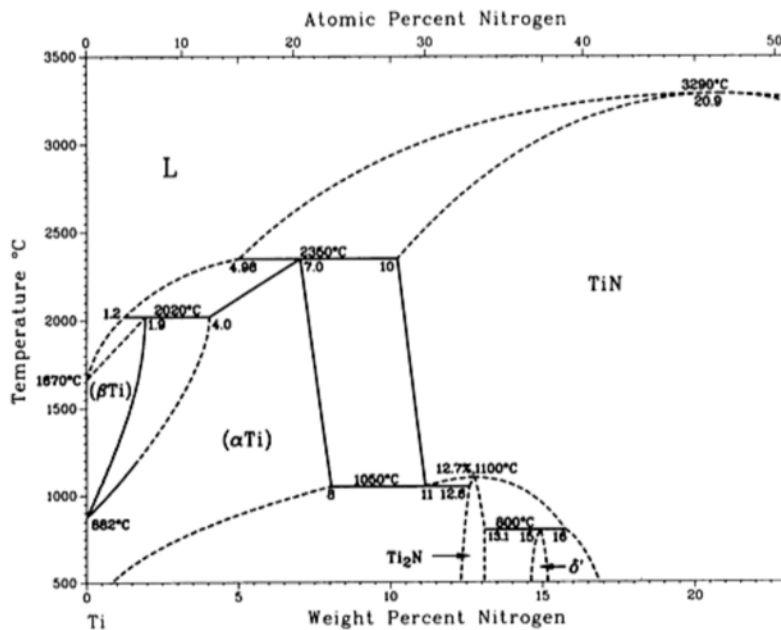


Figure 2.5. The titanium rich portion of the titanium-nitrogen phase diagram. Adapted from [32].

2.3 IGNITION AND COMBUSTION OF TITANIUM

2.3.1 Introduction

The chemical reaction of oxidation produces large amounts of heat. When the heat from the exothermic oxidation reaction is produced faster than can be dissipated by convective, conductive, and radiative heat losses, ignition and combustion occur. The ignition temperature is defined as the temperature in which the heat generated by oxidation first exceeds convective, conductive, and radiative heat losses [33]. The combustion of titanium is not a diffusion based, vapor phase reaction occurring at the surface of the metal, but instead is a heterogeneous reaction [34]. That is, the combustion process is a multiphase reaction, in which the metal and oxidant must be transported to the site of combustion through the phases of the metal and its oxides.

The combustion reaction is limited by fuel (metal), oxidant availability, oxygen pressure, temperature, and critical flow velocity [34]. Several mechanisms are defined as rate controlling, to include: oxygen diffusion and convection at the sample surface, physical and chemical absorption of oxygen molecules and atoms at oxygen gas/oxide boundary, diffusion of ions

through the oxide layer, and reactions at the oxide/metal boundary [35]. The energy necessary to initiate an ignition reaction must be provided by some ignition source; these include laser radiation and high pressure/temperature gas flow. There exists the autoignition temperature, at which ignition can spontaneously occur in the absence of external stimuli [36]. Lastly, there is a spontaneous ignition temperature, above which combustion will be self-sustained, and below which combustion cannot occur.

2.3.2 Pure Titanium

Several group 4 metals from the periodic table, including zirconium and hafnium, are highly reactive due to their considerable solubility for oxygen. Titanium is recognized as having a high heat of combustion and a high flame temperature [17,37-39]. Similarly, an increase in pressure has proven to lower the critical temperature necessary for ignition [40]. Historical review of titanium testing at NASA, Department of Energy (DOE), and Department of Defense (DOD) facilities [39] revealed that freshly exposed titanium surfaces are known to react violently with gaseous oxygen, while oxygen deficient test streams did not result in ignition.

Titanium was also found to combust vigorously in ambient pressure gaseous nitrogen, with higher pressures contributing to decreasing ignition temperatures [39,41]. Titanium exhibited combustion behavior in oxygen, nitrogen, and air [39], due to the considerable solubility of nitrogen in titanium [42]. Reynolds [43] and Peralta *et al.* [44] results agreed that oxygen versus oxygen/nitrogen atmospheric mixture did not appear to affect ignition temperature of bulk titanium, though ignition in oxygen produced an intensified burning. This indicates that ignition is likely controlled by a subsurface process, with oxidation controlled by adsorption or diffusion of oxygen into the metal surface. Kharatyan *et al.* [45] ignited pure titanium filaments in pure nitrogen, and found the ignition temperature to be above the metal melting point. This is an anomalous finding, and may be due to the presence of only nitrogen gas with no addition of oxygen. They theorized that the ignition of titanium was caused by dissolution of nitrogen into the metal, heats of formation associated with hard interstitial phases that form according to the

phase diagram, limitation of heat liberation, and diffusion resistance of nitride film formed on the surface. In summary, the nitride film which grows during the metal melting period exerts a strong effect on the progression of reaction.

Shuttle components were subjected to variable gravitational forces and loads during re-entry, caused by the rapid deceleration of the vehicle. Abbud-Madrid *et al.* [33,37,46] ignited pure titanium in oxygen atmospheres with a continuous radiation short-arc lamp source under reduced, normal, and high gravity conditions. Bulk metal combustion models that ignore gravitational effects have suggested that gravity plays an important role in heat and mass transport processes [35,47]. All temperature histories showed a change in slope corresponding to the latent heat associated with transformation of the metal from HCP α structure to BCC β structure. In reduced gravity, the environment is weakly buoyant, reducing the convective effects on the surface. Therefore, in reduced gravity, lower propagation velocities on the molten interface and longer burn times were found on the metal surfaces, indicating the strong influence of natural convection enhanced oxygen transport on burning rates. Higher temperatures, due to lack of convection, increased the localized boiling in the sample, resulting in intensified expulsion of particles from the surface. Tests performed at lower than 0.1 atmosphere (atm) pressures were attempted without evidence of a combustion event, indicating some threshold of reaction. Within the scales on the reduced gravity samples, TiO_2 and Ti_2O_3 in addition to TiO_3 and TiO_6 nearest the surface were found using an electron microprobe [48]. In normal gravity conditions, titanium combustion resulted in a self-sustained propagation followed by a violent exothermic reaction that included expulsion of small particles from the surface. The combustion products were swept upward by buoyancy induced currents. In high gravity conditions, higher convective forces led to the increased transport of oxygen to and from the metal surface, resulting in lower temperatures, yet higher oxidation rates and longer ignition times. This trend appeared to reverse after 5g's, with higher gravities leading to faster ignition times. Reactions were intensified by the higher oxygen transport rates and increased gravitational pull on molten products. In summary, gravitational effects appeared to have the highest effect on propagation

rate. Particles expelled in all gravitational conditions appeared to have undergone homogeneous gas phase reactions and multiple fragmentations once liberated from the bulk metal.

Formation of a hollow sphere has been documented in [49] and [50] for the case of titanium wires. Below a critical oxygen concentration, oxides formed would fragment and form a hollow sphere on the surface if artificially quenched. These hollow spheres were produced with aluminum, magnesium, zirconium, and titanium wires. The hollow sphere phenomena was postulated to occur when gas is dissolved into the metal, blowing up the liquid oxide shell. Surface combustion continues within the bubble, and all that is left is a hollow sphere; this specific effect and theory were developed for zirconium, a group IV metal with similar characteristics to titanium [51]. Branch *et al.* [52] also found evidence of hollow sphere formation, with the TiO₂ spheres undergoing a homogeneous gas-phase reaction and multiple fragmentation for pure titanium in microgravity environments.

2.3.3 Ti-6Al-4V

Alloying of titanium decreases the susceptibility to spontaneous ignition [53]. For example, increasing aluminum content from 5% to 20% increases the critical pressure necessary for ignition from 10 atm to 30 atm [53]. Though, practicality makes it unreasonable to design an alloy with such large concentrations of aluminum, as it dramatically decreases plasticity. Burn resistant titanium alloys have recently been developed, but usage is limited due to their cost [17]. These alloys tend towards less titanium, more aluminum, and an increase chromium and vanadium contents to decrease local heat release in ignition.

Like titanium, titanium alloys have exhibited an exothermic oxidation reaction on fresh surfaces that leads to the formation of oxides with the evolution of a large amount of heat and ignition [53-56]. At high oxidation rates, as would be expected in a re-entry environment, the heat of reaction will not dissipate quickly enough and the material will begin to burn. These studies explored varying geometries, angles of attack, and methods to achieve ignition, illustrating the complexity of compounding factors that must be considered. Gujadi *et al.* [57]

illustrated that the minimum oxygen pressure necessary to ignite cylindrical rod was the same for pure titanium and Ti-6Al-4V, yet Ti-6Al-4V exhibited a more violent combustion reaction when compared to commercially pure titanium. Strobbridge *et al.* [9] found that pure titanium and Ti-6Al-4V had the most comparable combustion rates of common commercial titanium alloys. Breiter *et al.* [58] found that for all titanium-zirconium alloys, ignition occurred below the melting temperature of the alloy, indicating that the ignition mechanisms of the pure metals is retained.

Bolobov [59] tested five separate titanium alloys, with Ti-6Al-4V being one of them, in high pressure oxygen flow. Combustion intensity and percent of burned surface increased with oxygen pressure. The critical pressure necessary for ignition did not show a dependence on sample thickness, but rather on distance from sample to the nozzle and diameter of the aperture. For all titanium alloys, the critical oxygen pressure necessary for ignition was larger for flow conditions than mechanical fracture. Bolobov theorized that this deflagration, combustion that propagates at subsonic speeds, occurs as the result of an electrical discharge, produced by liquid and solid particles suspended in the gas.

2.3.3 Ignition Methods

Fracture is often utilized as a method to induce ignition. Various methods have been used in literature to expose fresh fracture surfaces and induce combustion, to include tension [60], impact [61], rupture by oxygen pressure [60,62], and exposure of a specimen to high rate oxygen flow [63]. Bolobov [40,54] theorized that the fracture of metal samples involved creation of microfragments heated above significantly above ambient temperature by the heat of fracture work, and that the limiting stage of oxygen-titanium interaction during fracture is the dissociative chemical adsorption of O₂ molecules on the surface. Bolobov [64] later expanded on this theory of metal ignition at fracture, and confirmed that the dilution of the oxygen by less reactive species (nitrogen and water vapor) substantially increased the partial pressure of oxygen in the gas mixture, accelerating the self-ignition of titanium alloys. He suggested that the critical

temperature of ignition of titanium alloys is dependent upon partial pressure of oxygen and dilutants in the gas.

Another common method ignition method is laser radiation. Efimov *et al.* [56] found that titanium plates ignited by laser radiation show a dependence of the combustion rate on air stream velocity. A critical velocity was found, below which an ignition reaction could not occur. The nature of the critical velocity varied according to the viscosity of the alloy. Ti-6Al-4V has a lower viscosity, therefore the combustion rate was controlled by diffusion of oxygen into the partially oxidized melt layer. For Ti-6Al-4V, higher scale thicknesses corresponded to higher critical velocities necessary for ignition, suggesting that the the thicker the scale, the more energy was necessary for dissolution of oxygen into the surface. Efimov *et al.* [65] also found that combustion by pulsed laser radiation of Ti-2Al-1.5Mn alloy plates, of similar viscosity to Ti-6Al-4V, was limited by pressure. At pressures below atmospheric levels, the range of flow velocities in which self-sustaining combustion could be initiated initiated was reduced. Strakovskii [66] ignited titanium in air using a CO₂ laser radiation source. It was found that when titanium is heated in air or air flow, heat release of the material increases after the induction period when the growth of the oxide film leads to an increase in oxygen adsorbtion and thus the specimen heating rate.

Multiple theories exist on the mechanism of metal combustion in high velocity flow conditions [63]. Bolobov [67] proposed that the spontaneous deflagration of titanium alloys, to include Ti-6Al-4V, in a high pressure oxygen flow is initiated by electrical discharge due to the electrization of water particles and other impurities present in the flow. In later work, Bolobov [63] theorized that the mechanism of ignition under oxygen flow depended on the plastic deformation and local fracture of the oxide film. Metal particles are pulled away upon fracture, resulting in oxide free microcraters at the fracture site, exposing fresh metal surface. These conditions applied for both oxygen and nitrogen flow. Kovalev *et al.* [68] studied unsteady-state heating in the presence of oxidizer flow for pure titanium plates. At lower temperatures (977°C-1127°C), a homogeneous white film consisting of TiO₂ (rutile) formed, protecting the metal from

an ignition event. For temperatures above 1153°C, a multi-layer oxide formed with a top layer of TiO₂ (rutile) and inner layers of lower oxides, TiO and Ti₂O₃. For temperatures above 1600 K, a multi-layer scale is formed, with grains forming within the scale. The formation of grains corresponded to a decreasing parabolic oxidation rate.

Dissociative flow also exists for re-entry conditions. These particular mechanisms of combustion are noted as these methods encompass a range of possibilities of conditions for the X-links. Re-entry and break-up of the shuttle could have exposed several juvenile fracture surfaces, contributing to the combustion reaction. Likewise, preheating from ballistic heating and high velocity flow conditions are quite likely. The literature cited in this review illustrates the complexity of factors as it affects bulk metal combustion and how consideration of the many facets of the re-entry environment is key in understanding the complex reactions that occurred with *Columbia* components and arc-jet samples.

2.3.1 Ignition Temperature

Literature has cited a range of ignition temperatures for bulk titanium and its alloys, influenced by many factors: air content, pressure, preheating of the metal, configuration and dimensions of test specimen, and ignition method. Abbud-Madrid *et al.* [37] found the ignition temperature of pure titanium to be 1477°C in a weakly buoyant environment induced by reduced pressure, 1397°C in normal gravity, 0.1 MPa (0.98 atm) conditions [33], and 1452°C in oxygen in normal gravity, 1 atm environment using a continuous radiation short-arc lamp as the ignition source [46]. Derevyaga *et al.* [69] ignited varying thickness samples of pure titanium in oxygen at 1605°C and 1 atm pressure using an induction technique. NASA reports the spontaneous ignition temperature of titanium in air at a pressure of 1 atm to be 1593°C, while an ignition temperature of 1150° was reported for the same conditions in oxygen [39]. For titanium alloys, Uihlein *et al.* [34] reported ignition temperatures ranging from 1330°C in oxygen to 1600°C in air. Reynolds [43] reported ignition temperatures for titanium alloys to be between 1566°C-1627°C in hot air jet and electrically heated samples. Using induction heating of rod shaped

titanium, Peralta *et al.* [44] observed ignition temperatures of 1623°C -1659°C for pure titanium in both oxygen and nitrogen/oxygen gas mixtures and ignition temperatures of 1637°C -1649°C for Ti-6Al-4V in nitrogen/oxygen gas mixtures. For pure titanium, ignition temperatures of 925°C-1600°C have been reported in oxygen, and an ignition temperature of 1593°C in air by resistance heating [70-72]. A compilation of these ignition temperatures are shown in Table 2.3.

Table 2.3. Ignition temperatures of bulk Ti and Ti alloys.

Material	T _{ign} (°C)	Test Pressure	Test Gas	Ignition Source	Notes
Pure Ti [37]	1477	1 atm	O ₂	Short arc-lamp	Reduced gravity conditions
Pure Ti [33]	1397-1452	0.1 MPa (0.98 atm), 1 atm	O ₂	Short arc-lamp	Normal Gravity Conditions
Pure Ti [69]	1605	1 atm	O ₂	Induction Heating	
Pure Ti [39]	1593	1 atm	Air	???	
Pure Ti [39]	1150	1 atm	O ₂	???	
Ti and Ti alloys [34]	1330-1600	N/A	O ₂	None noted	
RC-70 (Pure Ti) [43]	1582-1626	1-7 atm	Air, O ₂	Resistance Heating	
RS-70 (98.65% Ti)	1587-1613		Air, O ₂		
RS-110-A (Remaining Ti)	1571-1599		O ₂		
RS-110-BX (Balance Ti)	1566-1604		O ₂		

Pure Ti [44]	1623-1659	1000 psia (68 atm)	O ₂ , O ₂ /N ₂ mixture	Induction Heating	
Ti-6Al-4V	1637-1649	1000 psia (68 atm)			
Ti alloys [70]	1149	500 psia (34 atm)	O ₂	Resistance Heating	
	1593	14.7 psia (1 atm)	Air		
Pure Ti [71]	1310-1600	14.7 psia (1 atm)	O ₂	N/A	
Pure Ti [72]	925	O ₂	50 psia (3.4 atm)	Resistance Heating	
Pure Ti [72]	1370	O ₂	300 psia (20.4 atm)	Resistance Heating	

It is evident that oxygen environments produce ignition at lower temperatures, despite the solubility of nitrogen in titanium. Alloying elements vary, therefore properties such as viscosity can play a role in ignition temperatures. These ignition temperatures are below the melting point of Ti-6Al-4V (1605°C-1660°C) and pure titanium (1660°C-1670°C). A spontaneous ignition temperature below the melting temperature of the metal poses serious risks, especially in oxygen enriched environments, where critical temperature for ignition can decrease. The highly reactive nature of this alloy poses a safety risk in high temperature applications, and brings focus to the sparsity of knowledge regarding which conditions are conducive to a combustion reaction.

2.4 PARTICULATE COMBUSTION OF TITANIUM

When certain metals become finely divided and fresh surfaces are exposed, the metal can become highly reactive [73]. In some cases, they can even become pyrophoric, meaning that they

will spontaneously combust in air. Impact or separation of the X-links from other structural components may very well have expelled finely divided Ti-6Al-4V particles from the metal, causing an ignition reaction to occur. Relative to combustion of bulk titanium, particle combustion has been more widely studied. Particles generally have ignition temperatures lower than those of the corresponding bulk metal, owing to the increased surface energy [12]. The use of metal additives in propellants [74], synthesis of nanoscale titanium oxide particles [75], and even the generation of brush fires in arid climates [76] have generated research questions regarding titanium particle combustion. Literature detailing fragmentation of particles from a bulk metal surface, discussed in the previous section, also suggests that combustion of smaller particles produces a homogeneous surface reaction. This is in contrast to the heterogeneous combustion that bulk titanium experiences. Similarly, footage from arc-jet testing documents expulsion and fragmentation of particles from the metal surface. For these reasons, particle combustion of titanium will be discussed.

Despite research efforts, available knowledge of titanium particle combustion in air is not expansive. Relationships between particle size, air content, and combustion reaction length are not fully understood. Shafirovich *et al.* [77] combusted levitated, <150 μm pure titanium particles in air with a laser ignition source. The particle sizes were not shown to change during ignition, and the reaction was terminated by an explosion. Results indicated that gas phase diffusion plays an important role in the combustion of the 100 μm or larger titanium particles in air, but that smaller particles appear to have a kinetics controlled reaction. Glotov [78] studied combustion and fragmentation of 300, 390, and 480 μm agglomerate produced titanium particles in air. Upon release from the sample, the particles took a spherical shape upon attainment of the melting temperature of titanium. The smaller particles tended to fragment immediately after taking on a spherical shape, while the larger particles fragmented at separate time intervals. Combustion time increased with increasing particle size. Differing fragmentation velocities of particle sizes suggest that fragmentation is associated with the internal state of the material, and not the surrounding air velocity. Mother particles were retained despite fragmentation; the final

shape of the ejected particles was a spruce tree, while the final state of the mother particle was a sphere with titanium oxides ranging from TiO to TiO_5 . Grachukho *et al.* [79] ignited 0.5-2 mm diameter spherical and cylindrical titanium alloy particles in oxygen/nitrogen gas mixtures. The limiting gas temperature for ignition decreased with increase in specific surface, with smaller particles having lower limiting temperatures. Increase in oxygen concentration in the gas also decreased the limiting ignition temperature of both spherical and cylindrical particles, and initial particle heating produced a decrease in ignition limit.

Mechanical activation of titanium particles has been shown to increase its ignition and combustion intensity. Voyuev *et al.* [80] postulated that the stronger influence of mechanical activation on the ignition process than the combustion process is due to the fact that burning of the powder grain surface layers deformed during ball milling in vacuum results in an ignition reaction. That is, the defects introduced to the surface accelerate the combustion velocity by increasing oxygen content in the stressed lattice. Shafirovich *et al.* [81] illustrated that after ball milling in air, the lower concentration limit of explosibility is decreased with increased grinding time. The authors concluded that this is a function of the decreasing particle size, increasing the specific surface of the material. Oxide films formed during ball milling were shown to have minimal influence on the explosion characteristics.

The role of nitrogen in the combustion process is also of interest. Nelson [82] examined combustion of metal droplets in pure oxygen and in an oxygen/nitrogen atmosphere mixture. It was demonstrated that in the initial metal-rich stages of oxidation, though both nitrogen and oxygen are initially absorbed by the metal droplets, the ultimate product may consist of only oxygen and the metal. This is because as the composition of the droplets approaches the more thermodynamically favored oxygen-rich composition, nitrogen is released. Khomenko *et al.* [83] found that nitrogen gas plays a significant role in ignition and combustion when igniting titanium particulates in oxygen, nitrogen, and air. Through time-resolved X-ray diffraction during ignition of titanium particles, titanium nitrides and oxynitrides formed prior to TiO_2 when titanium is combusted in air, though these nitride species were not resolved in the final product.

These studies confirm what was previously noted in Chapter 2.3, referencing the relative stability of titanium nitrides and titanium oxides. Despite all the evidence presented, Shafirovich *et al.* [77] found that N_2 acted as an inert gas during the combustion process, with only O_2 gas diffusion playing a prominent role in combustion when combusting titanium particles in air. Andrzejak *et al.* [84] studied the mechanisms of titanium particle reactions in O_2/N_2 and O_2/Ar atmospheres, and found that prolonged heating of titanium particles results in formation of a liquid TiO_2 bead that later ejected into fragments. TiO_3 was found at the bead interface, suggesting a supersaturation of oxygen and gas entrapment within the bead that led to fragmentation. Fragmentation occurred in both atmospheres; in the O_2/N_2 atmospheres, fragmentation was more intense than in the O_2/Ar atmospheres, at which the authors concluded that the N_2 accelerates the oxidation of liquid titanium.

A thorough discussion on particulate titanium combustion in air was offered by Molodetsky *et al.* [85]. The authors tested 240-280 μm titanium particles in air, altering combustion times and cooling rates. The maximum recorded temperatures of the titanium particles were close to $2400^\circ C$, well below the volatilization temperature of either titanium or its oxides. As combustion time increased, concentration of dissolved gases in the particles increased. One set of samples was quenched rapidly in air on aluminum foil and the other quenched slowly in an inert gas atmosphere. The quench rate affected the formation of phases within the particles. With a rapid quench, phase compositions differed moderately. With a slow quench, phase compositions differed considerably. That is, there was more phase separation present for those samples cooled slowly. Neither of the two phases was identified as a stoichiometric oxide or nitride, though in the slowly quenched samples, a phase close to stoichiometric Ti_2O_3 was observed. Because quenching produces a solidification reaction, nitrogen gas release and crack formation are likely to occur when the Ti_2O_3 oxide forms. For particles cooled slowly in an inert gas, voids were observed in the interior of the particles. For particles quenched rapidly in air, fresh surfaces produced by void formation reacted with oxygen, resulting in gas expansion and particle explosion.

Two temperature jumps were observed [85]. The authors developed a theory based on the binary Ti-O and Ti-N systems and the ternary Ti-N-O system to explain these temperature jumps and the reactions occurring inside the particle. Initially, oxygen and nitrogen gases were distributed throughout the particle in a homogeneous Ti-N-O solution. Looking at the Ti-N and Ti-O system, it is apparent that at combustion temperatures, oxygen has unlimited solubility while nitrogen has limited solubility. Because the particle was liquid during combustion, the authors concluded that the solubility of nitrogen within the particle must have been altered by the presence of oxygen. The two spikes in temperature occurred at 2300°C, early during combustion, and 1800°C, occurring near the end of combustion and associated with an explosion. The first spike, at 2300°C, was thought to be caused by the precipitation of a phase close to α -Ti, since the peritectic reaction ($\text{Liquid} \rightarrow \text{TiN} + \alpha\text{-Ti}$) on the Ti-N phase diagram occurs near that temperature. The Ti-O system does not have any reactions at that temperature. Since the nitrogen content decreases at this stage, and experimental ternary Ti-N-O diagrams suggest the disappearance of a nitrogen rich phase, it was conjectured that gaseous nitrogen is released, instead of forming TiN as per the peritectic reaction. The second radiation jump, at 1800°C, is thought to be associated with the eutectic reaction ($\text{Liquid} \rightarrow \gamma\text{TiO} + \beta\text{Ti}_2\text{O}_3$) on the Ti-O phase diagram. No phase transformation can be found on the Ti-N diagram at this temperature.

The literature suggests a strong dependence on gas content on the complex reactions taking place during combustion; more so with particulates than bulk metals. Parallels can be drawn between particle combustion and bulk metal combustion of titanium. For example, pre-heating and oxygen atmospheres decrease the ignition temperature, and nitrogen was found to be released as combustion progresses. This literature review serves to give perspective on the complexity of combustion, on the bulk and particle scale. Literature does not provide agreeing results, and provides several differing views on the mechanisms governing these reactions.

Chapter 3: Experimental Methods

3.1 PRIMARY SECTIONING OF X-LINKS

Because of the unique nature of the *Columbia* artifacts, it was necessary to complete a thorough nondestructive evaluation prior to destructively sectioning the X-links. Nondestructive methods utilized included as-received photography, visual observation, photographic compilation to construct a three dimensional model, and X-ray fluorescence (XRF) for chemical analysis. These methods thoroughly catalogued the as-received state and surface features of the X-links; unique physical features were noted when creating a destructive sectioning plan.

Due to the complicated geometry of the components, meaningful XRF data was difficult to obtain. Few planar surfaces were available for analysis, thus XRF results were problematic to obtain safely and with accuracy. Therefore, visual observations were a main contributor during development of a cut plan. A cut plan focusing on the areas with the most extensive mass loss and deterioration was developed to most fully characterize the accelerated degradation response of the material. The forward-to-aft and aft-to-forward flow patterns were also considered, and sections were taken to represent both of these flow regions. The starboard and port X-link were sectioned in an identical manner. The port and starboard X-link after primary sectioning are shown in Figure 3.1, with the lettering denoting the child piece nomenclature from the parent X-link. Primary sectioning was performed with a water jet cutter to minimize thermal effects from cutting that could convolute the data obtained. Samples of loose matter were scraped off prior to water jet cutting. Secondary sectioning of the child pieces, after further non-destructive evaluation, for metallographic analysis was performed at a slow rate using a cut-off saw lubricated with an oil/water emulsion.

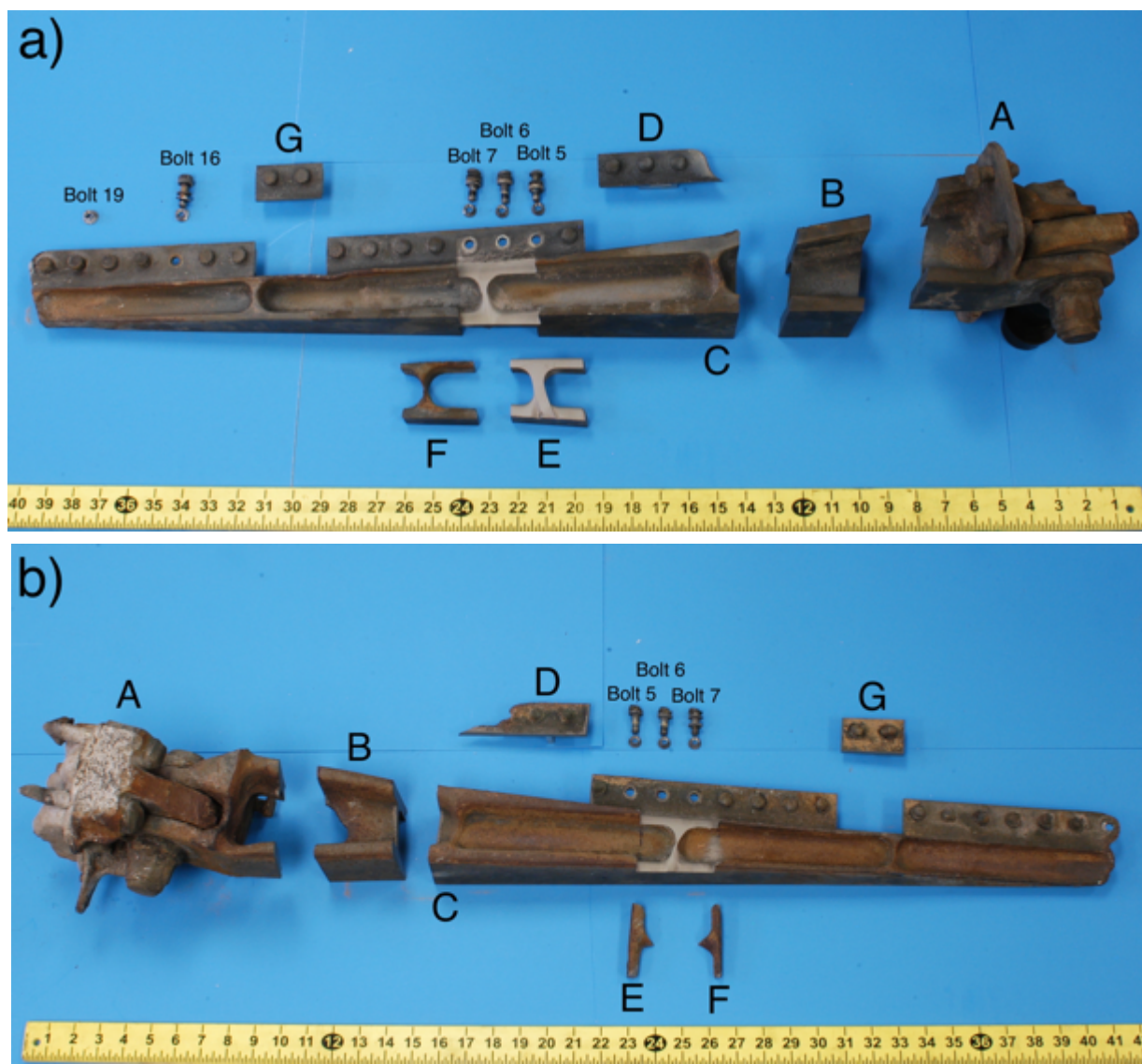


Figure 3.1. Primary sectioning of port (a) and starboard (b) X-links, top view.

3.2 SECONDARY SECTIONING OF X-LINKS

The starboard X-link was chosen for more thorough analysis due to the severely deteriorated state. Surface features of starboard X-link sections D, E, F, and G were analyzed and documented with with Keyence digital imaging for high resolution imaging of the surface, Scanning Electron Microscopy (SEM) and Energy Dispersive X-ray Spectroscopy (EDS) for higher magnification imaging and semi-quantitative chemical analysis, and X-ray Diffraction (XRD) for identification of oxide species.

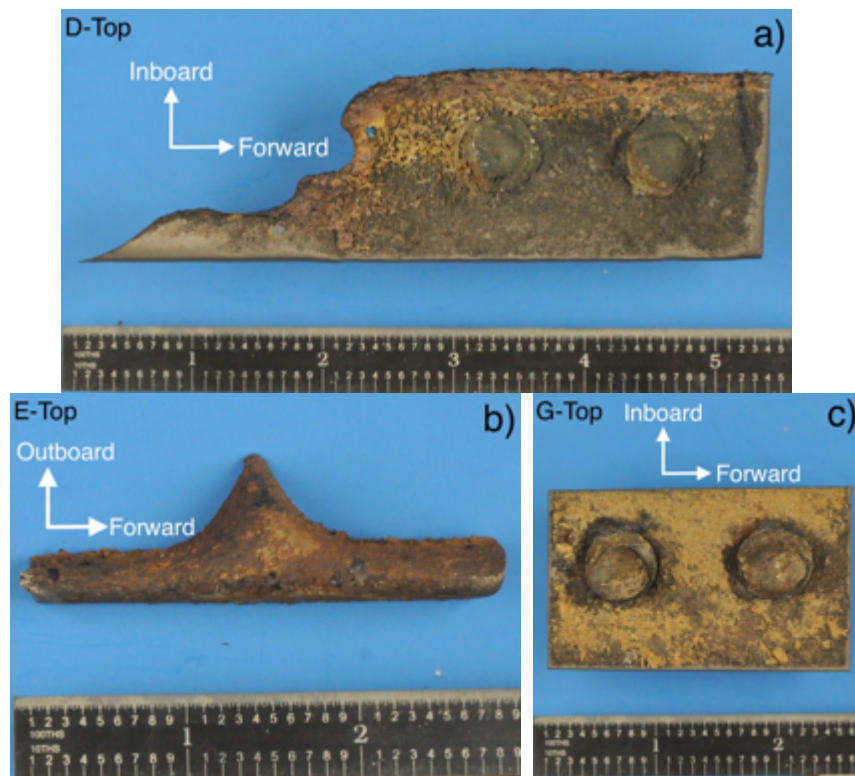


Figure 3.2. High resolution images of starboard pieces D (a), E (b), and G (c).

Figure 3.2 indicates the primary sections chosen for secondary sectioning and cross-sectional analysis. Locations of secondary sections are indicated by dotted lines in Chapters 4, 5, and 6. After secondary sectioning, child pieces were further labeled with number designations. For example, from the parent starboard X-link, section D was taken. Any secondary sections made to child piece D were named section D.1, D.2, etc. Cross-sections were analyzed with metallography and light optical microscopy (LOM) for microstructural analysis, SEM and EDS, XRD, and microhardness testing to relate mechanical properties to microstructural features. All samples were swab etched with Kroll's reagent (1.5 mL HF, 4 mL HNO₃, 94 mL H₂O). Microhardness testing, performed on the Buehler Micromet 3, was performed with a 500 kg load and 15 second dwell time on a calibrated instrument.

To determine initial microstructural state, port and starboard sections B were prepared by metallographic replication. The thickest portion of the X-links were chosen for replication (~1

inch thick), with the locations of the replicas shown in Figure 8.1 and 8.2. A discussion of the initial microstructural state of the X-links can be found in Chapter 5.3.1.

3.3 SECTIONING OF ARC-JET SAMPLES

Two Class II (ignition with unsustained combustion) and two Class III (ignition with sustained combustion) arc-jet samples were analyzed. The four samples analyzed were tested with the same protuberance (0.06 in.) and maintained similar configurations within the test. All samples were configured with a 30° angle between the fixture and the nozzle. The metal plates were fixed to a silicon carbide ceramic block with the use of a screw welded to the arc-jet plates for testing. Upon receipt, the arc-jet samples had been previously sectioned and handled. Figure 3.3 shows the four arc-jet specimens chosen for analysis. Table 3.1 shows pertinent testing information. More extreme material responses resulted from higher enthalpies and dynamic pressures. The step size refers to the protuberance of the sample from the mount. Dynamic pressure refers to the kinetic energy per unit volume of a particle upon release.

In areas where the titanium had melted completely, nearest the leading edge, a brittle char layer composed of a mixture of titanium, silicon, carbon, and oxygen covered the surface. Due to the focus of the dissertation on analysis of Ti-6Al-4V, only the remaining metallic portions of the sample were analyzed. In the class III reactions, more metal was consumed, and the remaining metal is encased in oxidized, melted titanium.

The arc-jet samples were sectioned perpendicular to the leading edge, one inch from the right side, as shown in Figure 3.3. Methods for characterization of the arc jet samples mirrored the methods utilized with the starboard X-link. Surface analysis of the samples was performed using Keyence digital imaging, SEM and EDS, and XRD. The cross-sections were analyzed using metallography and LOM, SEM and EDS, XRD, and microhardness testing. The samples were swab etched with Kroll's reagent, and microhardness testing was performed on a calibrated instrument with a 500 kg load and 15 second dwell time.

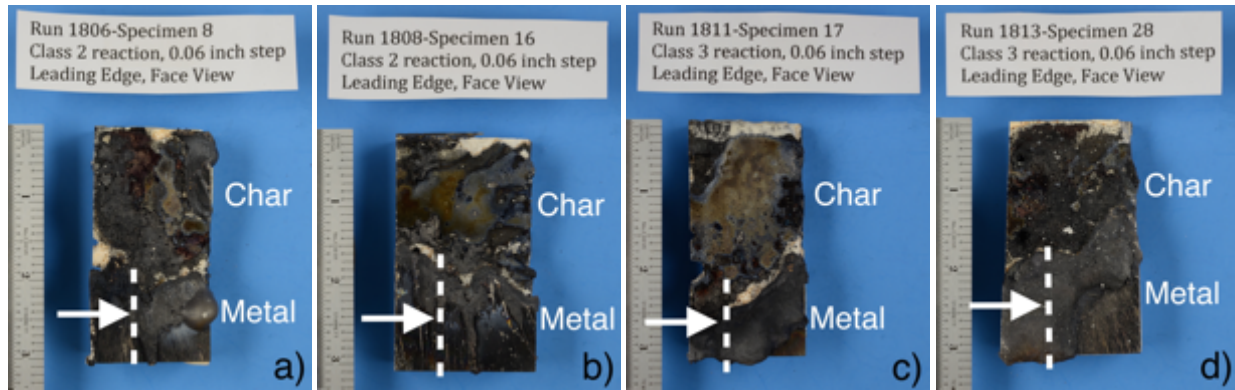


Figure 3.3. High resolution images of arc-jet specimens 8 (a), 16 (b), 17 (c), and 28 (d).

Table 3.1. Test matrix for chosen samples.

Run #	Specimen #	Configuration	Inferred Enthalpy (Btu/lb)	Dynamic Pressure (psf)	Test Duration (seconds)
1806	8	0.06 in. step	5852	244	25
1808	16	0.06 in. step	4921	167	40
1811	17	0.06 in. step	6650	295	10
1813	28	0.06 in. step	6650	295	22

6.1.1 ARC-JET SUPPLEMENTARY DATA

Explanation of the testing conditions and data is necessary for the arc-jet samples. Figures and information presented in this section are adapted from testing data from [6]. Figure 3.4 shows the test configuration and location of thermocouple (T/C) 1,2, and 3 as they relate to the time versus temperature data shown in Figure 3.5. The thermocouples were placed at roughly $\frac{1}{4}$, $\frac{1}{2}$, and $\frac{3}{4}$ of the length of the 3-inch specimen through the centerline. The thermocouples were Type C (W-Re) with a service range of 4200°F (2315°C). If there was a combustion reaction in the location of the thermocouple, the temperature reading became unreliable because the thermocouple junction was compromised. For example, T/C 1 and 2 were destroyed while

testing the given samples discussed in this dissertation. This is obvious from the photographic images indicating that more than half of the volume of material from leading edge to trailing edge was thermally eroded. Therefore, drastic spikes and depressions within the T/C data occur at the times in which this erosion occurred and data thereafter is considered dubious. The final drop in temperature occurred when the swing arm removed the sample from the arc-jet stream and the sample began to cool.

There is an inflection point located between 1850-1950 °F, at the β -transus, produced by the latent heat of phase change from α to β . In general, the temperature of the trailing edge remained below the temperature of the leading edge, as would be expected considering the location of the source of heated gases. The samples generally ramped up in temperature at a steady rate, with the exception of Run 1811, Specimen 17, in which temperature increased for T/C 1 within 4-5 seconds. It is noted that Run 1811 (Specimen 17) and Run 1813 (Specimen 28) had identical enthalpy and dynamic pressure test parameters, yet Specimen 17 reacted much more rapidly and violently than Specimen 28.

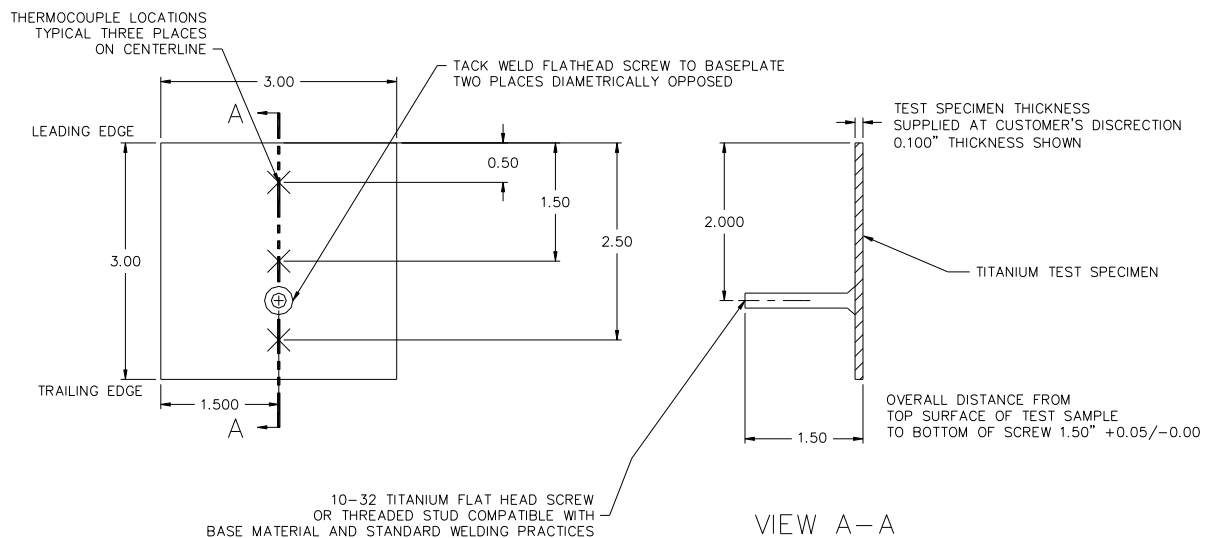


Figure 3.4. Test article configuration schematic. Adapted from [6].

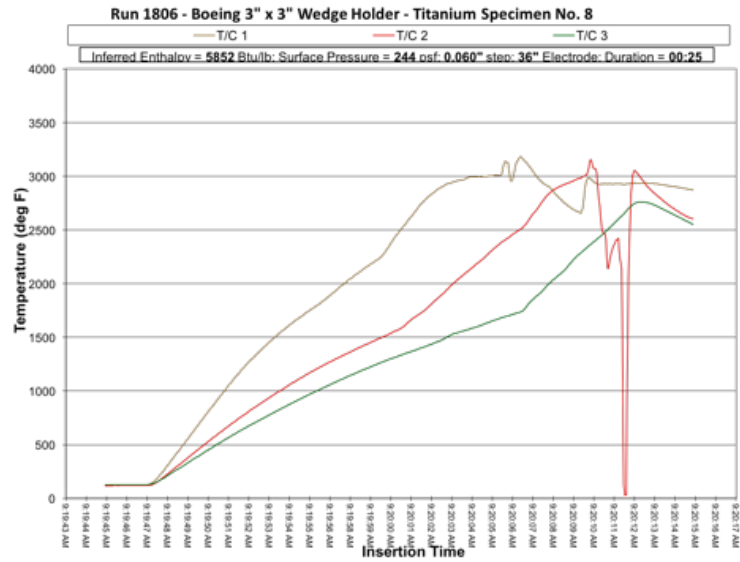


Figure 3.5. Insertion time vs. sample temperature data for Run 1806, Specimen 8. Adapted from data files from [6].

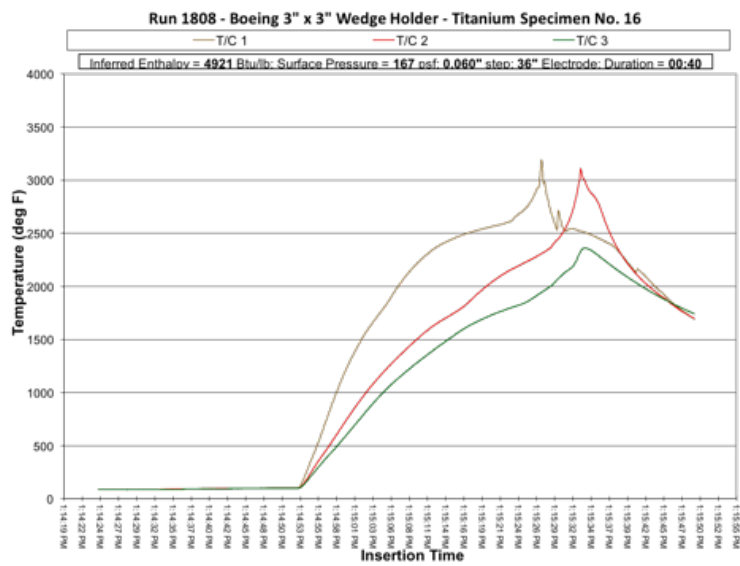


Figure 3.6. Insertion time vs. sample temperature data for Run 1808, Specimen 16. Adapted from data files from [6].

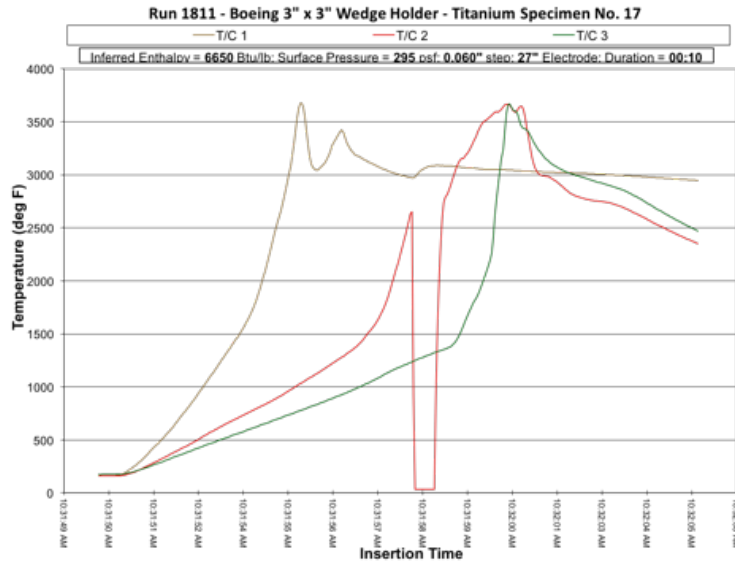


Figure 3.7. Insertion time vs. sample temperature data for Run 1811, Specimen 17. Adapted from data files from [6].

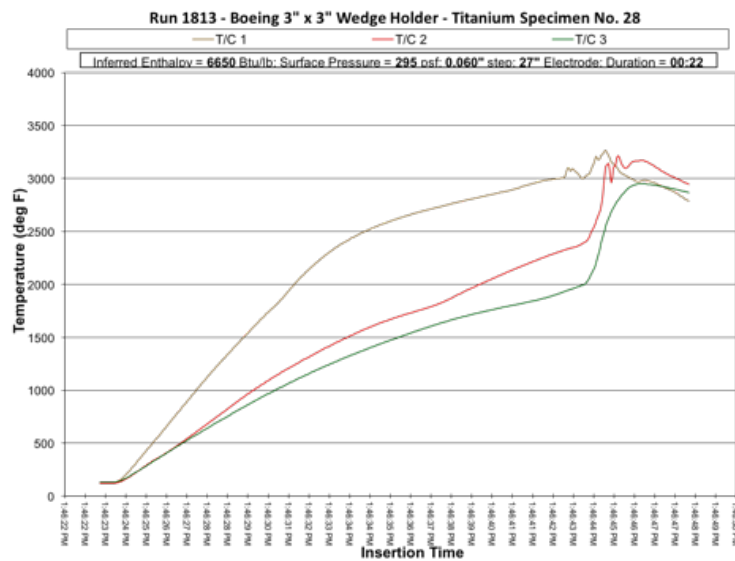


Figure 3.8. Insertion time vs. sample temperature data for Run 1813, Specimen 28. Adapted from data files from [6].

3.4 HEAT TREATMENT STUDY

During the combustion reaction, the material began to melt, reaching temperatures in excess of 3000°F (1649°C). Burning a material surpasses the β -transus temperature to such a great extent that the resultant material is not of commercial value, therefore microstructures of materials that have been treated at those high of temperatures are difficult to find in literature. To establish a better understanding of the effect of temperature exposure above the β -transus on microstructure, a basic heat treatment study was designed. Untested Ti-6Al-4V plate samples from the arc-jet testing, cut with a water jet to dimensions of 3/4 in. x 3/4 in. x 1/8 in., were held at temperatures ranging from 1650°F-2650°F (899°C-1454°C), in 100°F (37-38°C) increments, for 15 minutes, then quenched in an agitated water bath. The only exception is for the last sample, Heat Treatment 12, in which it was held at the maximum temperature (2650°F) for 30 minutes. To prevent excessive oxidation, the samples were wrapped in titanium getter foil prior to heat treatment. Two samples per heat treatment in addition to two untreated samples were mounted for microstructural analysis. The polished samples were etched with Kroll's reagent and characterized using LOM and microhardness testing. Results from heat treatment are shown in Chapter 7.

Chapter 4: Materials Characterization of the Oxidation and Combustion Behavior of Ti-6Al-4V X-links from the Space Shuttle *Columbia*

4.1 INTRODUCTION

On February 1, 2003, NASA's Space Shuttle *Columbia* suffered a catastrophic failure during re-entry into Earth's atmosphere. Ultimately, all seven-crew members lost their lives in this tragic event. Root cause analysis determined that a breach of the reinforced carbon-carbon (RCC) composite leading edge of the port wing was caused by a piece of insulating foam that detached from the external fuel tank during lift-off. This breach allowed superheated gas ingestion into the vehicle during re-entry, which ultimately degraded the sub-structural components and integrity of the space shuttle [86].

This investigation focuses on the starboard X-link from the space shuttle *Columbia*, one of two sub-structural components that connected the crew module, forward fuselage, and mid-body structures of the vehicle in the longitudinal direction. The X-links are composed of Ti-6Al-4V, a common titanium aerospace alloy used for its high strength-to-weight ratio, corrosion resistance and high operating temperature capabilities [87]. The structural attachment bolts that remain fastened to the X-links were found to be composed of MP35N, a nickel-cobalt-chromium-molybdenum alloy.

Upon recovery of the X-links after the accident, both the port and starboard components exhibited thermal degradation patterns that could not be explained by re-entry alone, shown in Figure 4.1. Compared to the port X-link, the starboard X-link exhibits more mass loss, discoloration, and is missing the aft-most bolt. The bolt heads exhibit evidence of exposure to forward-to-aft flow conditions, while the webbing of both X-links contain evidence of exposure to aft-to-forward flow conditions. Structural debris analysis suggests that initial failure occurred immediately aft of the starboard X-link from a combination of structural loads and thermal degradation, and the vehicle proceeded to separate from the starboard to port side [88].

During accident reconstruction, the Object Re-entry Survival Analysis Tool (ORSAT) predicted entry heating was not sufficient to explain the observed damage, most notably the

burn-through in the aft flange area, boxed region shown in Figure 4.1 [88]. Analytical predictions from ORSAT estimated a heating rate an order of magnitude higher than the estimated peak aero heating experienced during the accident would have been required to cause the observable damage. These findings led to the consideration of other possible material interactions: shock-shock interaction and metal combustion. The focus of this paper is on the latter.

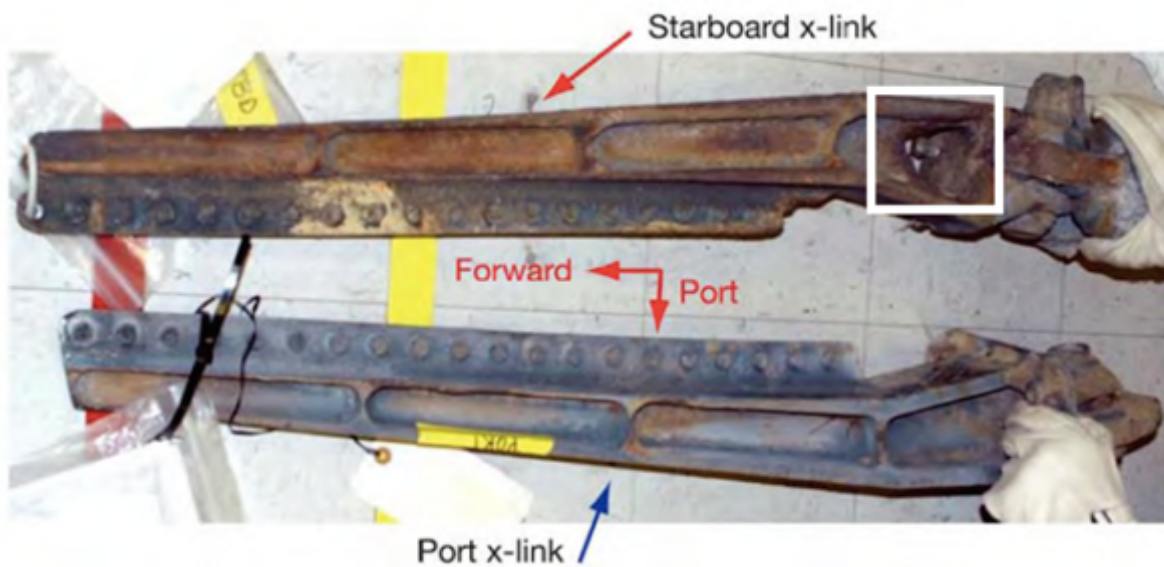


Figure 4.1. The X-links as recovered, top view, with box indicating burn through in the flange. From [3].

During the *Columbia* accident reconstruction, overhead windows from the forward fuselage were observed to contain a metallic deposit. This ‘char’ layer was found to be largely composed of metal oxides, and an oxidized layer composed of Ti-6Al-4V was deposited prior to that of an aluminum alloy [89]. Simply from the standpoint of relative melting temperatures between aluminum and titanium alloys, and given the larger overall weight percentage of aluminum alloy components comprising the shuttle construction, the observations from the overhead window char layer were puzzling. To determine the parameters which could account for these observations, an arc-jet test facility was utilized to simulate the oxygen rich, high

enthalpy, and low pressure re-entry environment to characterize the ignition and/or combustion response of Ti-6Al-4V [90]. Three different classifications of material responses were observed from arc-jet testing: material passivation; ignition resulting in initiation of melting without sustained combustion; and, ignition with sustained combustion. The results of the arc-jet testing provide evidence that ignition and combustion are plausible phenomena for titanium alloys in the re-entry conditions the *Columbia* X-links were exposed.

Despite a relatively mature understanding of combustion involving gaseous and liquid fuels, knowledge regarding combustion of bulk metals is not as extensive. This is likely due to the many compounding factors affecting oxidation and combustion that complicate analysis, including purity, gas composition, pressure, velocity past the surface, state of subdivision, and previous processing [91]. Titanium is recognized as having a high heat of combustion, a high flame temperature and a high solubility for oxygen [37,92-93]. At higher temperatures above the beta transus (approximately 1950°F), the solubility of oxygen in titanium and the oxidation rate increase. Historical review of titanium testing at NASA, DOE, and DOD facilities [94] revealed that freshly-exposed titanium surfaces are known to react violently with gaseous oxygen, while oxygen-deficient test streams did not result in ignition. Titanium was also found to combust vigorously in ambient-pressure gaseous nitrogen, with higher pressures contributing to decreasing ignition temperatures. Ti-6Al-4V has exhibited an exothermic oxidation reaction on fresh surfaces that leads to formation of oxides with evolution of a large amount of heat and ignition [54-55,95-96]. At high oxidation rates, as would be expected in a re-entry environment, the heat of reaction will not dissipate quickly and the material will begin to burn. These studies explored varying geometries, angles of attack and methods to achieve ignition, illustrating the complexity of compounding factors that must be considered.

The *Columbia* X-links themselves have a complicated geometry, and exhibit two distinct flow patterns, suggesting that various stages of oxidation and combustion were likely occurring simultaneously. Given the extensive use of titanium alloys as structural components in modern aerospace vehicles, consideration for accelerated thermal degradation due to exposure of these

alloys to the re-entry environment should not be neglected. Detailed materials characterization of the *Columbia* X-links will advance the understanding of titanium reactivity in the extreme environment of atmospheric re-entry.

4.2 METHODS

Surface and cross-sectional analyses were performed using light optical microscopy, and scanning electron microscopy (SEM) in conjunction with energy dispersive spectroscopy (EDS). Figure 4.2 shows post-sectioning regions of interest with the dotted line and arrow indicating the sectioning location and observation orientation of the metallographic sample.

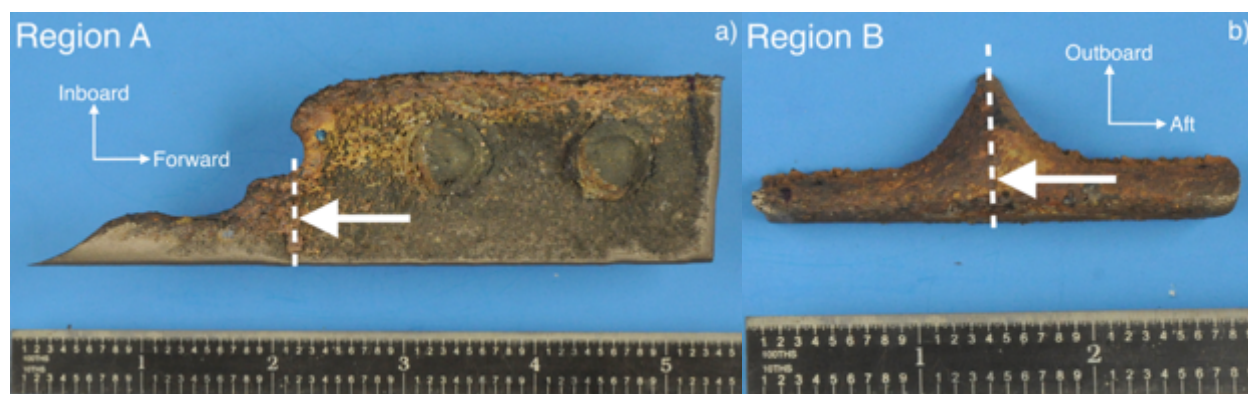


Figure 4.2. Top view of Regions A (left) and B (right).

4.3 RESULTS AND DISCUSSION

4.3.1 Region A

The overall surface is globular, flaky, and discolored. Localized regions of blue-tinted material underneath the flaky orange discoloration were observed, which was determined via EDS to consist primarily of titanium and oxygen (Figure 4.3). Trace detections of chromium, cobalt, iron, and nickel were also found, and attributed to contamination or transfer of material from the associated fasteners or other surrounding vehicle components. Blue-tinting is indicative of an oxide layer of the Ti-6Al-4V surface, while the orange discoloration could be indicative of a thinner oxide layer, or a foreign material deposit [97]. The flaking and evidence of separate oxidation colors suggest multiple deposition events and varying extents of oxidation, though of

note is that EDS of the overall surface chemistry was dominated by detections of titanium and oxygen, with only trace detections of elements consistent with the MP35N fasteners.

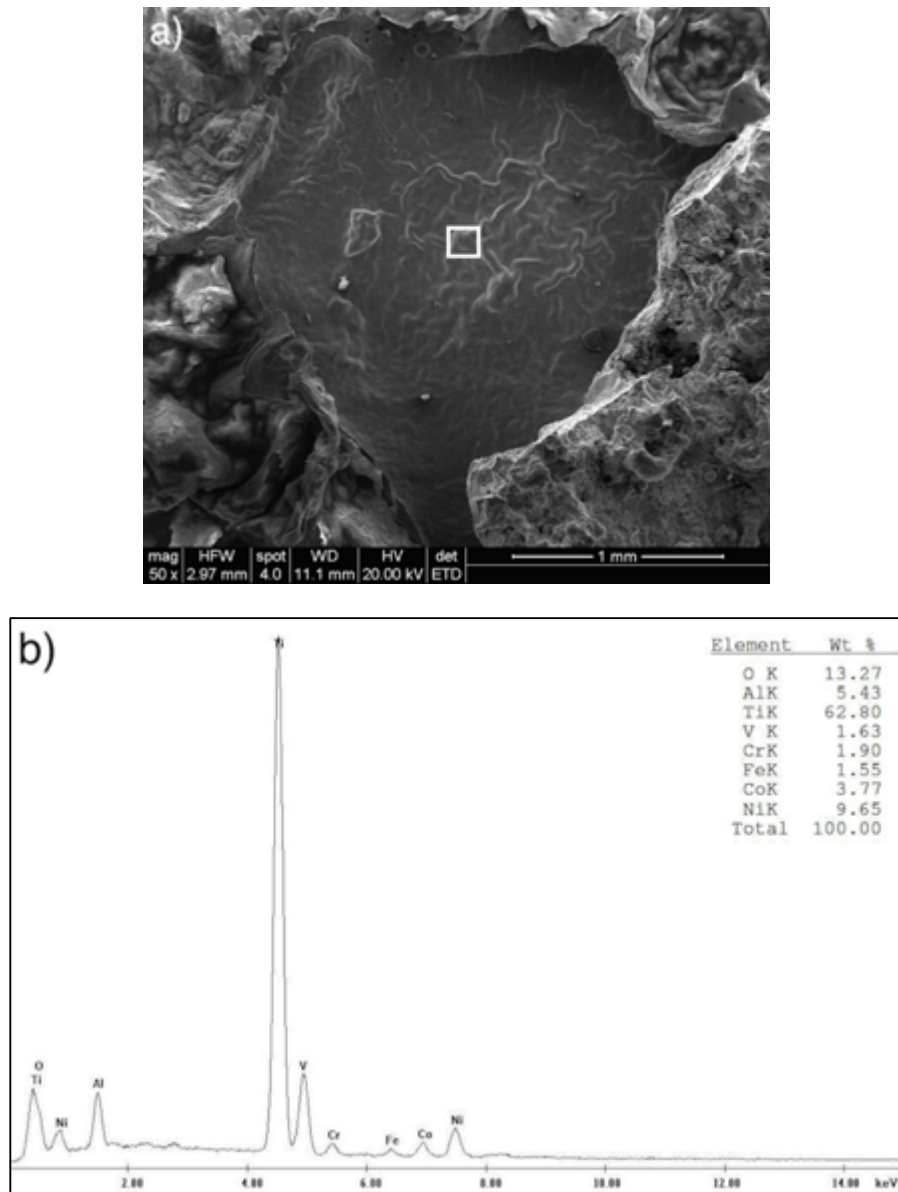


Figure 4.3. a) Secondary electron image of blue-tinted region with boxed area indicating EDS scan area; b) EDS spectrum obtained from the blue-tinted region

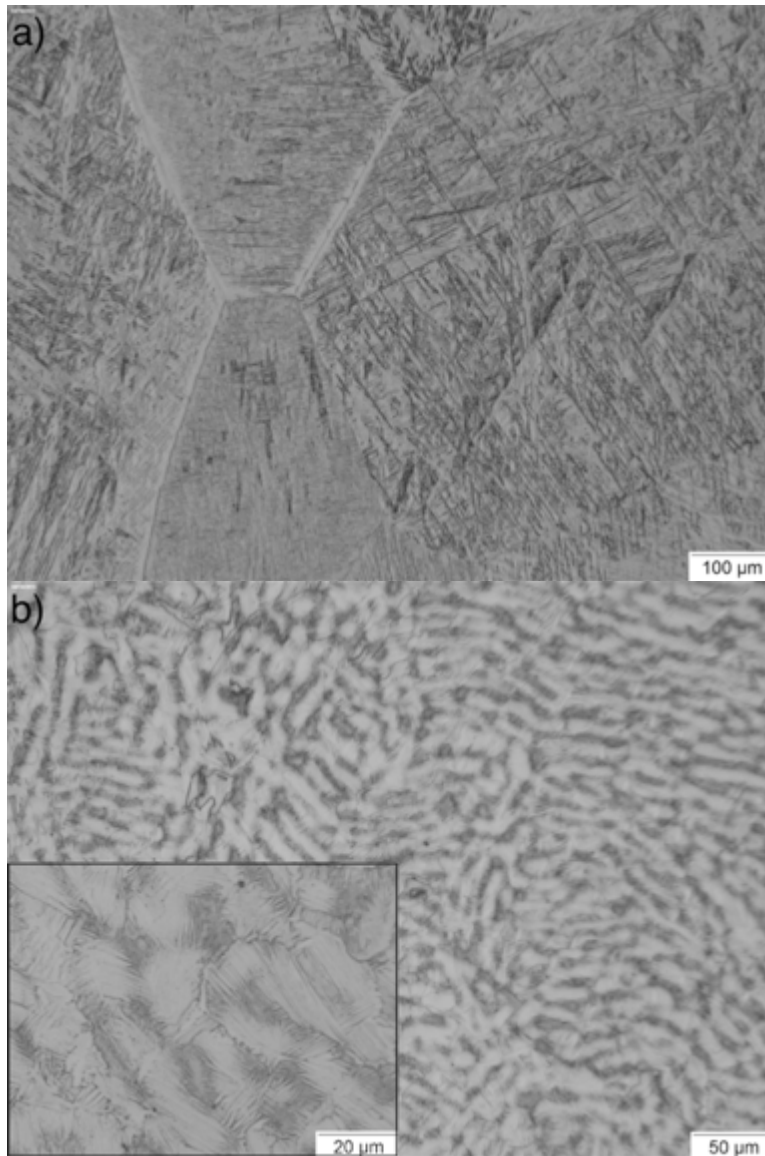


Figure 4.4. Inboard (a) and outboard (b) microstructures. Kroll's reagent.

Microstructural analysis (Figure 4.4) revealed a grain size gradient, with larger grains at the inboard side and progressively smaller grains towards the outboard side. The inboard microstructure shows a martensitic alpha prime structure in prior beta grains, while the microstructure of the outboard material exhibited a basketweave structure with diffuse beta forming between elongated acicular alpha prime colonies. The microstructures suggest that the outboard material in region A was above the beta transus temperature, and the inboard side was

hotter than the outboard side. Both sides appear to have cooled rapidly by some change in atmospheric conditions, as demonstrated by the martensitic alpha prime structure.

Cross-sections of Region A revealed several deposition layers on the base material, as well as oxide cracking, gas porosity and shrinkage porosity within the layers. Figure 4.5 illustrates a deposition layer found on the inboard underside of the shuttle. Pink-tinted depositions, shown optically in Figure 4.5a, were observed. EDS spot scans were performed to determine the composition of different layers, with scans one and two represented in Figure 4.6. Scan one revealed the solid pink layer consisted primarily of titanium and oxygen. Scan two focused on apparent solidification structures found throughout the deposit, which itself consisted primarily of titanium. The dark deposit in scan three was found to be titanium rich and similar to scan two. Lastly, the lightest phase consisted largely of titanium, and in addition, had small amounts of iron, nickel, and cobalt. Scan two and three exhibit similar spectra, but were obtained from regions with optically different microstructures.

Evidence shows that multiple layers were depositing simultaneously. It is noted that the pink layer and the layer surrounding the droplet of material appear different optically, but similar in the electron images. This may be attributed to differences in titanium oxide stoichiometry, leading to different structures that change the interactions with light. The strongly oxidized layers of titanium could be a result of localized thermal erosion causing the dislodging and transport of material, the X-link flying through a molten debris cloud, or molten titanium being expelled from the surface in the case that the protective oxide layer cracked. The break-up environment was dynamic and therefore similar layered phases are observed but are not identical.

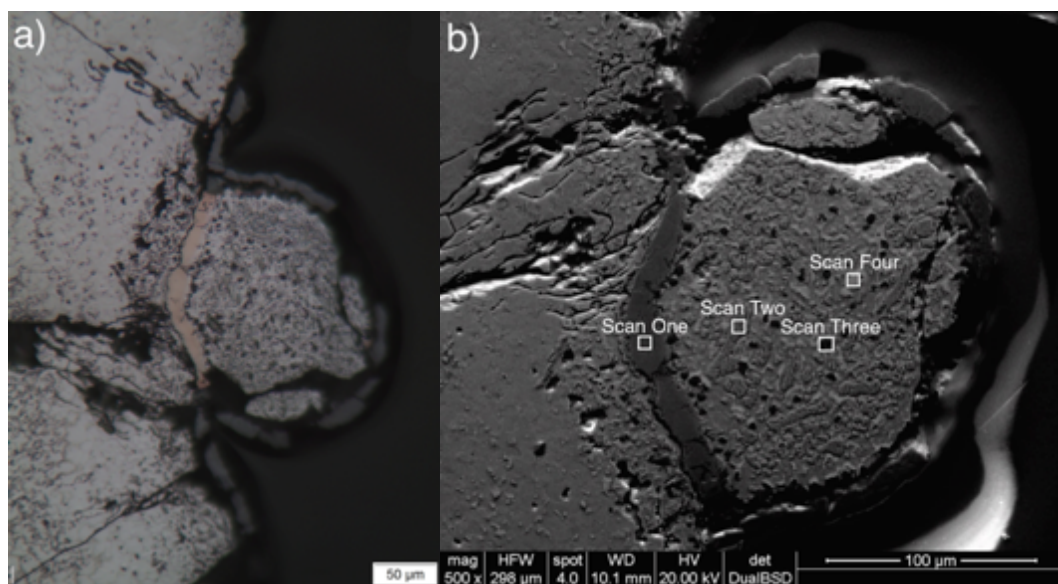


Figure 4.5. a) Optical image of deposition layer (Kroll's); and, b) Backscattered electron image of deposition layering in Region A (boxes indicating selected areas for EDS spot analysis).

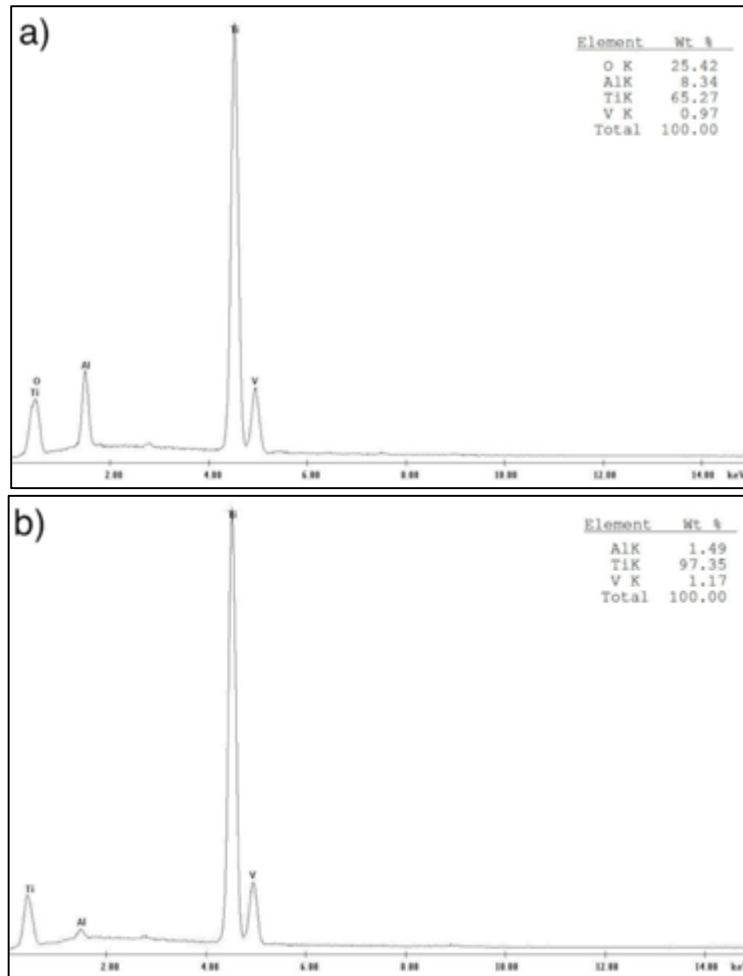


Figure 4.6. EDS spectra from a) Scan One, and b) Scan Two from Region A.

4.3.2 Region B

Surface analysis performed on all orientations of Region B revealed significant porosity, with many features suggesting porosity was associated with solidification shrinkage (Figure 4.7). All surfaces had a globular appearance, with oxide cracking, flaking of oxide layers, and orange and brown discoloration. EDS spectra across all surface orientations revealed detections of silicon, oxygen, and nitrogen, in addition to the Ti-6Al-4V alloy constituents. Specifically, the top surface had several silicon particles embedded within the pores. The inboard surface, nearest the bolts, had EDS detections of elements consistent with MP35N. The outboard surface had

many embedded particles rich in carbon that may have originated from the X-link impacting the ground after the accident.

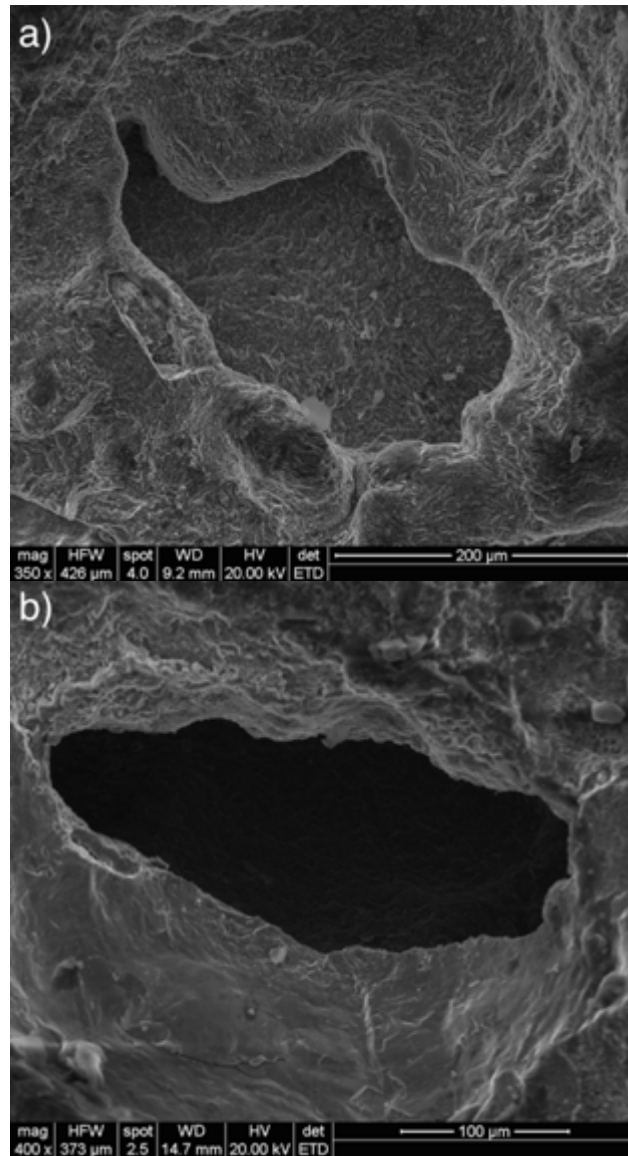


Figure 4.7. a) Secondary electron image of porous surfaces resembling shrinkage porosity from surface, top surface and b) Secondary electron image of porosity, top surface

The inboard microstructure shown in Figure 4.8a is characterized by large prior beta grain boundaries containing acicular alpha prime on the inboard side. The microstructure in Figure 4.8b has a basketweave structure with a diffuse beta occurring between elongated alpha

prime colonies, with some retained primary alpha, on the outboard side. Region B also appears to have been rapidly cooled in a process similar to quenching, as inferred from the martensitic structure. The microstructures suggest that Region B was exposed to a lower temperature than Region A, owing to the smaller grains and presence of retained primary alpha. It is likely that the outboard side of Region B remained slightly below the beta transus, because of the retained primary alpha.

Cross-sectional analysis revealed the depositions appear more porous, as shown in Figure 4.9. EDS showed that the porous material is titanium oxide rich, and the inclusions are silicon and oxygen rich (Figure 4.10). The silicate nearest the surface likely underwent a different deposition process than the silicate deeper inside the surrounding material, indicated by the strongly oxidized titanium encapsulation. Similar silicon and oxide rich particles were embedded along the surface, suggesting that this region of the X-link came into contact with portions of the vehicle thermal protection system. Layers with a pink tint similar those observed in Region A were also seen in Region B, but were not as abundant.

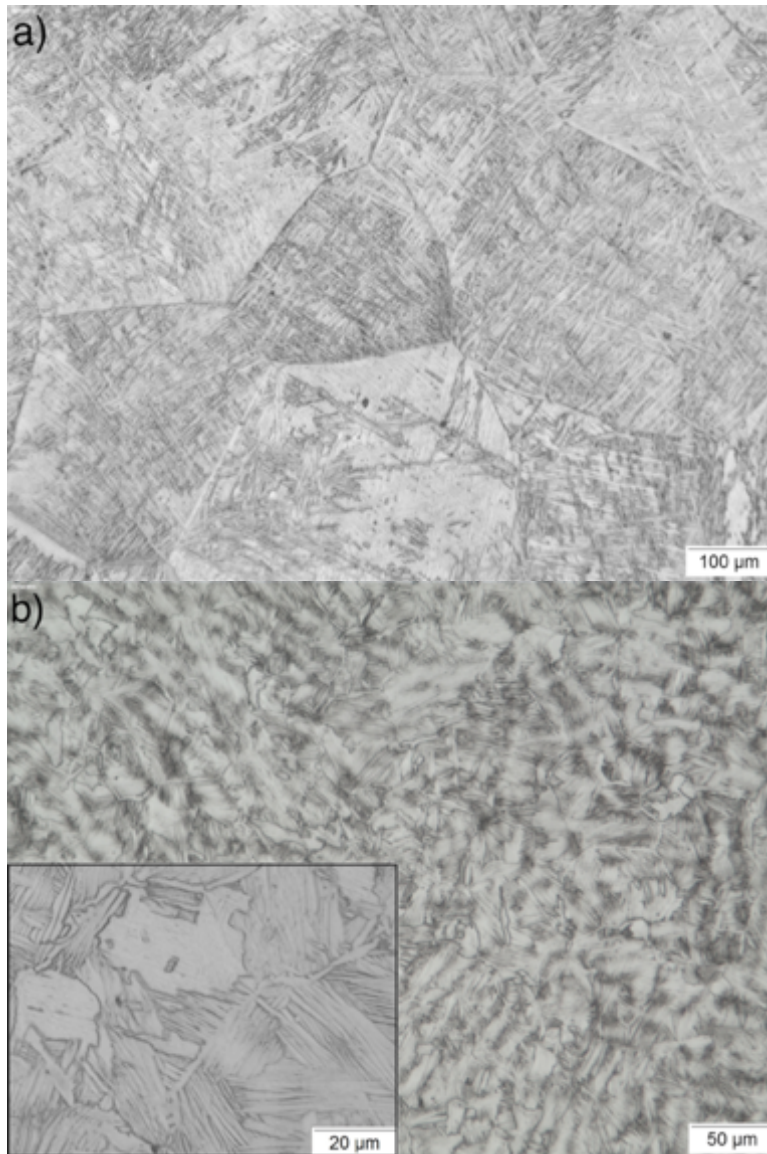


Figure 4.8. Inboard (a) and outboard (b) microstructures from Region B. Kroll's reagent.

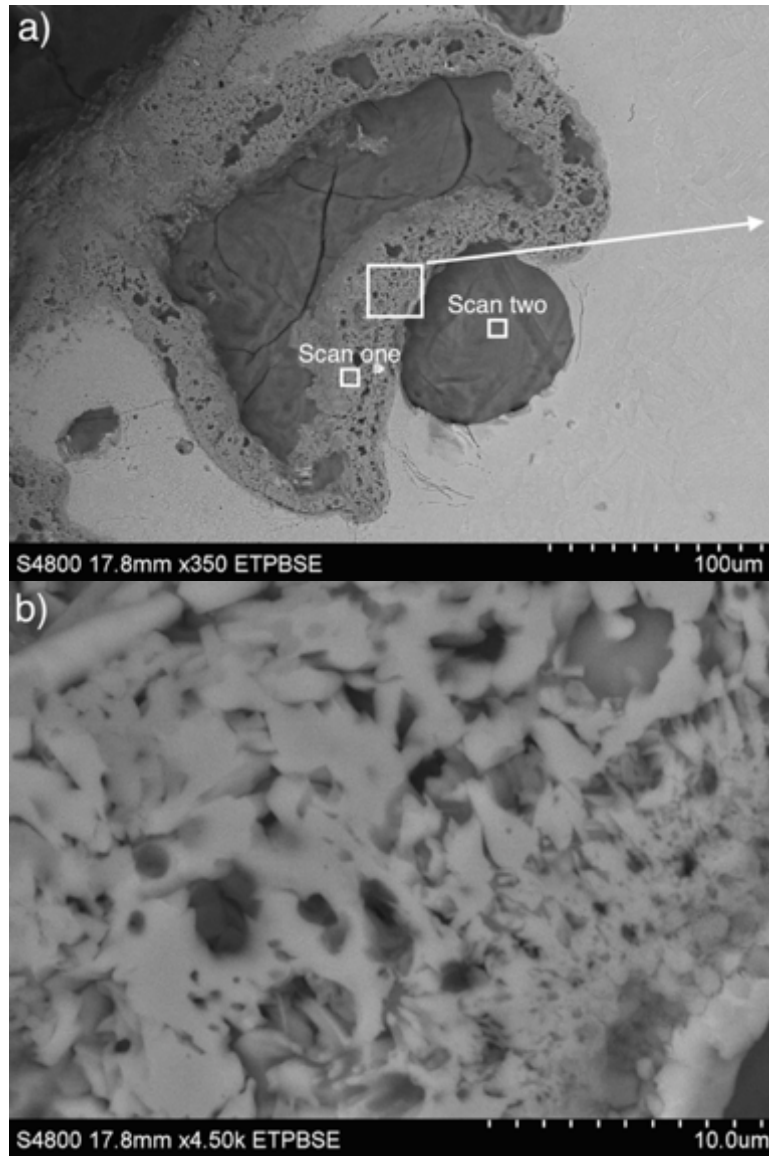


Figure 4.9. Backscattered electron image of outboard deposit (b), with higher magnification image of porous layer surrounding the large inclusion particles.

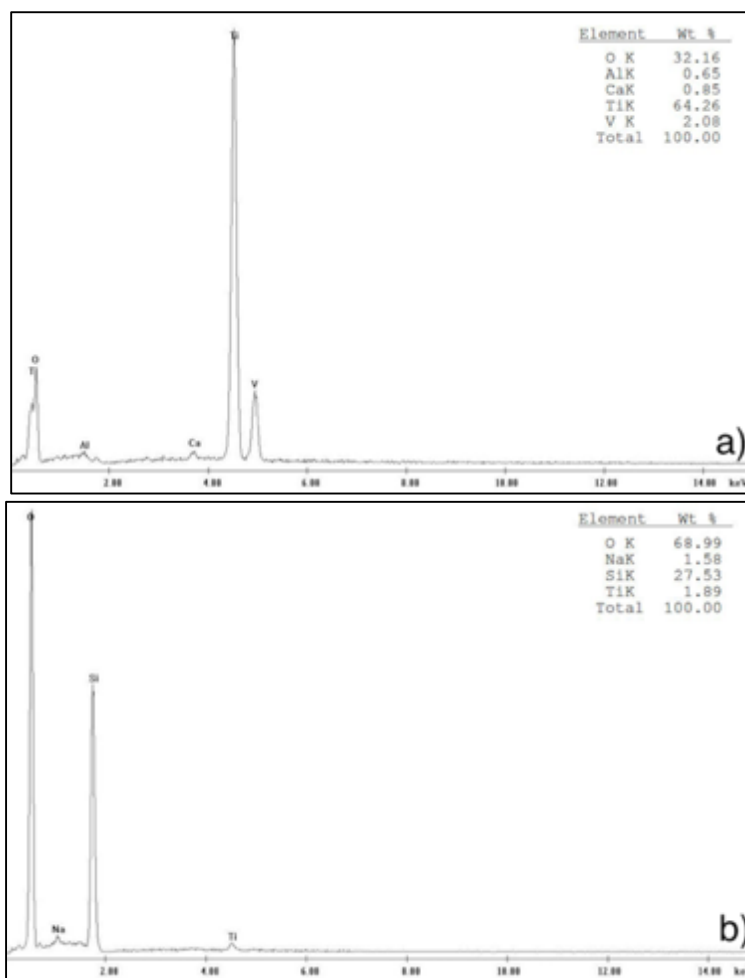


Figure 4.10. EDS spectra from a) Scan One, and b) Scan Two from Region B.

4.4 CONCLUSIONS

Surface and cross sectional EDS analysis found varying amounts of Ti-6Al-4V constituents, foreign material, oxygen, and nitrogen, with the main elements as titanium and oxygen. The microstructures suggest exposure temperatures both above and below the beta transus. Porosity, oxide cracking, and multi-step deposition processes were observed.

The evidence suggests that titanium was responding aggressively to the environment during the re-entry event. Further research will focus on characterization of samples that ignited and combusted using arc-jet testing and results will be compared to data from the X-links. This comparison will help to determine if ground-based testing methods to simulate re-entry are

sufficiently representative of the actual environment to encompass conditions supportive of metal combustion. Because the arc-jet testing parameters are relatively well characterized, it is possible to make inferences on the unknown parameters of the actual re-entry environment based on the known parameters of the arc-jet in the case that any similarities are found. This and future research aims to develop a clearer understanding of material interactions in the extreme environment of atmospheric re-entry.

4.5 ACKNOWLEDGEMENTS

The authors would like to thank the *Columbia* Research and Preservation facility office at Kennedy Space Center, John D. Olivas, Christopher Bradley, Shalayna Smith, and Alejandro Hinojos for their support.

Chapter 5: Investigation into the response of Ti-6Al-4V alloy to atmospheric re-entry exposure

5.1 INTRODUCTION

Ti-6Al-4V is a common aerospace alloy utilized for its high strength-to-weight ratio, corrosion resistance, and high operating temperature capabilities [15]. Yet, research has shown that practically every commercial titanium alloy can ignite [53]. Despite a relatively mature understanding of combustion involving gaseous and liquid fuels, knowledge regarding combustion of bulk metals is not as extensive. This is likely due to the many compounding factors affecting oxidation and combustion that complicate analysis, to include purity, gas composition, pressure, velocity past the surface, state of subdivision, and previous processing [12]. Titanium is recognized as having a high heat of combustion, a high flame temperature, and a high solubility for oxygen [17,37-38,98]. The high heat of combustion of titanium is related to its relatively modest thermal conduction properties when compared to other structural aerospace alloys. Conduction of heat within a material as it affects surface temperature is an important factor in ignition [18]. With a lower thermal conduction and thus lower thermal inertia in the material, the surface temperature will rise more quickly and lead to the creation of a “hot spot”, in which a localized ignition reaction can occur. The reactivity of titanium is also attributed to the high solubility for oxygen within titanium [99]. At temperatures above the β -transus (approximately 1950°F), the solubility of oxygen in titanium and the oxidation rate increase. Similarly, an increase in pressure has proven to lower the critical temperature necessary for ignition [40]. Historical review of titanium testing at NASA, Department of Energy (DOE), and Department of Defense (DOD) facilities [98] revealed that freshly exposed titanium surfaces are known to react violently with gaseous oxygen, while oxygen deficient test streams did not result in ignition. Titanium was also found to combust vigorously in ambient pressure gaseous nitrogen, with higher pressures contributing to decreasing ignition temperatures. Ti-6Al-4V has exhibited an exothermic oxidation reaction on fresh surfaces that leads to the formation of oxides with the evolution of a large amount of heat and ignition [53-56]. At high oxidation rates, as

would be expected in a re-entry environment, the heat of reaction will not dissipate quickly enough and the material will begin to burn. These studies explored varying geometries, angles of attack, and methods to achieve ignition, illustrating the complexity of compounding factors that must be considered.

On February 1st, 2003, NASA's Space Shuttle *Columbia* endured a catastrophic failure during re-entry into Earth's atmosphere. Ultimately, all seven crew members lost their lives in this tragic event. Root-cause analysis determined that a breach of the reinforced carbon-carbon (RCC) leading edge of the port wing was caused by a piece of insulating foam that detached from the external fuel tank during lift-off. This breach allowed superheated gas ingestion into the vehicle during re-entry, which ultimately degraded the substructural components and integrity of the space shuttle [1].

The X-links, a substructural component composed of Ti-6Al-4V that connected the crew module, forward fuselage, and mid-body structures of the vehicle in the longitudinal direction, were identified as a component of interest due to the physical features observed. The X-links were secured to the shuttle structures with fasteners made of MP35N, a nickel-cobalt-chromium-molybdenum alloy trademarked by SPS technologies. The as-received port and starboard X-link are shown in Fig. 5.1 as they were configured within the space vehicle. Upon recovery of the X-links after the accident, the starboard X-link exhibited thermal degradation patterns that could not be explained by re-entry alone. Relative to the port X-link, the starboard X-link exhibited more mass loss, discoloration, and is missing the aft-most fastener. The fastener heads exhibit evidence of exposure to forward-to-aft flow conditions, while the webbing of both X-links contain evidence of exposure to aft-to-forward flow conditions. Structural debris analysis suggests that initial failure occurred immediately aft of the starboard X-link from a combination of structural loads and thermal degradation, and the vehicle proceeded to separate from starboard to port side [3]. Despite similar flow patterns, the starboard X-link was recovered in the forebody debris field and the port X-link in the midbody debris field; this separation is theorized to have occurred after the combustion event.

In terms of vertical temperature, there are four atmospheric layers. In order of increasing altitude is the troposphere, stratosphere, mesosphere, and thermosphere. Modeling results published in NASA's Columbia Crew Survival Report indicate that breakup of Columbia occurred in the mesosphere, between 180-210 thousand feet altitude [3]. In the mesosphere, low temperatures prevail and molecular oxygen and nitrogen still compose 99% of the air, with virtually the same mixings as air at sea level (78% N₂, 20.9% O₂) [2]. The high velocities produced by vehicle deceleration can result in the dissociation of O₂ and N₂ gases, converting the species to their atomic forms. The presence of atomic nitrogen and oxygen create a more aggressive environment in which oxidation and combustion are accelerated.

During accident reconstruction, NASA's Object Re-entry Survival Analysis Tool (ORSAT) predicted entry heating alone was not sufficient to explain the observed damage, most notably the burn through in the flange area [3]. In order to cause the observed damage, analytical predictions from ORSAT estimated a required heat rate an order of magnitude higher than the maximum peak aero heating the vehicle could have experienced. These findings led to the consideration of other possible material interactions: shock-shock interaction and metal combustion. The focus of this research is on the latter.

During *Columbia* accident reconstruction, overhead windows from the forward fuselage were observed to contain a metallic deposit. This 'char' layer was found to be largely composed of metal oxides, and an oxidized layer of Ti-6Al-4V was deposited prior to that of an aluminum alloy [7]. Simply from the standpoint of relative melting temperatures between aluminum and titanium alloys, and given the larger overall weight percentage of aluminum alloys comprising the shuttle construction, the observations from the overhead window char layer were puzzling. To determine parameters that could account for these observations, an arc-jet test facility was utilized to simulate the oxygen rich and high enthalpy re-entry environment to characterize the ignition and/or combustion response of Ti-6Al-4V [100]. Arc-jet testing represents the best ground-based simulation of a re-entry environment by providing the ability to explore the oxidation behavior of materials under extreme conditions [4]. The arc-jet is a high altitude,

hypersonic wind tunnel facility that heats and accelerates O₂ and N₂ gases through a nozzle onto the surface of a sample [5]. Three different classifications of material response were observed from arc-jet testing (Fig. 5.2). Class I represents material passivation, Class II represents ignition and initiation of melting with no combustion, and Class III represents ignition with sustained combustion. It should be noted that ignition and combustion only occurred when there was a protuberance of the sample from the mount, thus causing the test coupon to have a higher effective ballistic number. In cases where the test coupon was mounted without protuberance, only the Class I oxidation response was observed. Because the X-links have a complicated geometry and thus a high effective ballistic number, it is likely that many separate oxidation and combustion states were occurring simultaneously. The results of the arc-jet testing provide evidence that ignition and combustion are plausible phenomena for titanium alloys in certain re-entry conditions.

A forensic materials characterization study of two separate Ti-6Al-4V components that have been exposed to re-entry conditions, both actual and simulated, will further the understanding of bulk metal combustion in the extreme environment. Qualitative and quantitative correlations will be made between the X-links and the arc-jet samples in an effort to relate the known parameters of testing to the unknown parameters of the X-links re-entry into the atmosphere. This comparison will help to determine if ground-based testing methods are sufficiently representative of the actual environment to encompass conditions supportive of metal combustion. These results will also aid in differentiating separate material reactions in an effort to identify the mechanism of Ti-6Al-4V combustion in a re-entry environment.

Given the extensive use of titanium alloys as structural components in modern aerospace vehicles, consideration for the accelerated thermal degradation due to exposure of these alloys to the re-entry environment should not be neglected. The aerospace community must be aware of a well-predicted and graceful degradation of materials being sent into space. Detailed materials characterization of the *Columbia* X-links and arc-jet samples will advance the understanding of titanium reactivity in the extreme environment of atmospheric re-entry.



Figure 5.1. As-received photographic documentation of the port and starboard X-links.



Figure 5.2. The three different classifications of material response observed from arc-jet testing.

5.2 METHODS

Metallography and Light Optical Microscopy (LOM), Scanning Electron Microscopy (SEM), Energy Dispersive X-ray Spectroscopy (EDS), X-ray Diffraction (XRD), and microhardness testing were used to characterize the material. A significantly degraded region of the starboard X-link, located on the aft side, immediately next to the aft-most burned off fastener, was chosen for analysis; two metallographic sections were taken from this region (Fig. 5.3). For comparison, the metallic portions of two arc-jet samples, one Class II and one Class III, were analyzed with complementary methods (Fig. 5.4). Dotted lines indicate secondary sections, and arrows indicate observation orientation of the metallographic samples. For ease of explanation, the X-link and arc-jet samples will be referred to as samples 1-4, as described in Tab. 5.1.

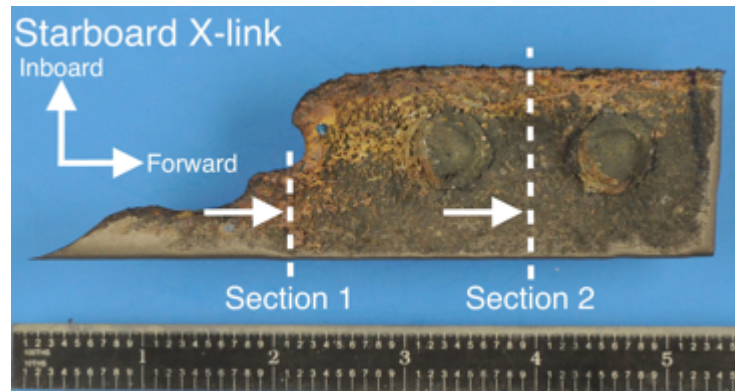


Figure 5.3. Starboard X-link region of interest with numbered sections.

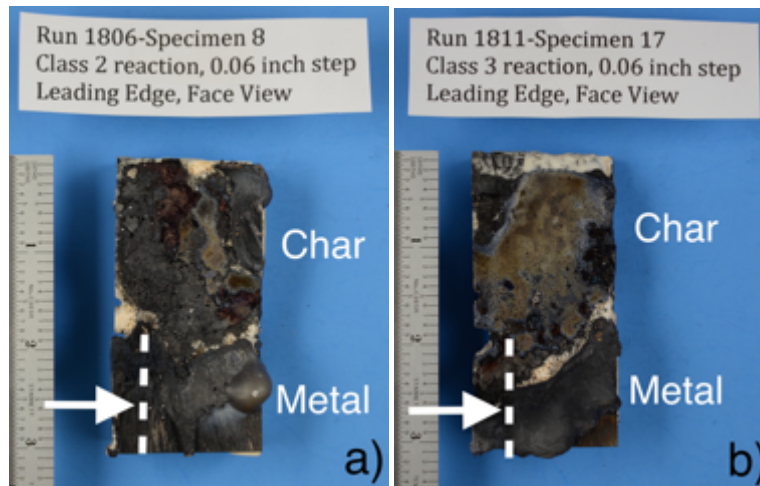


Figure 5.4. Class II (a) and Class III (b) arc-jet samples.

Table 5.1. Nomenclature of samples discussed in paper.

Sample No.	Source: X-link or Arc-jet	Additional Information
1	X-link	Section 1 (Fig. 5.3)
2	X-link	Section 2 (Fig. 5.3)
3	Arc-jet	Class II (Fig. 5.4a)
4	Arc-jet	Class III (Fig. 5.4b)

5.3 RESULTS

While the purpose of this work is to correlate material responses from the simulated and actual re-entry environments, it is necessary to make some distinctions between intrinsic differences that exist. The history of the X-links, to include temperature exposure and initial microstructural state, are unknown. Therefore, assumptions about the history are made based upon observations on the macro and micro scale. As the position of the X-links decreased in altitude it is likely that they experienced a variable cooling rate as it transitioned through the atmospheric levels. Ballistic heating, exothermic reactions occurring near the X-links, and other heat sources could have also influenced temperature and cooling rate. The arc-jet samples essentially experienced an air quench upon removal from the arc-jet flow stream at the end of the test. Cooling rate directly affects the microstructure. Geometrical variations between the X-links and arc-jet samples could have affected observations. The arc-jet samples originate from 1/8 inch, uniform thickness metal plate while the X-links were geometrically complex parts with varying thicknesses up to 3 inches. The thinnest, 1/4 inch, sections of the X-links were examined and compared to the arc-jet samples. The X-link samples examined within this paper transitioned to a thicker geometry nearest the outboard side. The conductive heating effects from the thicker material may have caused the material nearest the outboard side to remain hot for longer periods of time, converse to the relatively uniform cooling rate of the arc-jet samples. Contamination from surrounding material systems for both arc-jet and X-link samples also exists. The X-links were surrounded by several material systems comprising the shuttle, and the arc-jet samples were fixed to a SiC ceramic plate. As illustrated, several different factors are present which could influence the characterization results.

References to the relative flow directionality observed on the X-links will be attributed to the similar characteristics observed on the arc-jet samples. Physical features on the X-links suggest that flow originated from the inboard side. The configuration of the arc-jet creates a leading and trailing edge on tested specimens. Throughout this work, inboard and leading edge features will be referred to in terms of forward facing flow, while outboard and trailing edge features will be referred to in terms of back facing flow. Discrete changes in features are observed with arc-jet samples, while more pronounced transitions are described for the X-link samples.

5.3.1 Microstructural Features

In order to evaluate the effects of the combustion reaction on the microstructure, it is helpful to know the initial microstructural state. The initial microstructure of the arc-jet samples, taken from untested metal plate, was a fine-grained bimodal structure of slightly elongated α in a lamellar α/β matrix (Fig. 5.5), a sub- β transus structure. Assigning an initial microstructural state to the X-links without any processing history was a more difficult task, for which the following method was used. To mitigate heat effects in the material, metallography was performed on the thickest cross-sections (~1 inch) on both the port and starboard X-link in the same relative location away from any extreme thermal effects (Fig. 5.6). The port X-link, possessing minimal thermal degradation and mass loss, contained a bimodal structure, with elongated α in a lamellar α/β matrix. The starboard X-link contained transformed β with platelike α and more clearly defined prior β grain boundaries. The port X-link suggests a sub β transus temperature exposure while the starboard X-link suggests exposure above the β transus. The initial state of the arc-jet samples is similar to the microstructure observed on the port X-link, though arc-jet has a finer grain size. The port microstructure is believed to adequately represent the original microstructural state of the X-links, and the starboard section appears to be moderately heat affected. The microstructures in both port and starboard X-link were uniform and no gradients were observed.

Forward facing flow microstructural features were similar for all samples (Fig. 5.7), consisting of martensitic α prime within large prior β grains. Martensitic α formation occurs with a quick cooling rate, as in quenching. Grain sizes were comparable though not identical in all samples. Smaller grains were observed in X-link sample 2 than X-link sample 1, possibly due to the closer proximity of sample 1 to more aggravated flow, evidenced by the burned off bolt immediately aft of the parent piece. X-link section 2 also exhibited martensitic and serrated α ; serrated α is typically observed in weld zones due to overheating [101] and when there is a rapid cool from the β phase field [102]. Oxygen enriched, α stabilized phases, referred to as α cases, were observed in all forward facing flow material, due to the high temperature diffusion of oxygen into the surface.

Back facing flow microstructural features differed between the samples (Fig. 5.8). X-link samples 1 and 2 possessed a microstructural gradient, exhibiting a basketweave structure of acicular α colonies in an aged, transformed β matrix with acicular α with some α islands dispersed in the structure.

The acicular α colonies are thinner, with a more defined β in sample 2 than sample 1. Cooling rate typically determines the thickness of α lamellae, suggesting that sample 2 cooled more quickly than sample 1. Sample 2 appears less thermally degraded, so it is plausible that the material in sample 1 was at a higher temperature prior to cooling, resulting in a slower cooling rate than sample 2. The acicular α microstructure appears to be an intermediate structure resultant from the transition from a martensitic α to the initial globular α observed in Fig. 5.5. Arc-jet sample 3 exhibited a less extreme microstructural gradient, with larger grains at the forward facing flow side, transitioning to slightly smaller grains at the back facing flow side. Serrated α grains were also observed. Arc-jet sample 4 did not exhibit a microstructural gradient and had a relatively constant grain size across the length of the sample consisting of acicular α within large prior β grains. The back facing flow side of arc-jet samples 3 and 4 did not transition to the intermediate acicular α structure as X-link samples 1 and 2 did. This is likely due to the geometry of the X-links versus the arc-jet samples. As discussed previously, it is plausible that conductive heating effects from thicker material in X-links sample 1 and 2, causing the back facing flow material to remain hot for longer, producing a microstructure corresponding to a lower cooling rate than the forward facing flow material.

The absence of a microstructural gradient in sample 4 (a Class III reaction) may rely on several factors. One possibility relates to the large consumption of titanium metal during testing for Class III combustion reactions. The Class III samples often had molten material encompassing the entirety of the remaining metal, causing the metal to remain at a higher temperature longer and produce even cooling within the metal. It is also possible that arc-jet sample 4 reached some critical threshold where uniform heating was established, resulting in the absence of a microstructural gradient. Arc-jet sample 3, a Class II reaction, has a slight microstructural gradient, thought to be negligible due to the martensitic α and large grained structure retained throughout. X-link samples 1 and 2 were not able to reach this even heating state due to the close proximity of thicker Ti-6Al-4V material connected to the back facing flow material.

Microstructural features are dependent on many processing parameters. A higher cooling rate from the β phase field results in smaller α colony size, α plate width, and thickness of α at grain

boundaries for the lamellar microstructures observed. [17]. Longer times at temperatures above the β -transus result in a higher percentage of β in the microstructure. Larger β grain sizes result from high solutionizing temperatures. Because exact parameters are not known for the temperature exposure of the X-links, it is difficult to ascertain what parameter caused each microstructural characteristic.

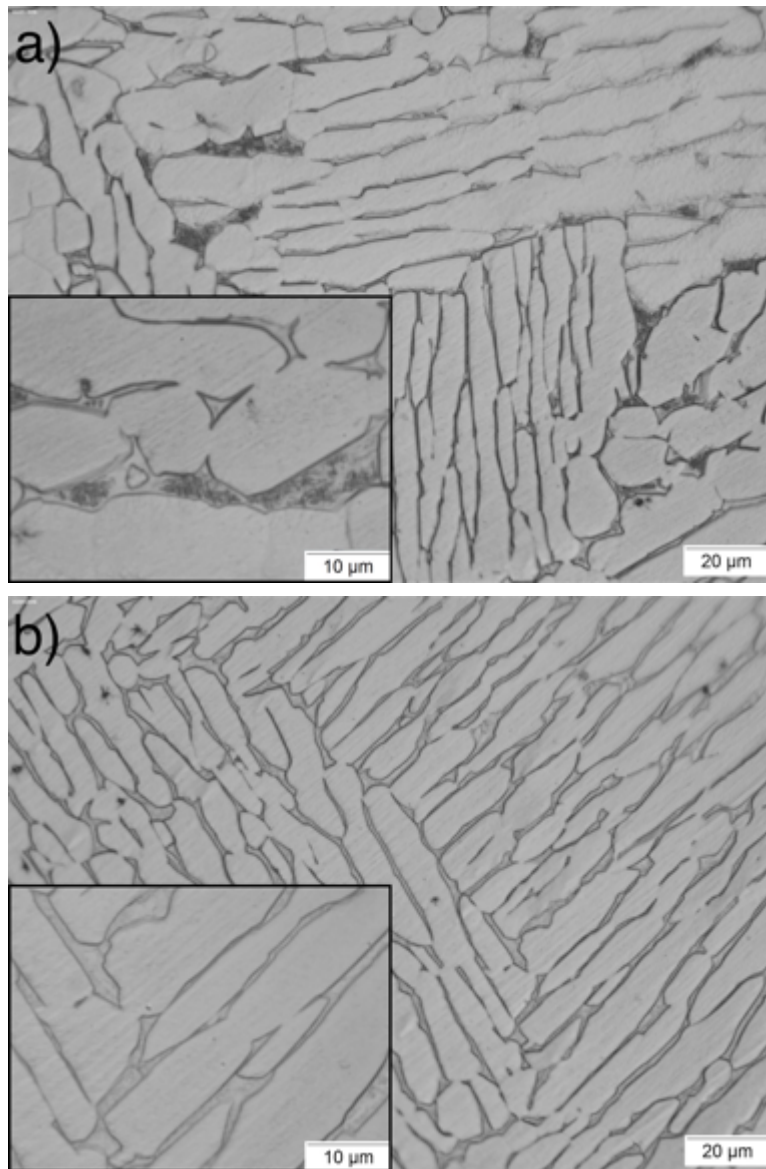


Figure 5.5. Complementary microstructures through thickest section of port (a) and starboard (b) X-links.

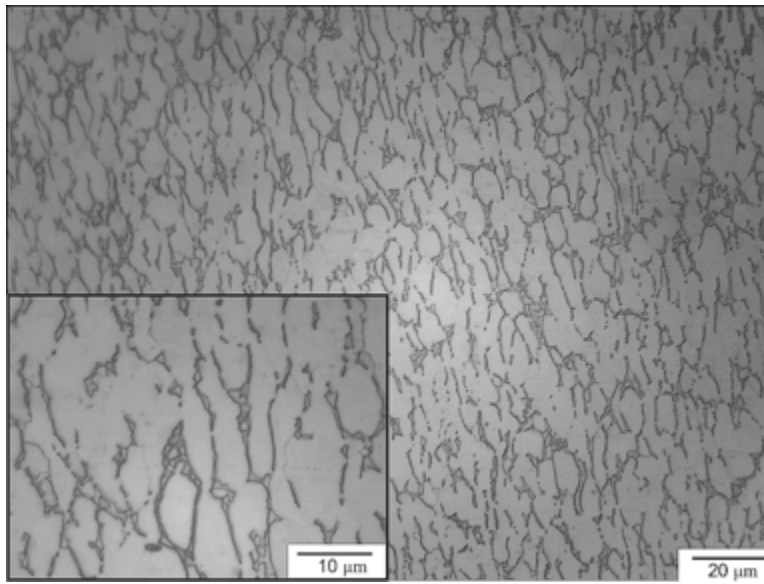
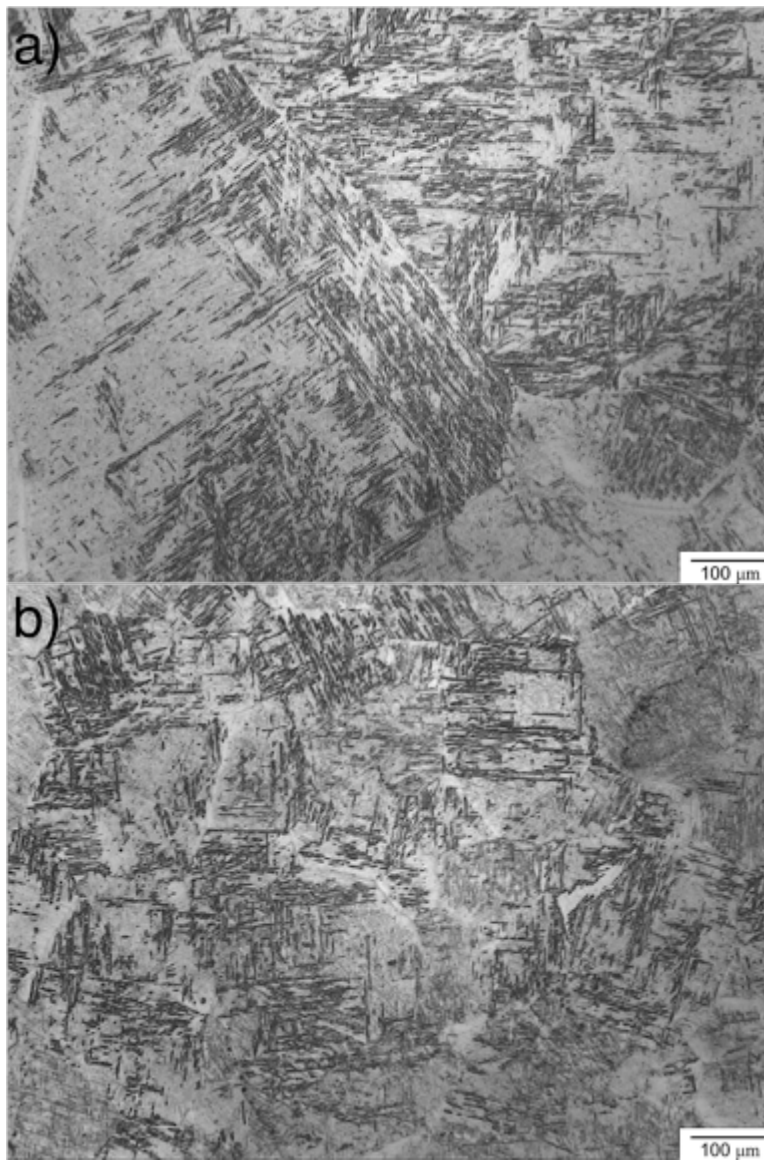


Figure 5.6. Initial microstructural state of the arc-jet samples.



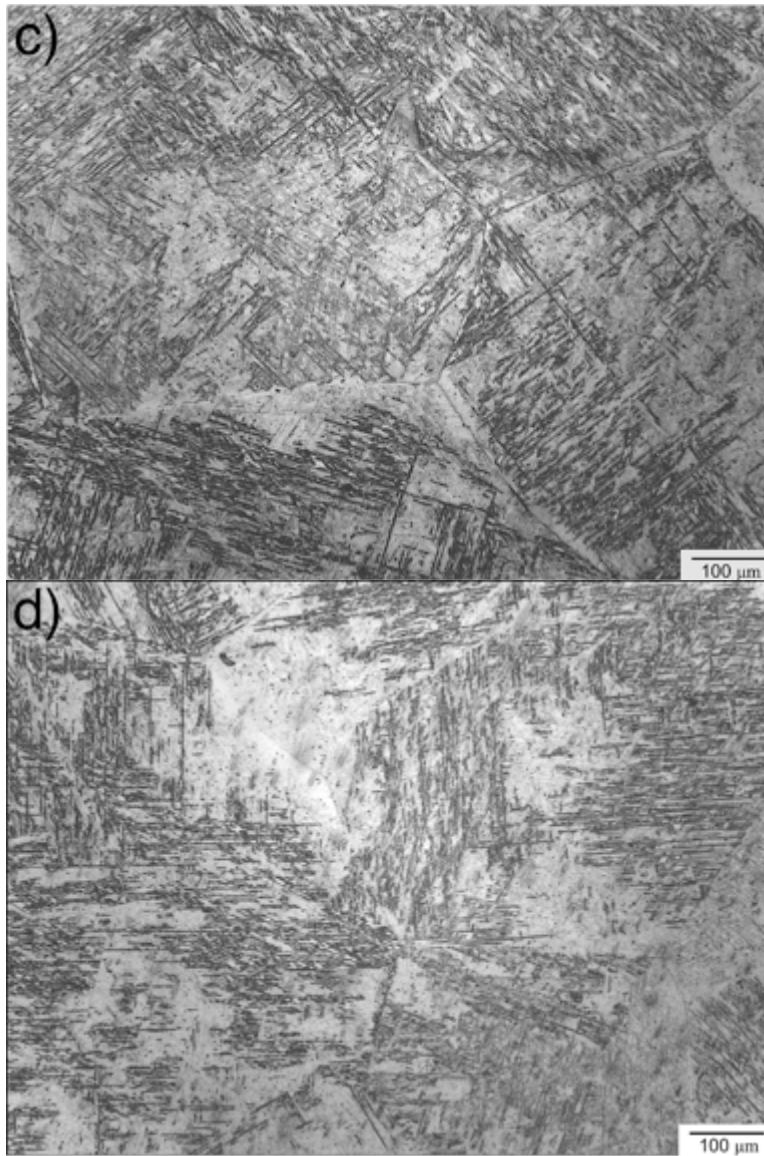
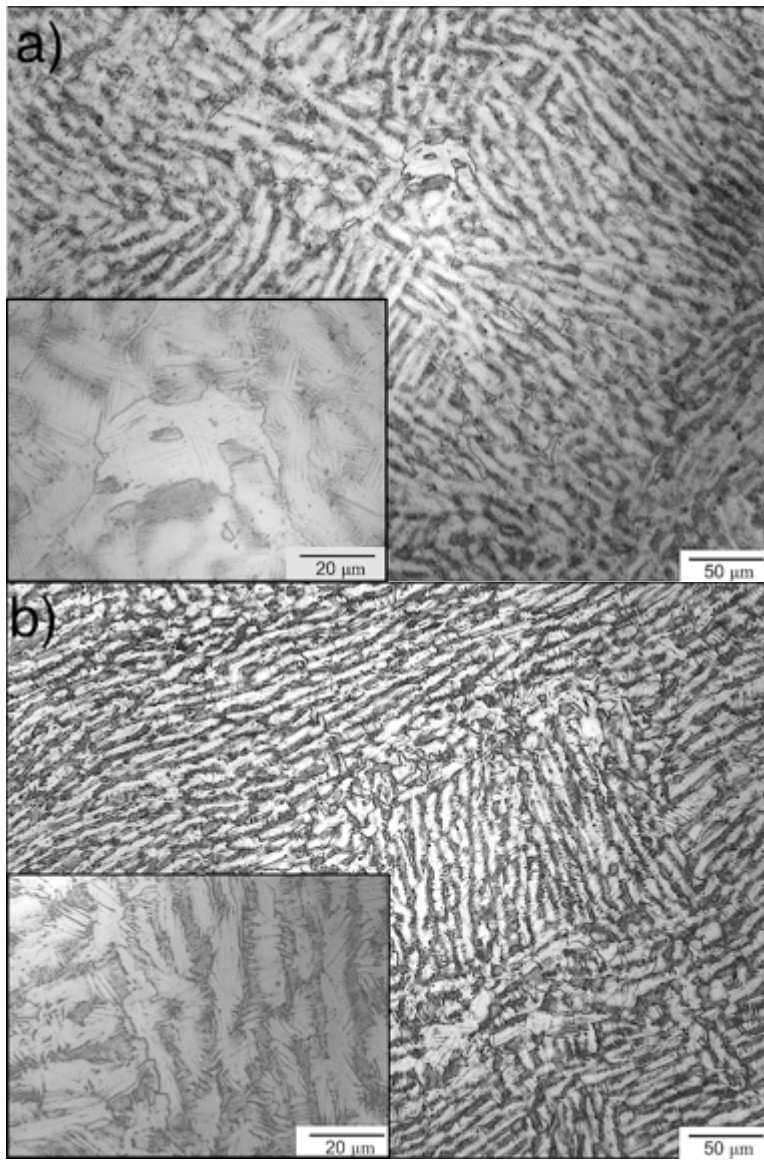


Figure 5.7. Forward facing flow microstructures for starboard X-link section 1 (a), starboard X-link section 2 (b), arc-jet sample Class II (c), and arc-jet sample Class III (d).



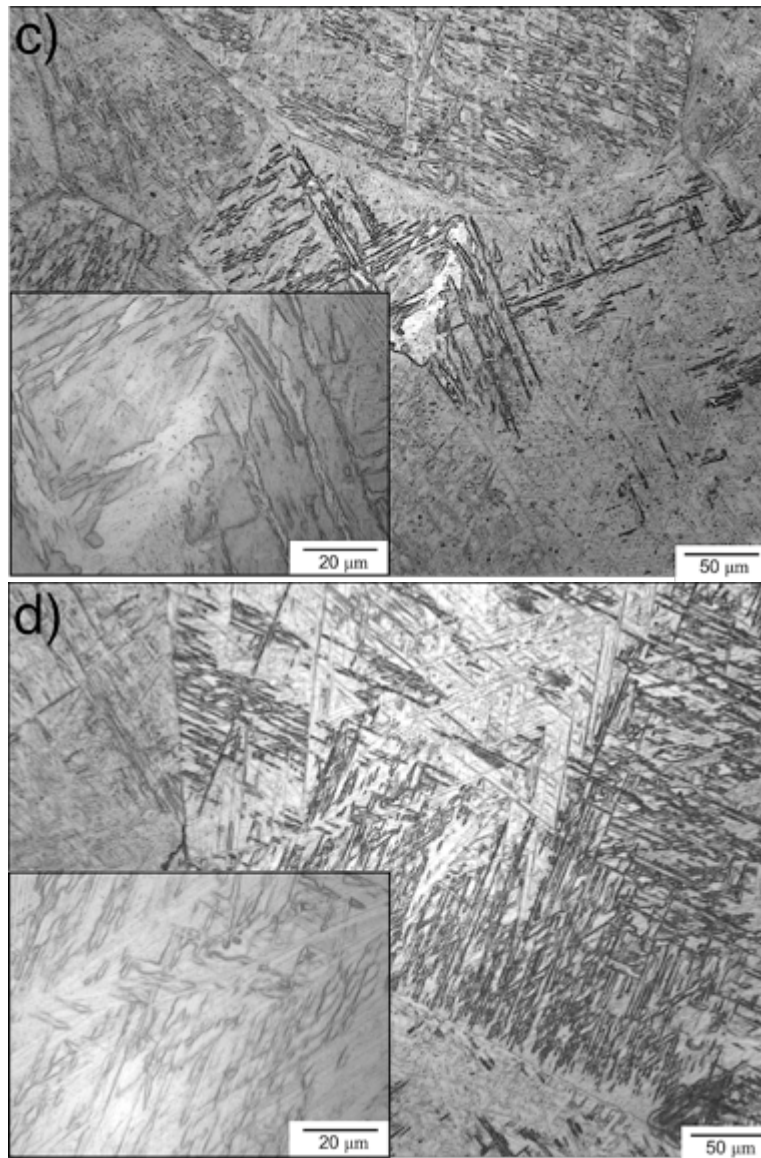


Figure 5.8. Back facing flow microstructures for starboard X-link section 1 (a), starboard X-link section 2 (b), arc-jet sample Class II (c), and arc-jet sample Class III (d).

5.3.2 Scanning Electron Microscopy

Oxide cracking, gas porosity, and shrinkage porosity were observed within the deposits. Several different oxide layers exist due to the dynamic nature of the event and the tendency of oxide layers to flake at higher temperatures. All samples contained small amounts of chemical contamination. Contamination of X-links samples 1 and 2 was consistent with MP35N fastener constituents and other constituents present in shuttle structural materials. Arc-jet samples 3 and 4 were contaminated by the SiC ceramic plate fixture used for testing. Solidification features observed were similar between

samples. Granular features coalescing to form a layer at the outermost surface were observed in X-link sample 2 and arc-jet sample 3 (Fig. 5.9). EDS scans of all samples were titanium and oxygen rich, with arc-jet scans for samples 3 and 4 containing trace amounts of nitrogen (Fig. 5.10). The ambient air content used in the arc-jet facility is similar to the air content in the mesosphere where breakup occurred. It is possible that detection limits of the instrumentation prevented small concentrations of nitrogen from resolution in the spectra. EDS also lacks the sensitivity necessary to accurately discriminate between titanium, vanadium, oxygen, and nitrogen energies. More sophisticated equipment will be utilized in further research to determine with certainty the elemental composition of the deposits.

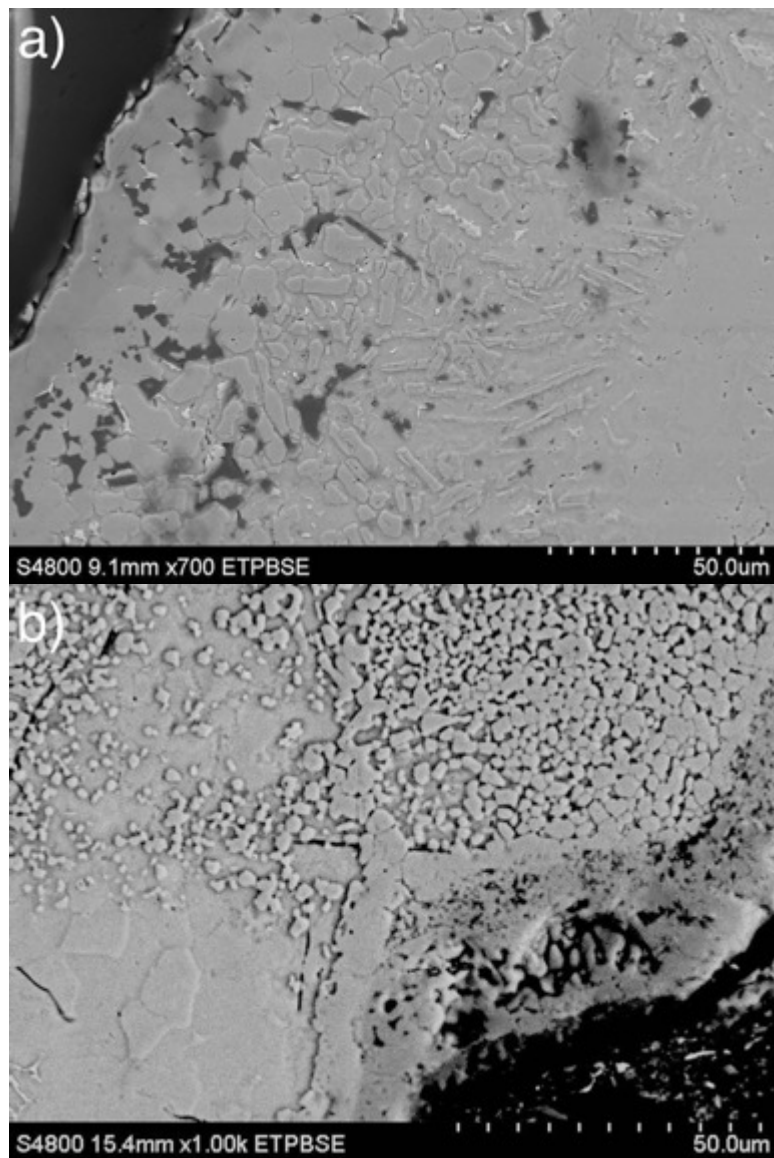


Figure 5.9. Backscattered electron images of granular features coalescing to form a solid layer in X-link sample 2 (a) and arc-jet sample 3 (b).

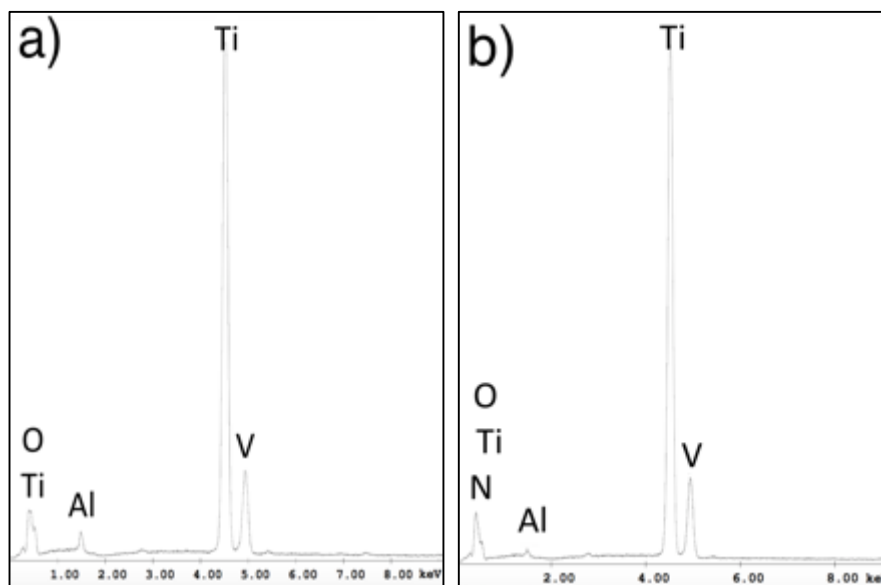


Figure 5.10. EDS spectrum of granular features in X-link sample 1 (a) and arc-jet sample 3 (b).

5.3.3 X-ray Diffraction

XRD was performed at the forward facing flow side for all samples. Fig. 5.11 shows XRD patterns, grouping the more thermally degraded X-link sample 2 and arc-jet sample 3 and the less thermally degraded X-link sample 1 and arc-jet sample 4. The most common titanium oxide form, TiO_2 (rutile), was not detected because this oxide typically forms between 300°C to 1000°C [23,25], indicating that these oxides formed at higher temperatures. High temperature oxides of the form Ti_xO and $\text{Ti}_x\text{O}_{2x-1}$ in addition to hexagonal α titanium were detected in all samples. The less degraded sample scans exhibit titanium nitrides, consistent with EDS scans, and Ti_2O_3 , a lower titanium oxide formed by reacting TiO_2 (rutile) with titanium metal at roughly 3000°F [26]. The more degraded sample scans show titanium rich Ti_2O . Oxygen deficient hexagonal oxides of the form Ti_xO , detected in all samples, are formed when oxygen orders in hexagonal α Ti; these oxides were likely detected at the metal/scale interface and were shielded from physical removal early in the deposition event. The oxide Ti_6O is a lower temperature oxide formed from the solid solution, and Ti_3O is a higher temperature oxide that crystallizes from the melt [27]. The higher oxide, Magneli-type phase Ti_4O_7 , found in all samples, forms when TiO_2 (rutile) is reduced [28]. The results indicate that more extreme degradation of samples formed oxygen deficient oxides and the less degraded samples formed nitrides and Ti_2O_3 . The non-uniformity in the color of the scales suggests different oxides in different areas of the samples.

Similar oxides were detected, but a more diverse set of oxide species were detected in the less thermally degraded samples. Lower stabilities of titanium nitrides versus titanium oxides resulting in reduction of the nitrides [30], physical processes to include ablation and dislodging of oxide layers, and instrumentation limitations may account for this finding. The scans suggest mixing of the oxides and the possibility of non-stoichiometric titanium oxides, as indicated by peak shifting and broadening. It is possible that several oxides and nitrides coexist, considering the similar atomic radii and tendency of titanium to combust in ambient pressure gaseous nitrogen in addition to oxygen. More sensitive methods are necessary to discriminate separate oxide and nitride species.

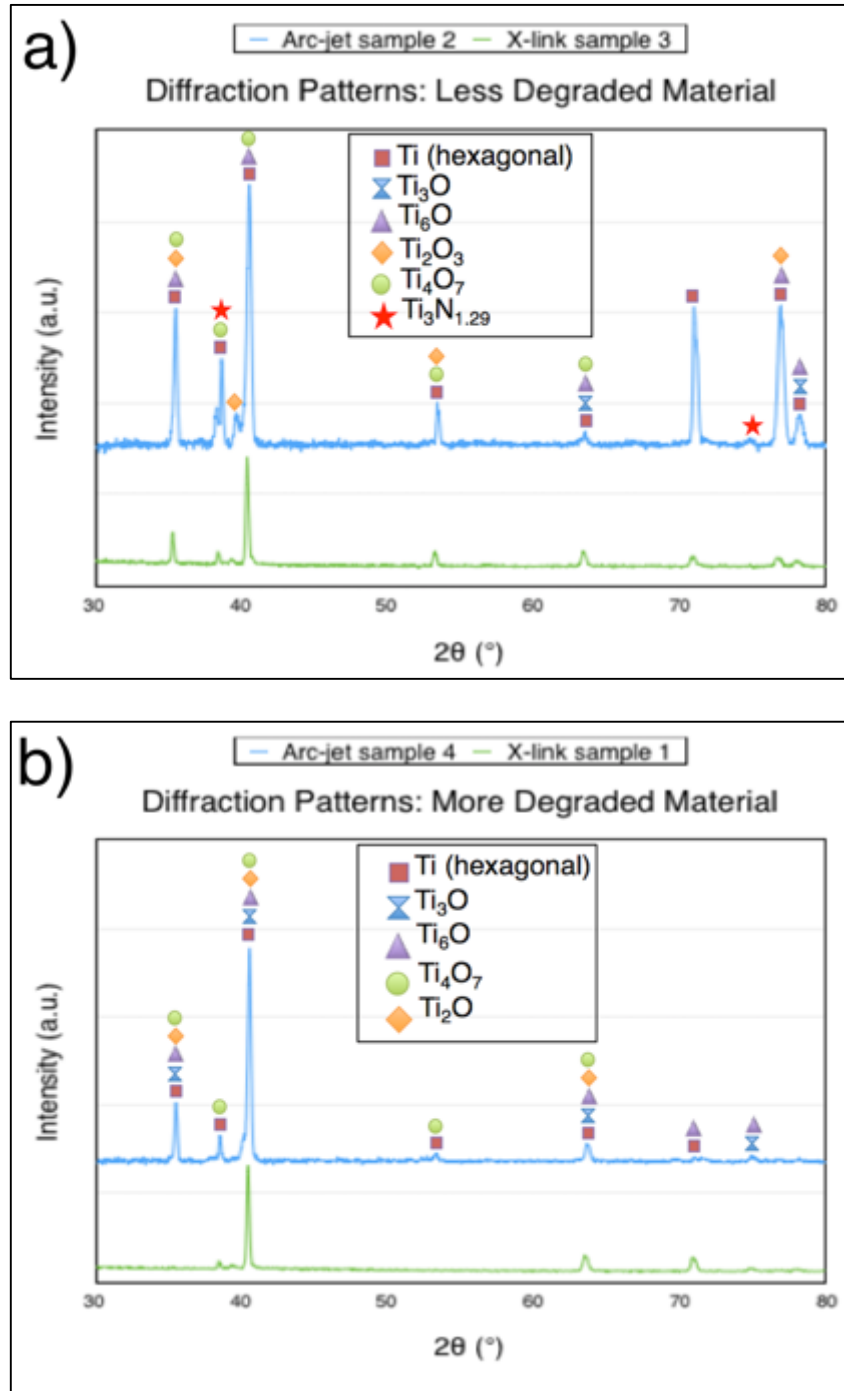


Figure 5.11. X-ray diffraction patterns for the less thermally degraded X-link sample 2 and arc-jet sample 3 (a) and the more thermally degraded X-link sample 1 and arc-jet sample 4 (b).

5.3.4 Microhardness Testing

Microhardness readings were taken traversing the sample from forward to back facing flow sides and averages lie within the typical range of commercial Ti-6Al-4V. Scatter in readings is due to the

intrinsic nature of the two phase Ti-6Al-4V structure. A spike in hardness is observed at the forward facing flow side due to the presence of an α case. Arc-jet sample 4 exhibited an α rich phase at forward and back facing flow surfaces. X-link samples 1 and 2 have relatively constant microhardness values after the initial α case despite the drastic transition in microstructural features. This may be explained by the acicular α present throughout the entire microstructure. Arc-jet sample 3 shows a slight increasing trend in hardness values as the grain size decreases from forward to back facing flow material while arc-jet sample 4 remains relatively constant, agreeing with the microstructures. It is noted that the bulk microhardness values of X-links samples 1 and 2 are lower than arc-jet samples 3 and 4, possibly due to the air quench or initial fine grained microstructure, resulting a harder material.

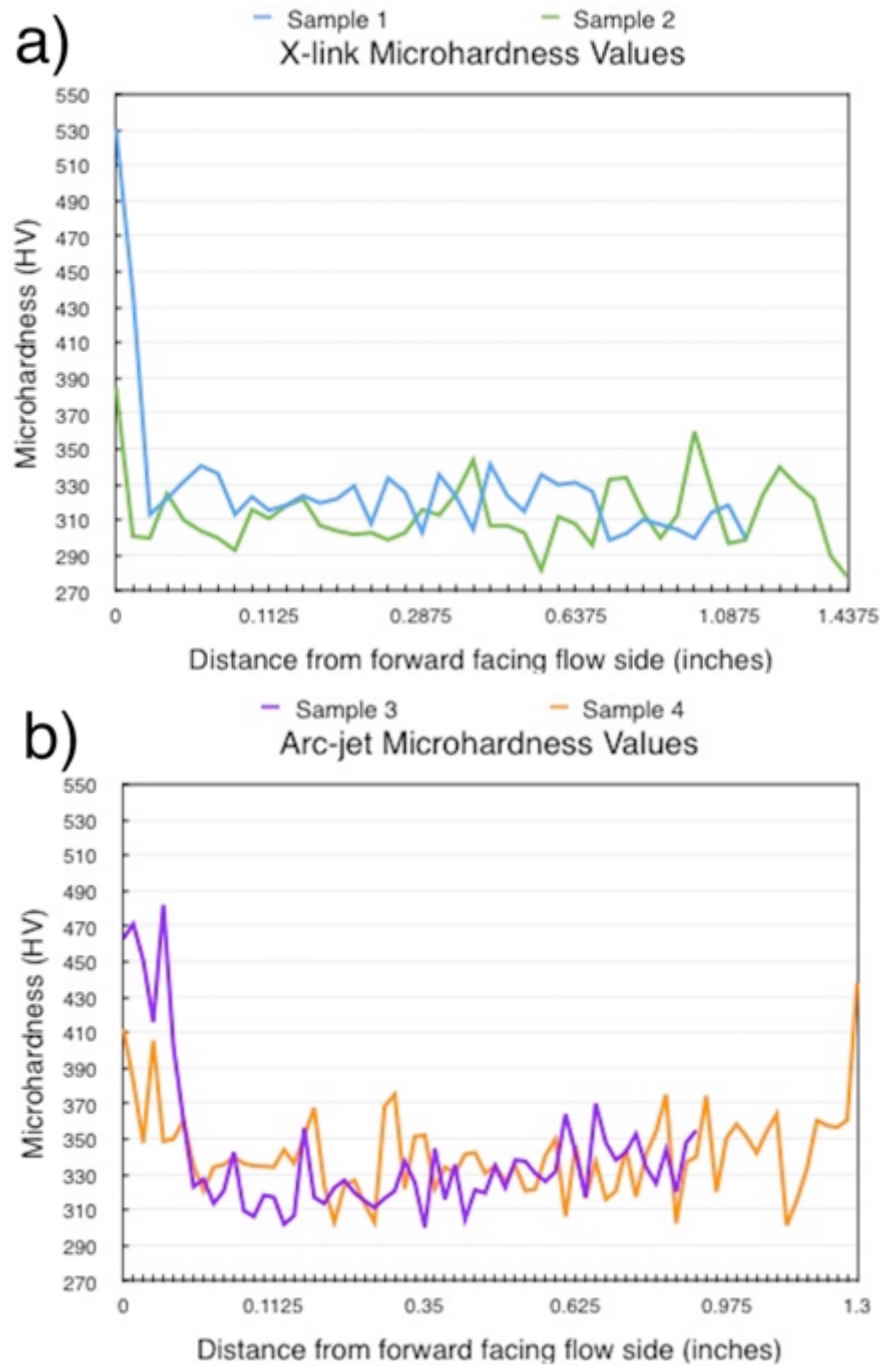


Figure 5.12. Microhardness values traversing from forward to back facing flow side for samples 1 and 2 (a) and samples 3 and 4 (b).

Table 5.2. Average microhardness and population standard deviation for samples 1-4.

	X-link Sample 1	X-link Sample 2	Arc-jet Sample 3	Arc-jet Sample 4
Average Microhardness (HV)	328	313	341	342
Pop. Standard Deviation (%)	40.1	19.4	40.4	24.3

5.4 CONCLUSIONS

The widely used aerospace titanium alloy, Ti-6Al-4V, was forensically characterized utilizing multiple techniques to better understand the material response in the monoatomic oxygen rich and high enthalpy re-entry environment. Material previously exposed to the actual and simulated re-entry environment were analyzed and compared by examining artifacts from the Space Shuttle *Columbia* and arc-jet tested samples, respectively. While the purpose of this work is to relate similarities, there are intrinsic differences affecting the results, including interaction with surrounding material systems, cooling rate, geometry, thickness, conductive heating effects, air content, length of combustion reaction, and possible encapsulation by surrounding materials. Similarities and differences were discussed relative to these factors.

The initial microstructural state of the X-links is suggested to be a sub β transus structure of elongated and equiaxed α in a lamellar α/β matrix, based upon observations of a physically unaffected portion of the port X-link. The initial microstructural state of the arc-jet samples was established to be slightly elongated α in a lamellar α/β matrix, similar except in grain size to the port X-link. Forward facing flow microstructural features are similar in all four samples, consisting of martensitic α within large prior β grains. The strongly microstructural similarities suggest conditions of the arc-jet are relatable to the environmental conditions of the X-links at the forward facing flow side. Back facing flow microstructural features differed between samples, yet similarities were distinguished between X-link samples 1 and 2 and arc-jet samples 3 and 4. The X-links exhibited a drastic microstructural transition to a basketweave structure of acicular alpha colonies and aged, transformed beta at the back

facing flow side that is likely due to conductive heating effects from a transition to thicker material. Arc-jet sample 3 had a less extreme transition to smaller grains at the back facing flow side. Microstructural gradients were only observed in material that physically appeared to have combusted, with the exception of sample 4, and uniform microstructures were observed in physically unaffected material. This implies that a combustion reaction may create a non-uniform heating condition and manifest through microstructural gradients, but it is possible for the combusted material to reach some steady state condition, as evidenced in sample 4.

SEM and XRD revealed qualities of the deposits, but these methods lacked the sensitivity to accurately discriminate between the oxide and nitride species present. XRD patterns suggest the more physically degraded material of X-links and arc-jet differed from the less physically degraded material, with a more diverse oxide species in the less thermally degraded material. Reduction of the nitrides, physical oxide removal processes, and instrumentation sensitivity may account for this observation. Microhardness testing revealed a higher average hardness in the arc-jet samples and a large degree of scatter due to the intrinsic nature of the material.

The similarities between features in samples 2 and 3 and samples 1 and 4 evidenced through XRD and SEM characterization indicate that different areas of the X-links exhibited different material reactions. It is possible that X-link sample 2 underwent only an ignition and melting event, and not a combustion event, as was documented through testing for arc-jet sample 3. X-link sample 1 appears to have ignited and combusted, like arc-jet sample 4. Recognition of these patterns will allow for information to be gleaned on the differing material evidence present in oxidation, ignition, and combustion events. Material with a higher effective ballistic number, i.e. regions with an out-of-plane protrusion (arrow in Fig. 5.1, shown in Fig. 5.3) on the X-links and Class III arc-jet specimens, result in uncontrolled combustion reactions limited by consumable material and removal from air stream. Lower effective ballistic numbers, i.e. planar material and Class II arc-jet specimens, appear to only ignite but not sustain combustion. Considering the complicated design of many structural components, the possibility of destructive material behavior resulting in the compromise of integrity of the space vehicle should not be ignored.

Several questions remain regarding the nature of the deposits and oxide/nitride species observed using the current techniques. A quantitative and more sensitive technique, Wavelength Dispersive Spectroscopy (WDS), will be used to further distinguish between the deposit oxide/nitride species. The more precise energy resolution achievable with WDS will allow for better differentiation between the titanium, vanadium, oxygen, and nitrogen energies and provide an improved understanding of the oxide species present using quantitative data. WDS will assist in understanding the complex deposit characteristics and reactions.

Given the extensive use of the Ti-6Al-4V alloy in past and future spacecraft, it is necessary to establish a known material reaction if exposed to the re-entry environment. Understanding the combustion response by defining thresholds and parameters necessary for a combustion reaction to occur will improve safety in future space travel. This and future work contributes to the sparse knowledge regarding bulk metal combustion and material reactions in the re-entry environment. Thermal degradation of titanium components can compromise the structural integrity of spacecraft; therefore, it is of interest to establish an expected combustion mechanism and graceful degradation pattern to ensure safety and reliability of future space travel.

5.5 ACKNOWLEDGEMENTS

The authors would like to acknowledge the Herrera, Stafford, and Associates employees for assistance with laboratory services. The authors would also like to thank Mike Ciannilli of the *Columbia* Research and Preservation Office at NASA-KSC for facilitating access to *Columbia* artifacts and Rick Russell of the Spacecraft and Launch Vehicle M&P Engineering group at NASA-KSC for his support.

Chapter 6: Results and Discussion

Table 6.1 outlines location within this work where results of each respective sample is discussed, noting differing nomenclature per each chapter. N/A is written where testing for that sample was not completed.

Table 6.1. Locations of data discussion of X-link and arc-jet samples in dissertation.

NOMENCLATURE	LOM	SEM/EDS	XRD	MICRO-HARDNESS
X-LINK SECTION D.2				6.1.4
CH. 4-REGION A	4.3.1	4.3.1		
CH. 5-SAMPLE 1	5.3.1	5.3.2	5.3.3	5.3.4
X-LINK SECTION D.6				
CH. 5-SAMPLE 2	5.3.1	5.3.2	5.3.3	5.3.4
X-LINK SECTION E.2			6.1.3	6.1.4
CH. 4-REGION B	4.3.2	4.3.2		
X-LINK SECTION E.3	6.1.1	6.1.2	6.1.3	N/A
X-LINK SECTION G.1	6.1.1	6.1.2	6.1.3	6.1.4
ARC-JET SPECIMEN 8			6.2.3	N/A
CH. 5-SAMPLE 3	5.3.1	5.3.2	5.3.3	
ARC-JET SPECIMEN 16	6.2.1	6.2.2	6.2.3	5.3.4
ARC-JET SPECIMEN 17		6.3.2	6.2.3	N/A
CH. 5-SAMPLE 4	5.3.1	5.3.2	5.3.3	
ARC-JET SPECIMEN 28	6.2.1	6.2.2	6.2.3	5.3.4

6.1 X-LINK RESULTS

Section D has been covered in entirety through the published works in Chapters 4 and 5. One secondary section of section E was discussed in an introductory manner in Chapter 4, but will be elaborated on in this chapter. Section E was cut from the top, webbed portion of the X-links in an area of

apparent aft-to-forward flow (Figure 6.1). Two sections were chosen for analysis from piece E: section E.2 and E.3. Arrows indicate observation orientation for the metallographic specimens. Surface features of section E and microscopy of section E.2 are detailed in Chapter 4.3.2. This section supplements previously presented data for section E.2 and will present new data for section E.3. Microhardness testing was only performed on section E.2, which exhibited a microstructural gradient.

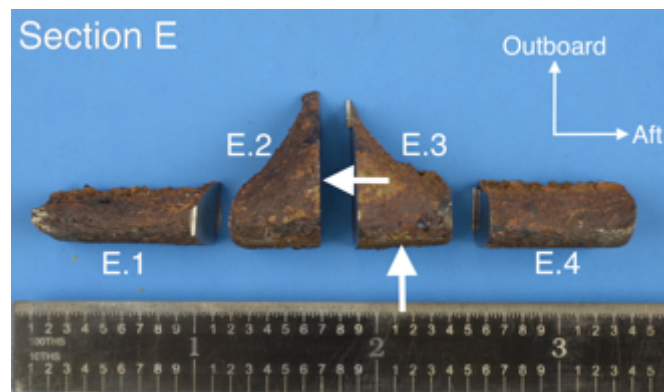


Figure 6.1. Secondary sectioning of section E.

Section G was not previously discussed, therefore surface features, LOM, SEM/EDS, XRD, and microhardness testing results will be covered here. Section G was cut from the inboard side of the X-link, in an area of apparent forward-to-aft flow (Figure 6.2). For reference, the forward-to-aft flow appeared to be most aggressive, noted by the burn through in the flange, but section G was furthest from this considerable mass loss. The section chosen for analysis was section G.1; section G.1 was mounted without prior removal of the MP35N fastener, so that the fastener was also mounted in cross-section. The MP35N fastener material was not analyzed. The arrow in Figure 6.2 indicates observation orientation of the metallographic specimen.

On the surface of section G, an orange deposit was observed and was confirmed through SEM and EDS to be tubular, porous, carbon-rich matter. It is probable that this region of the X-link impacted a tree or bush upon descent, embedding wood on the surface of the hot titanium. This finding did not play an active role in the combustion of titanium, and is considered to be of little importance. Other surface features were similar to those of other sections, with a globular, cracked, and flaky appearance.

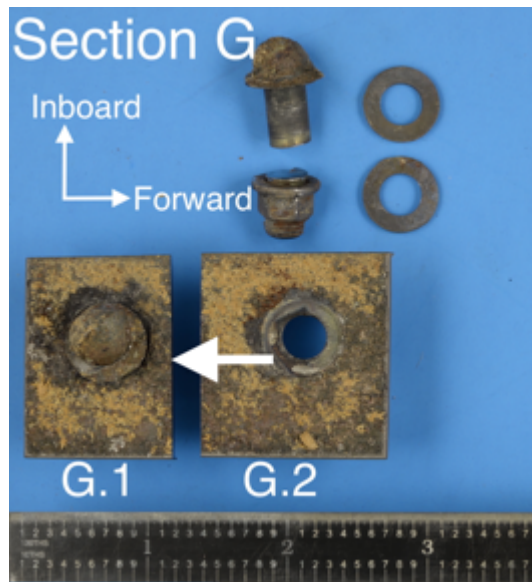


Figure 6.2. Secondary sectioning of section G.

6.1.1 Microstructural Features

It is of interest to know the initial microstructural state of the X-link components, so as to understand the microstructural evolution caused by the combustion reaction. For a detailed discussion, please see section 5.3.1.

Section E.3

Microstructural features were uniform throughout the sample, consisting of martensitic α' and some serrated α , within large prior β grains (Figure 6.3). Section E.3 did not exhibit a microstructural gradient as the other samples did, and this is likely due to the observation orientation. The surface observed in cross-section is on the inboard side of the X-link, meaning that the entire surface was exposed to an aggravated flow, unlike the other samples in which orientation created an inboard and outboard side. While this does not suggest uniform heating or laminar flow for the entire X-link, or even the inboard side, it is possible that this small sample of material was exposed to even heating conditions, due to the orientation. Grain size for section E.3 was slightly smaller than grain size for the inboard sides of section D, and similar in size to those in section E.2.

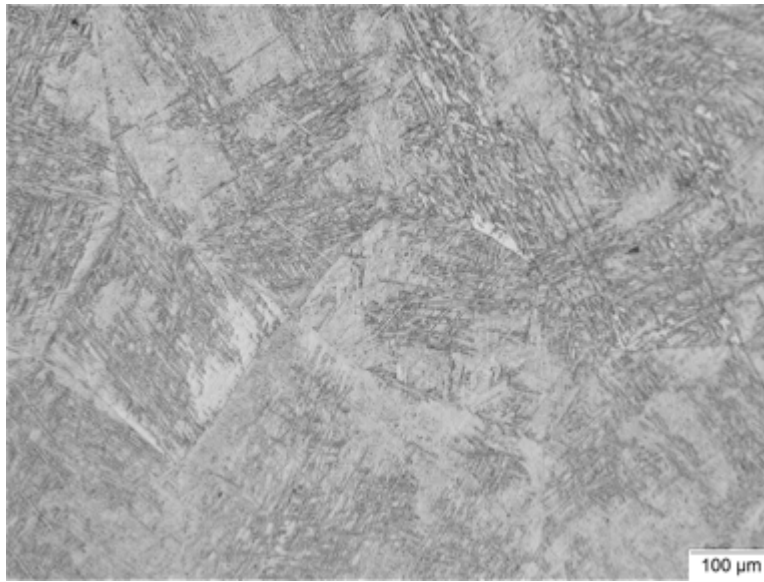


Figure 6.3. Microstructure of section E.3, showing martensitic α within large prior β grains.

Section G.1

In contrast to the martensitic α' observed at the inboard sides of sections D and E, the inboard side of section G consisted of an outlined serrated α , with transformed β and acicular α (Figure 6.4a). The outboard microstructure contained diffuse β forming between acicular α colonies with some α islands (Figure 6.4b), similar to sections D and E. The inboard side microstructure suggests a temperature above the β -transus, while the outboard side suggests lower temperature exposure than the inboard side. The temperature reached on the outboard side is likely slightly above the β -transus.

This diffuse β structure was observed at the outboard sides in sections D and E, and appears to be a transitory structure formed at lower temperatures than the acicular and serrated α , typically forming above the β -transus, but higher temperatures than the globular α , forming below the β -transus. The presence of α islands, previously assumed to be primary α in Chapter 4, is now theorized to be a transitory serrated α structure. This deduction was made considering the shape, location, and surrounding microstructural features. The α islands are often faceted and irregular in nature, and the surrounding features suggest a higher temperature exposure, given the presence of acicular α . The islands may indeed be primary α structures, but given the morphology of the islands, it is a less likely conclusion. Further analysis through electron backscatter diffraction and transmission electron microscopy could provide clarification.

Section G.1 was mounted in cross-section without prior removal of the MP35N fastener piece. The fastener acted as a roughly ½ inch thick interruption in the bulk titanium, essentially separating inboard from outboard sides. At the fastener interfaces, a globular, elongated primary α in a transformed β matrix containing acicular α was observed (Figure 6.5), suggesting that the material nearest the fastener interfaces experienced a different thermal history than the rest of the sample. It is also possible that manufacturing could have influenced a unique microstructural state near the fastener holes due to residual cold working. The same globular primary α structure, assigned as the initial microstructural state, was observed on the inboard/fastener and outboard/fastener interfaces. The Ti-6Al-4V/MP35N interfaces and outboard microstructures of section G suggest that the temperature in these areas did not exceed the β -transus temperature. Section G exhibited the least thermal degradation compared to sections D and E, which may attribute to the contrasting microstructural features observed.

This difference in microstructure at the MP35N/Ti-6Al-4V interface could also be explained by the specific heat capacities of the two materials. MP35N has a specific heat capacity of 758 J/kg-K, and Ti-6Al-4V has a specific heat capacity of 528 J/kg-K. Heat capacity refers to the ability of a material to absorb heat without a temperature increase. Since MP35N has a higher heat capacity, it would take more heat to cause a temperature increase, therefore MP35N was at a lower temperature than Ti-6Al-4V. In essence, the MP35N fasteners could have acted as a heat sink to the titanium, causing the Ti-6Al-4V in contact with the MP35N fastener to be at a lower temperature than the bulk of the sample, generating a localized temperature differential and thus microstructural difference. It is also possible that the fastener and washer material were shielding the underlying titanium, which would account for the difference in microstructure at the titanium surfaces in contact with fastener material.

Section G is nearer to the forward side of the X-link, further away from the most extreme physical degradation evident at the flange and aft-most fastener. The larger distance from more aggravated flow appears to have produced different microstructural features. In sections D and E, the microstructure tends to transition from martensitic α at the inboard side, to serrated α between inboard and outboard sides, to the acicular alpha and diffuse beta structures at the outboard side. The serrated α at the inboard side of section G.1 thus appears to be a lower temperature structure than the martensitic α

structure, while the fastener interfaces bear a close resemblance to the initial microstructural state of the X-links. The diffuse beta at the outboard side still exists, with an increase in percentage of alpha islands compared to the other X-link samples.

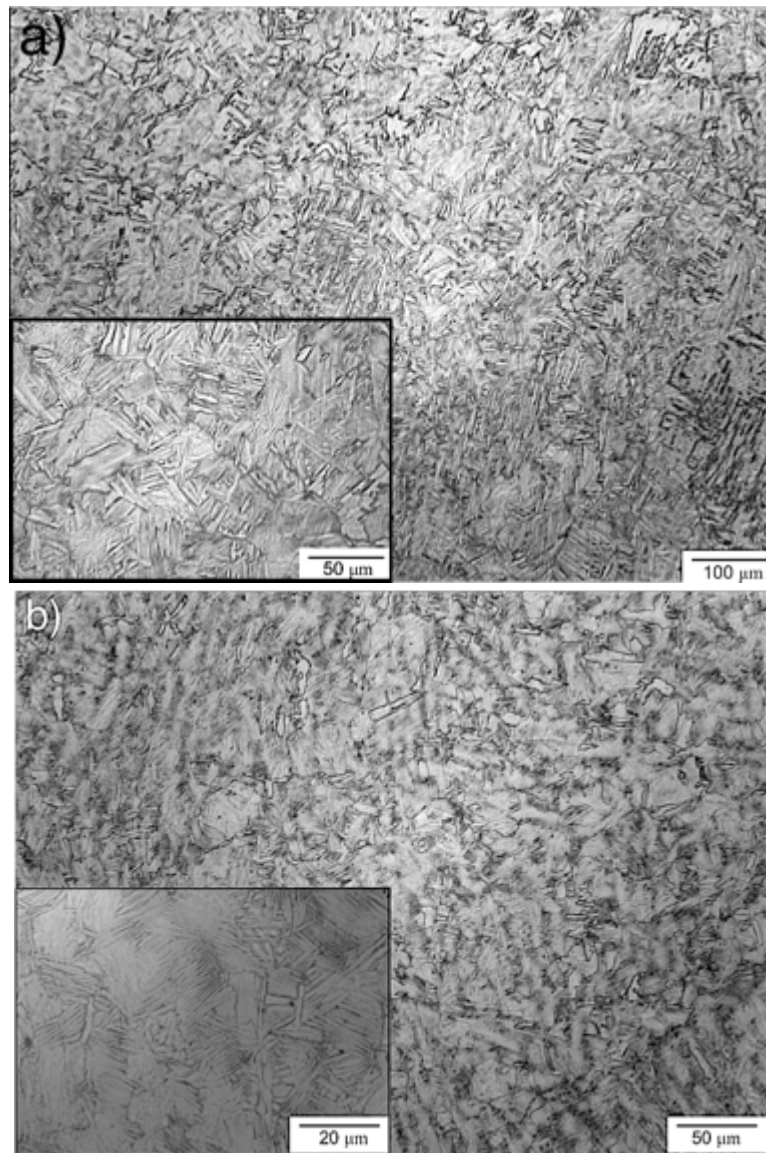


Figure 6.4. Microstructural features of section G.1 at the inboard (a) and outboard (b) sides.

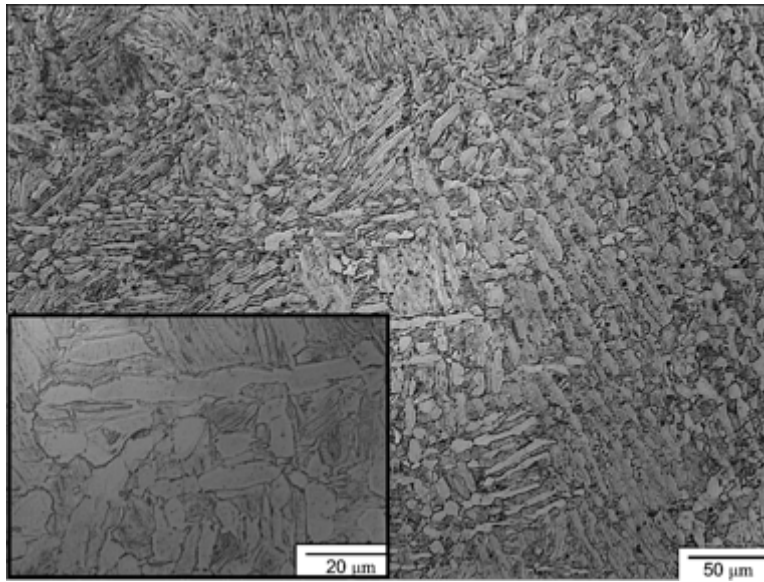


Figure 6.5. Microstructure of the Ti-6Al-4V material at the titanium/MP35N fastener interface.

6.1.2 Scanning Electron Microscopy/Energy Dispersive Spectroscopy

It is noted that in all samples, X-link and arc-jet alike, bulk metal oxidation and deposition were occurring simultaneously. For ease of explanation, the once molten, now solidified metal oxides on top of the base metal will be referred to in a general matter as layers. This term does not discriminate between bulk metal oxidation and deposits. The deposits can be of the parent Ti-6Al-4V material, foreign material from other surrounding material systems, or a mixture of the two. In those samples where EDS spectra consisted primarily of titanium and oxygen with no foreign contaminant, it is assumed that bulk metal combustion dominated.

It is noted that the layers present on these samples may have originated from several sources, to include flying through a molten debris cloud, localized thermal erosion resulting in dislodging and transport of material, expelling of molten metal from the surface, or physical removal processes. Several samples contained spherical deposits (discussed in Chapter 4.3.1) that very likely could have originated from spalling of the protective oxide layer and expelling of molten metal. Literature reviewed in Chapter 2 suggested that molten particles maintain their spherical shape upon ejection. All layers contained titanium, and the surrounding material systems appeared to be mixing with the molten and oxidized titanium.

Section E.3

Layers were minimal on section E.3, due to the nature and location of the section. Chemically, the layers consisted primarily of titanium and oxygen. Embedded particles, rich in silicon and oxygen, and similar to those discussed in Chapter 4.3.2 for section E.2, were observed (Figure 6.6). These likely originated from thermal protection system or glassy material that interacted with and likely impacted this part of the X-link during re-entry.

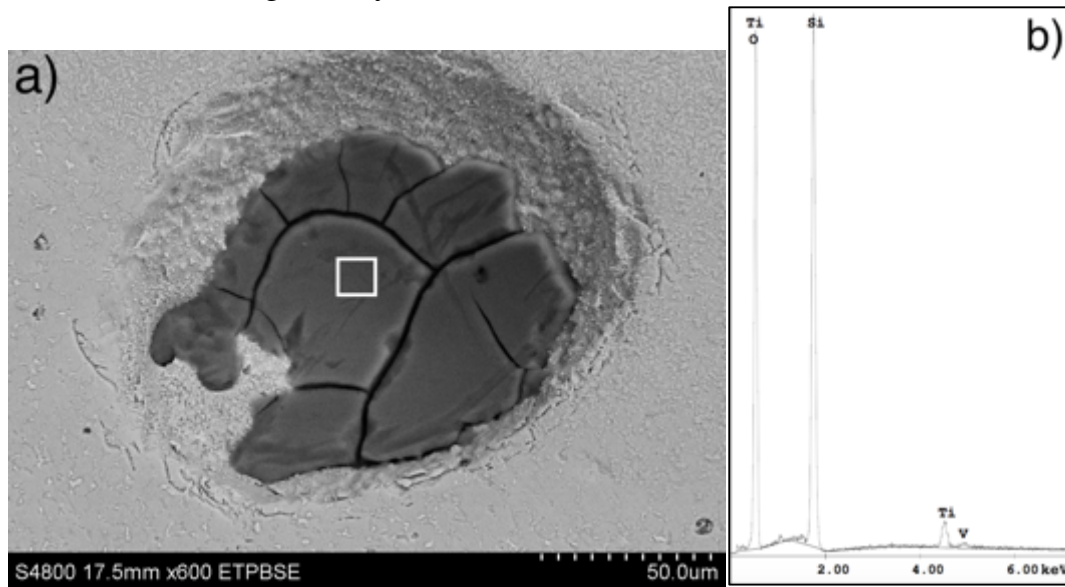


Figure 6.6. Backscattered electron image of silicon rich embedded particle in section E.3 (a) and EDS spectrum of boxed area (b).

Section G.1

Section G.1 displayed a lack of thermal erosion relative to other X-link sections discussed. Due to the close proximity of the MP35N fastener to the titanium material, nickel, cobalt, chromium, and molybdenum were observed within the deposits. Layers appear to have resulted from mixing of molten and oxidized titanium with MP35N fastener material, though other material systems were resolved. For the other sections, bulk metal combustion seemed to dominate, i.e. the layers consist primarily of oxidized Ti-6Al-4V; in contrast, section G.1 appears to be deposit dominant. The top surface (fastener head side) has more deposits than the bottom surface (fastener shaft side).

The layers were quite porous (Figure 6.7a), and granular features (similar to those in Chapter 5.3.2 for X-link sections D and E) were observed on the layers closest to the free surface (Figure 6.7b).

Foreign elements, to include fastener material, structural steel, and carbon-rich material, were observed in all layers on section G.1, but were most prolific in the porous layers. There was no correlation between amount of foreign elements and distance from the free surface. Layers and scales in section G.1 appeared lighter than other X-link and arc-jet samples in backscatter mode due to the increased presence of heavier elements such as cobalt, chromium, and nickel.

Trace amounts of nitrogen (<0.15 wt.%) were found in section G.1 deposits (Figure 6.8b). For reference, section G was furthest from the aggravated flow condition, and had negligible mass loss. It is possible that the nitrogen, while volatilized in those samples with more degradation, was retained in this section.

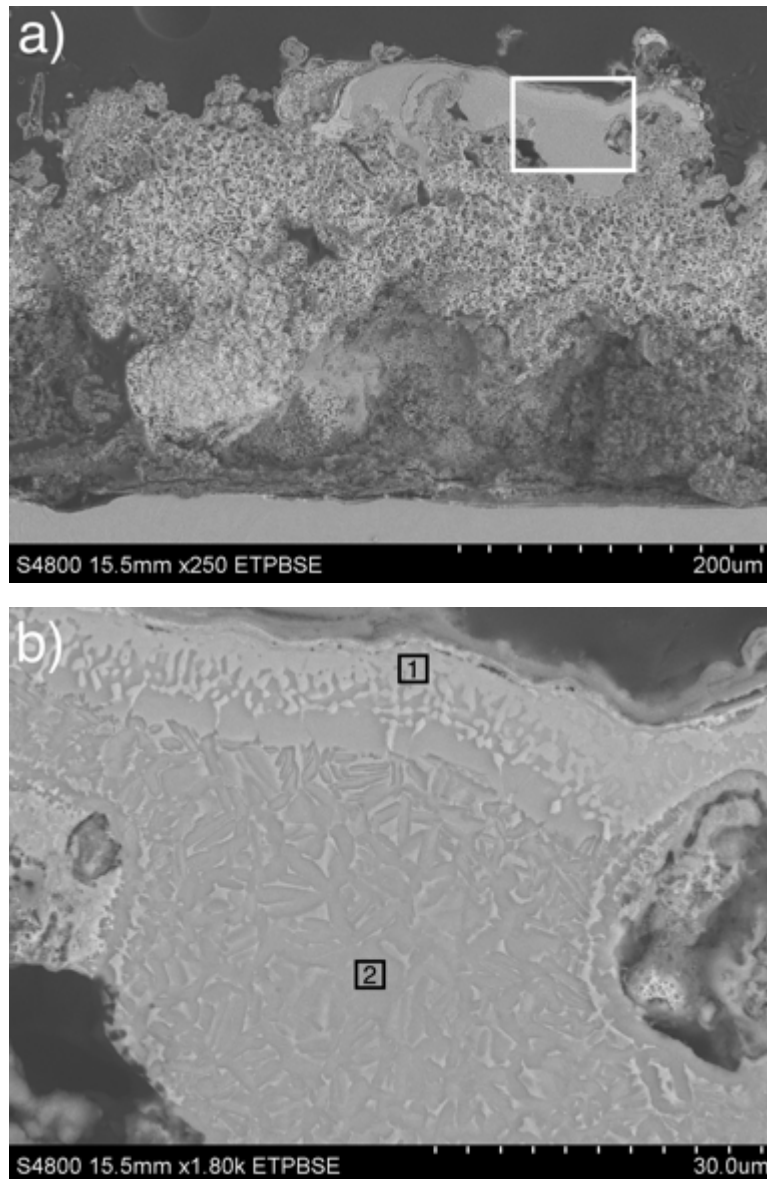


Figure 6.7. Backscattered electron image of section G.1 inboard side deposit (a), with white boxed area indicating location of zoomed image in (b). Black boxes indicate locations of EDS scans.

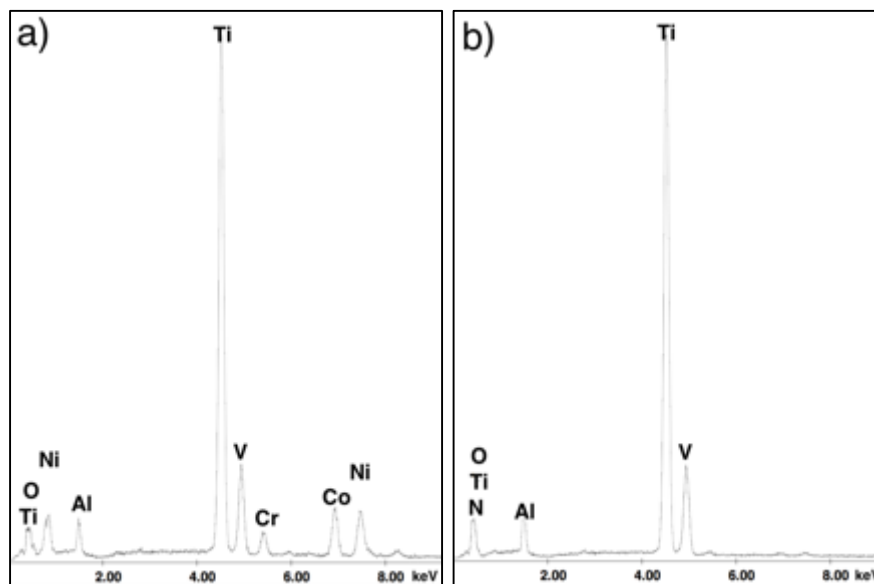


Figure 6.8. EDS spectra of section G.1 for box 1, porous material in Figure 6.7a (a) and box 2, granular features in Figure 6.7b (b).

6.1.3 X-ray Diffraction

Section E.2

Section E diffraction patterns, shown in Figure 6.9, illustrated that specific oxide compound presence was based on orientation within the shuttle. Boxed area 1 refers to the top surface, boxed area 2 refers to the inboard surface, and boxed area 3 refers to the side closest to the bottom surface. The top orientation refers to the top view of the X-link within the shuttle, if the reader were on top of the shuttle looking down. The oxides took the form Ti_xO_{2x-1} and Ti_xO . Hexagonal titanium was observed at all surfaces and corresponded to the α case created by the high temperature diffusion of oxygen into the surface. Titanium rich oxides of the form Ti_xO typically form near the surface as oxygen diffuses into the titanium. Magneli-type phases were observed with Ti_4O_7 and Ti_7O_{13} ; these tend to form when TiO_2 (rutile) is reduced [28]. Location 1 (top) exhibited the most diverse oxide species, similar to what was observed for Class II behavior in Chapter 5.3.3. Location 2 (inboard) has a less diverse oxide species than locations 1 (top) and 3 (bottom), consistent with the findings in Chapter 5.3.3, indicating that more physically degraded material tends to show fewer oxide species, likely due to the volatilization of intermediate oxides. No rutile was detected. It is likely that due to the lower temperature properties and ease of volatilization versus higher titanium oxides, that the any rutile phase previously present was

consumed in the creation of higher temperature oxides. Small peak shifting and broadening is observed and may be explained by residual stresses in the material, instrumentation error, and mixing of oxides causing the formation of non-stoichiometric oxides.

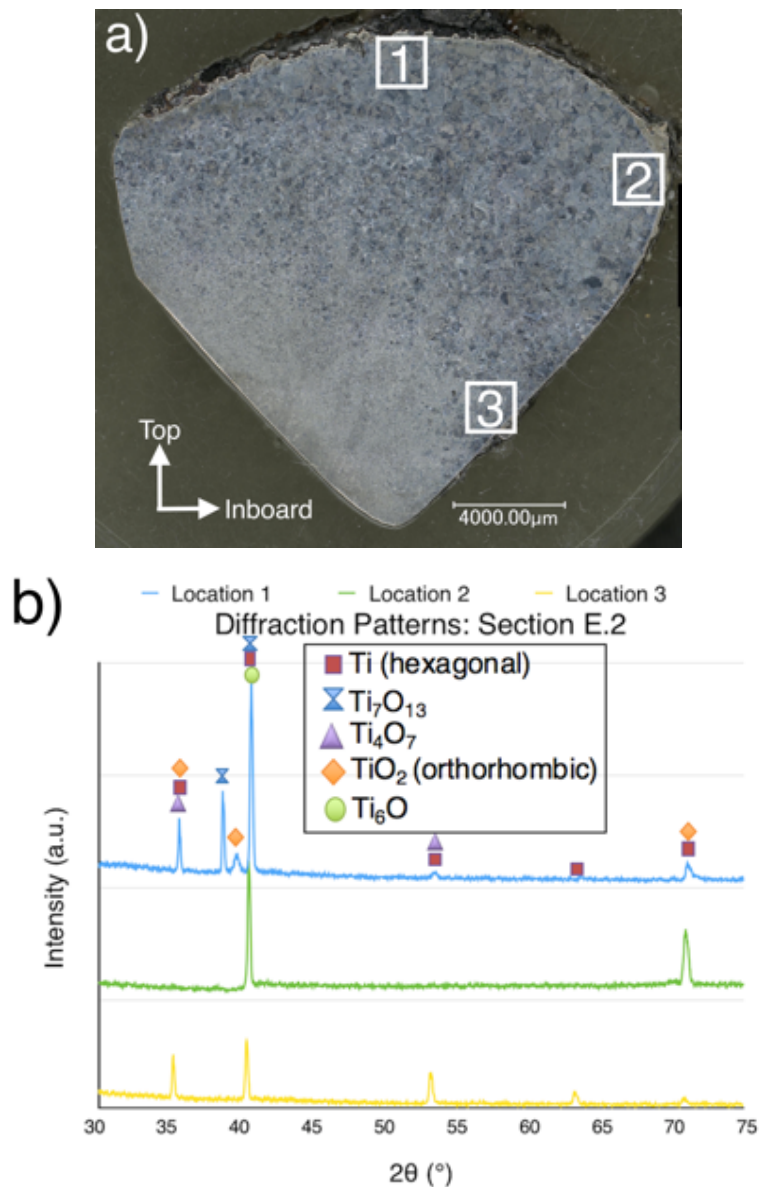


Figure 6.9. Location of XRD data collection (a) and diffraction patterns for section E.2 (b).

Section E.3

Section E.3 evidenced a more diverse oxide species, also consistent with Chapter 5.3.3 findings that less degraded material possessed intermediate oxides and more degraded material did not. Similar to the other samples, hexagonal titanium, titanium rich oxides formed at the surface, and Magneli-type phases were observed. The less titanium rich Ti_2O was also noted. No rutile was detected. Diffraction patterns were taken at the top side, where deposits were most plentiful.

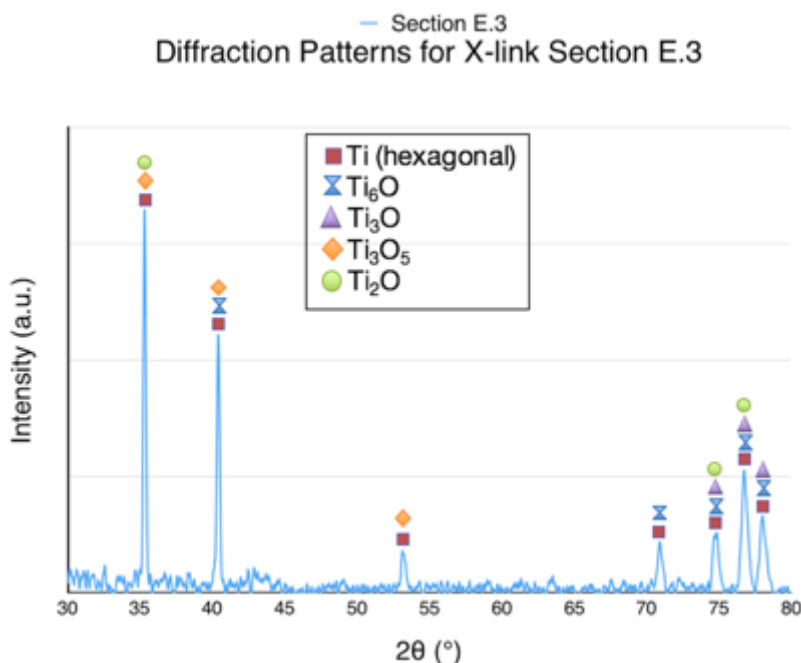


Figure 6.10. Diffraction pattern for section E.3.

Section G.1

Slight differences were observed in the diffraction patterns between the inboard and outboard side of section G.1. The oxides found in section G.1 have been discussed previously and consist primarily of hexagonal titanium, titanium rich oxides, Magneli-type phases, and orthorhombic TiO_2 . Orthorhombic TiO_2 is typically associated with brookite, but the methods available were not sufficient to confirm the presence of brookite [103]. When examining the diffraction patterns individually, it was determined that hexagonal titanium, Ti_2O_3 , and Ti_3O were more prominent at the outboard side, while Ti_4O_7 , TiO_2 (orthorhombic), and Ti_6O were more prominent at the inboard side. In summary, higher order Magneli phases and more titanium rich oxides were observed at the inboard side. Orthorhombic

titanium was also observed at the more degraded top side of section E.2. Oxide mixing and non-stoichiometry caused some peak shifting.

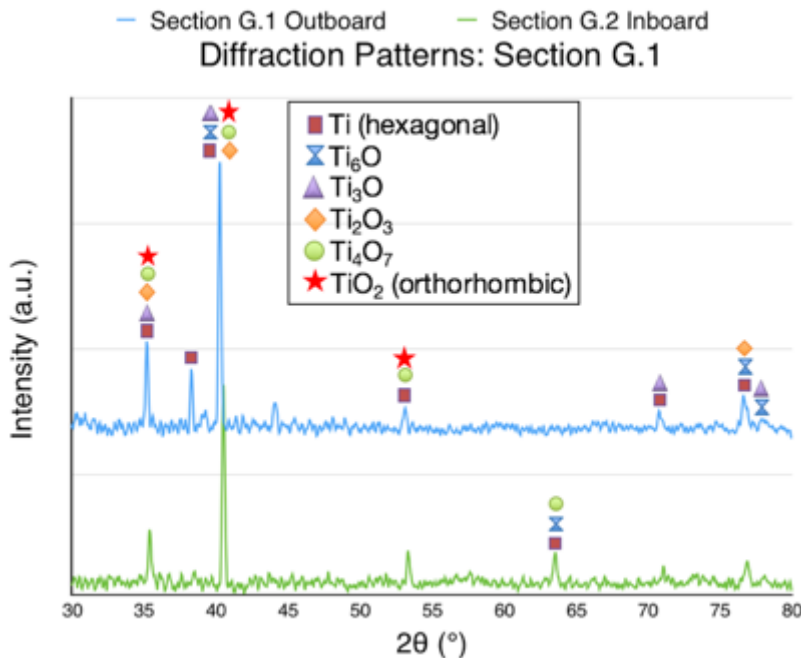


Figure 6.11. Diffraction patterns for the inboard (bottom) and outboard (top) side of section G.1.

6.1.4 Microhardness Testing

For comparative purposes, microhardness readings from section D.2, E.2, and G.1 are shown in Figure 6.12. Average microhardness values and population standard deviation are shown in Table 6.2. Standard deviation is high due to the intrinsic nature of the two phase alloy. Deposits had the highest microhardness, ranging from 600-800 HV, exhibiting a higher hardness than the α cases. In terms of physical degradation level, progressing from highest to lowest, are sections D.2, E.2, and G.1.

The microhardness values were highest at the inboard side for sections D.2 and E.2, where an α case caused a sharp increase. A relatively constant microhardness value was observed through the bulk of section D.2, despite the drastic microstructural change from acicular α within large prior β grains to the diffuse β structure. Section E.2 exhibited a steady decrease in microhardness traversing from inboard to outboard side, and exhibited a higher average microhardness than sections D.2 and G.1; this may be due to the smaller grain structure. In addition, section E.2 had the lowest outboard hardness of the three sections shown, and is similar to the values obtained for the outboard side of section G.1.

The microhardness values for section G.1 are plotted as a whole, eliminating the intermediate fastener material length, with the inboard portion of material representing 0 through 0.375-inches and the outboard portion representing 0.375-inches and beyond. Section G.1 did not develop a significant α case due to the further proximity from most extreme physical degradation. Similarly, the average microhardness and standard deviation were also lowest in this section; this is postulated to owe to the lower temperature microstructural features observed and relative lack of acicular features. The outboard hardness values were similar between sections D.2 and G.1, but section E.2 had a lower microhardness at the outboard side.

For completeness, the features of section D.6 will be reiterated here from Chapter 5.3.4. Section D.6 had a low α case hardness, and the microhardness remained relatively constant throughout the length of the sample. At the outboard side, hardness reached a low, corresponding to the basketweave structure with some acicular features which bore strong similarities to the initial microstructure of the X-links. The average microhardness was 313 HV, coming in higher only than section G.1.

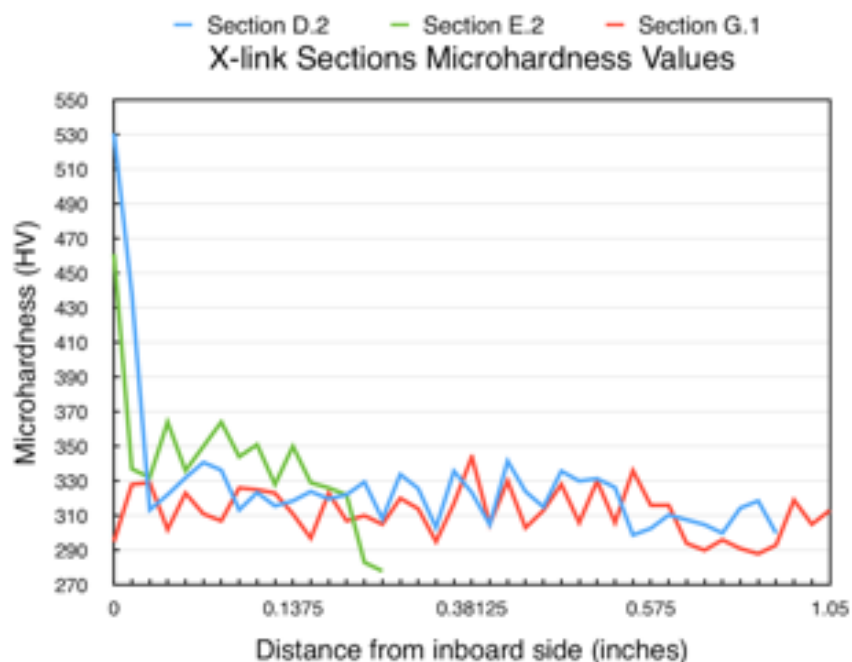


Figure 6.12. Traversing microhardness testing results for sections D.2, E.2, and G.1.

Table 6.2. Averages microhardness values and population standard deviation for sections D.2, E.2, and G.1.

	Section D.2	Section E.2	Section G.1
Average Microhardness (HV)	328	341	305
Population Standard Deviation (%)	40.1	38.8	13.7

6.2 ARC-JET RESULTS

Four arc-jet samples were chosen for analysis: two exhibiting Class II behavior, and two exhibiting Class III behavior. Table 6.1 details the chosen samples. Full details of these tests can be found in reference [6] and Table 3.1, with as-received photography in Figure 3.3. Surface examination by EDS was limited due to the contamination by foreign elements to include silicon, carbon, fluorine, and sodium. The silicon and carbon likely stem from the ceramic the Ti-6Al-4V plates were attached to during testing. The remaining contaminants were thought to have originated from previous handling and cutting of the specimens. The presence of these contaminants caused charging and difficulty with data analysis, therefore minimal surface SEM/EDS data was utilized during analysis. Specimens 8 and 17, with the exception of SEM/EDS data, are covered in Chapter 8. Specimen 16 and 28 will be discussed in this chapter. The microhardness testing presented in section 7.3.4 represented specimens 16 and 28. No further microhardness testing was performed.

6.2.1 Microstructural Features

Specimen 16

Specimen 16 exhibited a microstructure of acicular α' within large prior β grains. Grain size change from leading edge to trailing edge were negligible, and the structure remained consistent throughout. This structure suggests exposure above the β -transus followed by a quick cooling event. It is recognized that the arc-jet samples underwent an air quench upon removal from the flow stream. Essentially, once it was deemed that the test had reached completion, the samples were removed from the supersonic flow using a swing arm, the supersonic flow was halted, and the metal was cooled in air to ambient conditions.

Converse to the X-link microstructural features, the arc-jet samples are shown with the leading edge structure at 100X, and the trailing edge structure at 100X with a 200X inlay, to accurately represent the features of the structure.

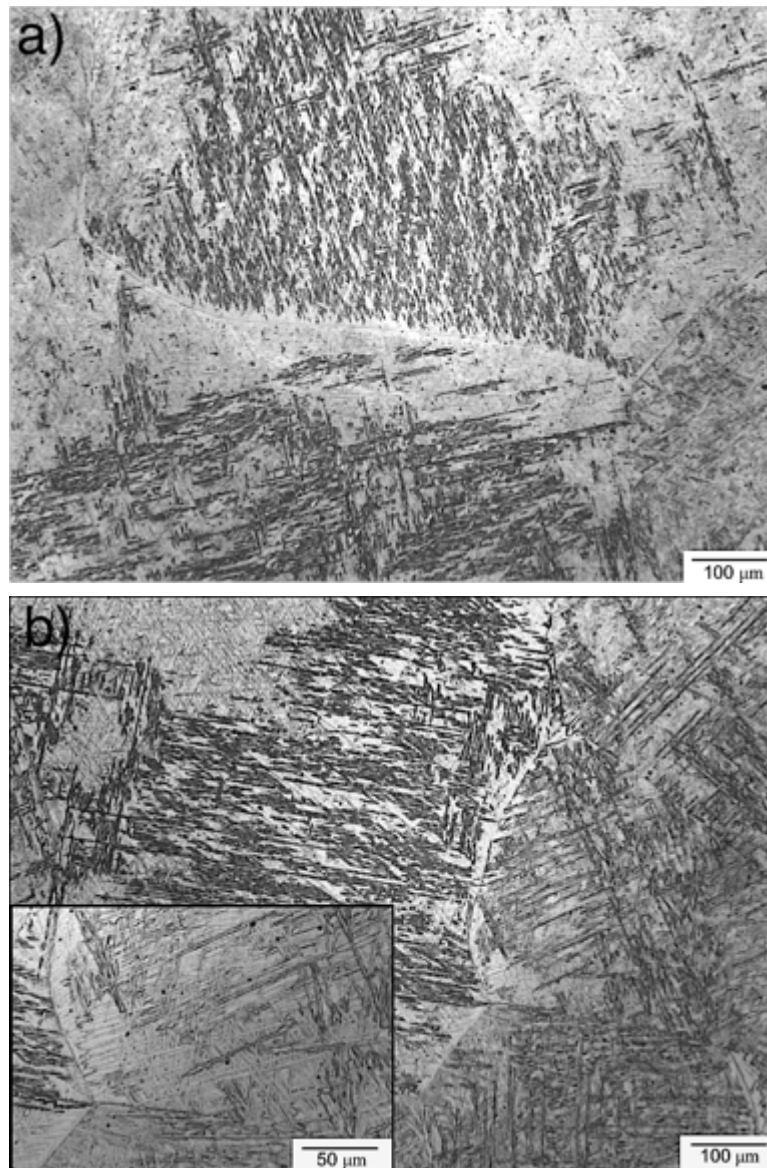


Figure 6.13. Microstructural features of the leading edge (a) and trailing edge (b) of Class II arc-jet specimen 16.

Specimen 28

The microstructural constituents throughout specimen 28 were uniform and consisted of martensitic α' within large prior β grains. Grain size change from leading edge to trailing edge is negligible. These observations are consistent with the known quasi-stable environment of the arc-jet.

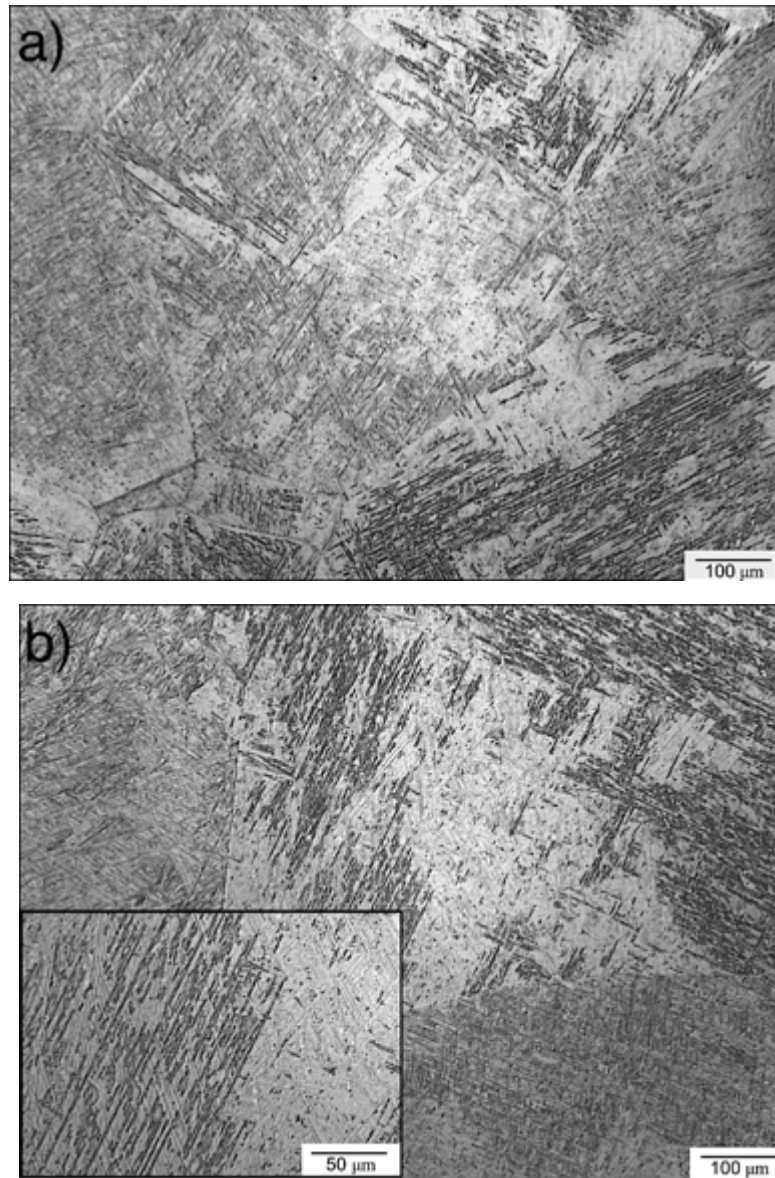


Figure 6.14. Microstructural features of the leading edge (a) and trailing edge (b) of Class III arc-jet specimen 28.

6.2.2 Scanning Electron Microscopy/Energy Dispersive X-ray Spectroscopy

Specimen 16

Layers on specimen 16 consisted primarily of granular features that coalesced nearest the surface to form a boundary (Figure 6.15). EDS revealed (Figure 6.16) that these features were titanium and oxygen rich, with trace amounts of nitrogen. Aluminum, titanium, and oxygen rich intergranular deposits, porous in nature, were also observed. It appears that the higher concentration of aluminum leads to the formation of this intergranular phase. The matrix material was identified as Ti-6Al-4V and oxygen rich, similar to the granular features and deposit nature of the X-links. Converse to the X-link samples, which were surrounded by several material systems, the arc-jet samples have layers formed by bulk metal oxidation. In some cases, the protective oxide layer spalled, metal was ejected from the surface, and some of the ejected particles re-deposited.

For the arc-jet samples, minimal foreign element contamination was observed. Foreign elements that were present were silicon and carbon, originating from high temperature mixing of the SiC fixture and Ti-6Al-4V plate material. For some samples, sodium and fluorine were also detected with EDS scans. These were detected on the surfaces, despite cleaning. It is possible that there could have been some testing apparatus with these elements surrounding the X-links that caused the contamination.

The arc-jet samples exhibited evidence of trace amounts of nitrogen within the deposits; as shown previously, nitrogen was only observed in section G.1 for the X-links. Refer to Chapter 6.1.2 for additional discussion. While it is most likely that nitrogen content is dependent of degree of reaction, it is also possible that the air content within the arc-jet versus different from the air content for the X-links during re-entry. In addition, lack of sensitivity of the instrument paired with peak shifting and mixing of oxides may have shielded the titanium nitrides from detection.

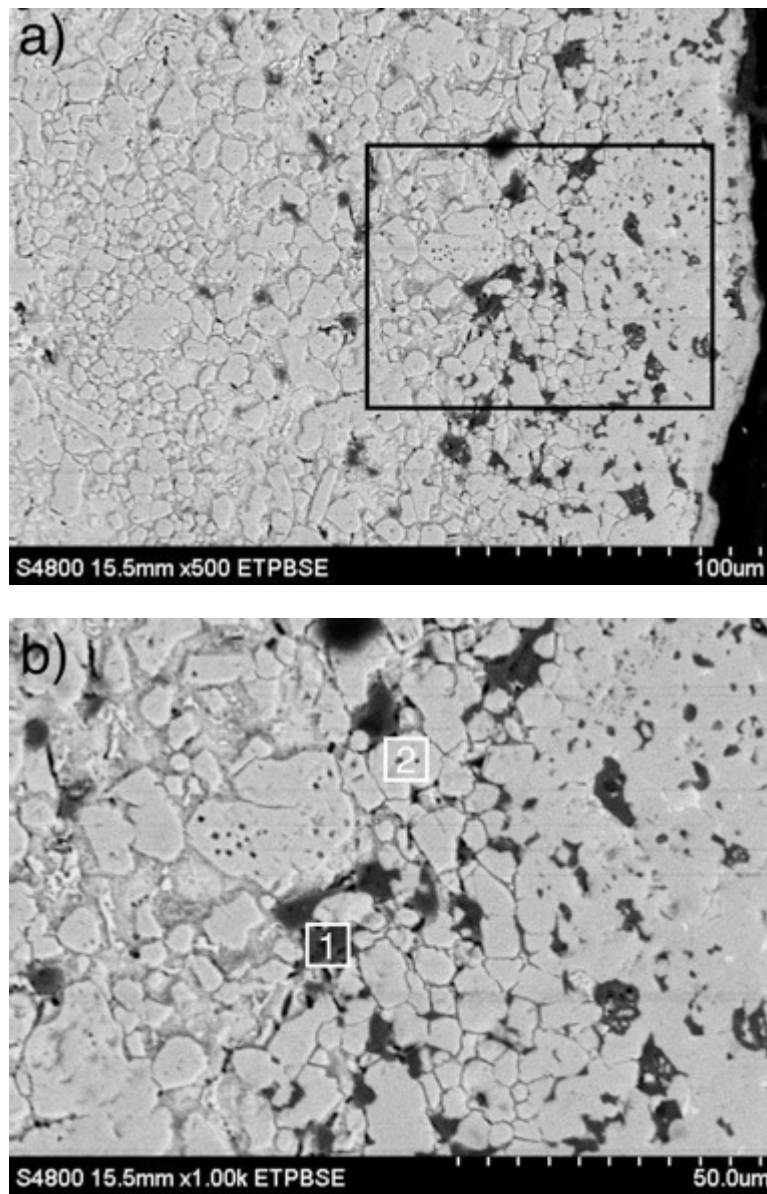


Figure 6.15. Backscattered electron microscope images of Class II arc-jet specimen 16, with close-up of (a) in (b).

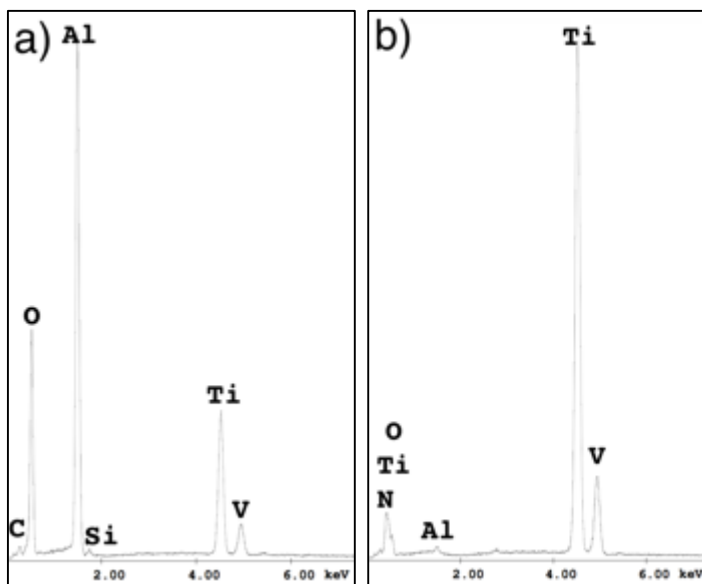


Figure 6.16. EDS spectra of Class II arc-jet specimen 16 with box 1, intergranular deposit (a) and box 2, granular features (b) in Figure 6.15b.

Specimen 17

Specimen 17 deposit features were not documented in Chapter 5 and will be discussed here. The two images in Figure 6.17 were taken at the same area. Figure 6.17(b) is located to the immediate right of Figure 6.17(a), with the white arrow in (a) indicating the direction in which image (b) was taken. EDS scan areas are boxed in Figure 6.17(b). Spoke-like solidification structures (see black arrow in Figure 6.17a) were observed throughout the arc-jet samples, specifically shown for Specimen 17 in this section. It was initially thought that these were a result of particulate metal combustion resulting in a star-like morphology, discussed in [76] and [104]. Upon further investigation, it was observed that the star-like morphologies contained some amount of silicon. Referencing semi-quantitative EDS results, silicon amounts as low as 5 wt.% were observed within the unique solidification structures. It appears that the addition of silicon to the titanium changes the surface tension properties, resulting in a disperse phase with a star-like morphology. The acicular structures seen to the left in Figure 6.17(a) are of the acicular Ti-6Al-4V bulk metal microstructure, and not the subject of discussion.

Specimen 17 had a thick scale with a granular morphology. The granular features did not appear to coalesce, as in Class II samples, but appeared as a continuous and stable granular phase. Literature has documented grains forming in thicker scales [105]. The structures nearest the surface in Figure 6.17(b) were chemically different from the surrounding grains, and had more than 5 wt.% silicon as a

chemical constituent. It appears that the star-like features formed intergranularly and eventually diffuse into the granular structure, increasing in abundance deeper into the scale. An advancing solidification front from the surface inward, resulting in saturation of solute at the solidification front, may account for the star-like formations. Lower concentrations of silicon did not appear to produce the same effect. Note the absence of nitrogen within the scales for the Class III behavior.

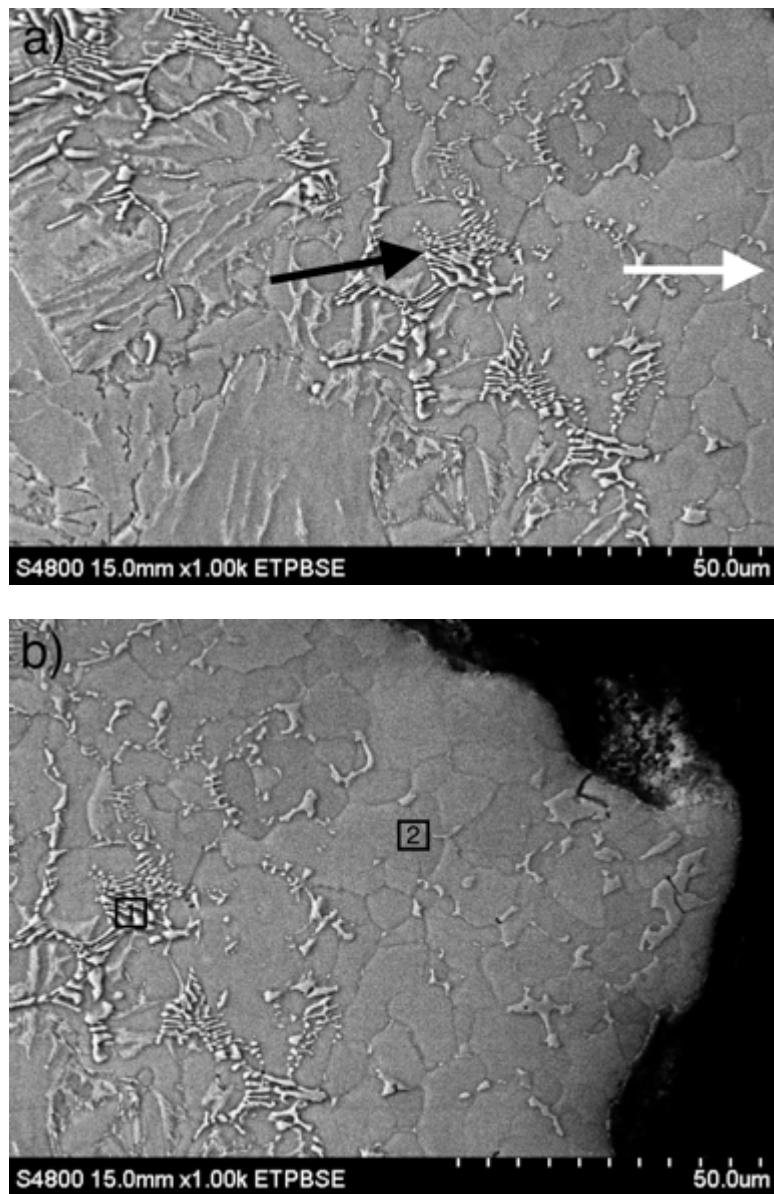


Figure 6.17. Backscattered electron microscope images of Class II arc-jet specimen 17, with arrow in (a) indicating location of (b).

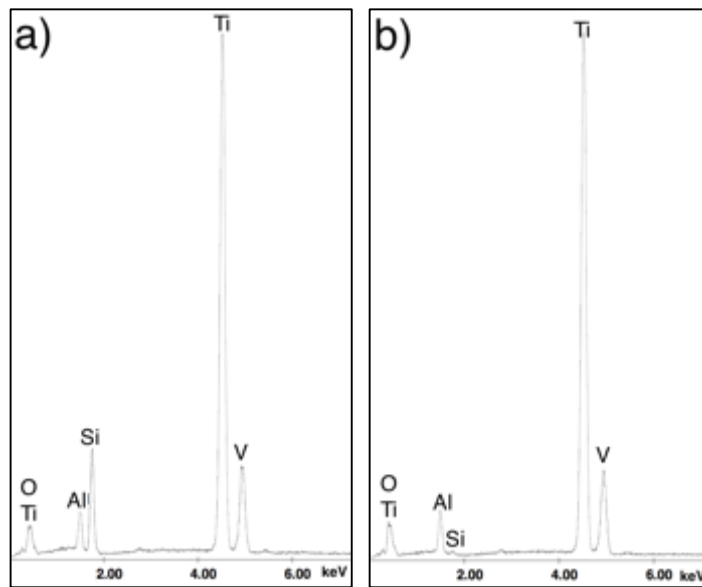


Figure 6.18. . EDS spectra of Class II arc-jet specimen 17 with box 1, star-like features (a) and box 2, granular features (b) in Figure 6.15b.

Specimen 28

Star-like solidification structures (see arrow in Figure 6.19a) were observed throughout the arc-jet samples. These shown for specimen 28 are similar to the structures shown for specimen 17 (Figure 6.17). These solidification features appear to by forming intergranularly, and increased silicon contents within the star-like features are in agreement with specimen 17. The acicular structures seen to the left of the images in Figure 6.19 are of the martensitic Ti-6Al-4V bulk metal microstructure.

Stable granular features, different from those formed in Class II specimens and X-link samples, near the surface are observed in both images in Figure 6.19. The granular features are larger and more polygonal than those observed in the X-link samples. The coalescing granular features observed throughout the other titanium samples appear to have evolved into stable grains, suggesting some threshold condition in which parabolic oxidation rate is reached. It is also true that the arc-jet samples were not exposed to the rotations and atmospheric changes that the X-links were, and had a higher likelihood for quasi-stable scale development.

EDS spectrum of the surface grains versus the inner grains were the same, consisting primarily of Ti-6Al-4V constituents and oxygen. The granular features near the surface were contaminated with sodium, magnesium, and fluorine. The exact origin of these constituents is unknown. Note the absence of nitrogen within the scales for the Class III behavior.

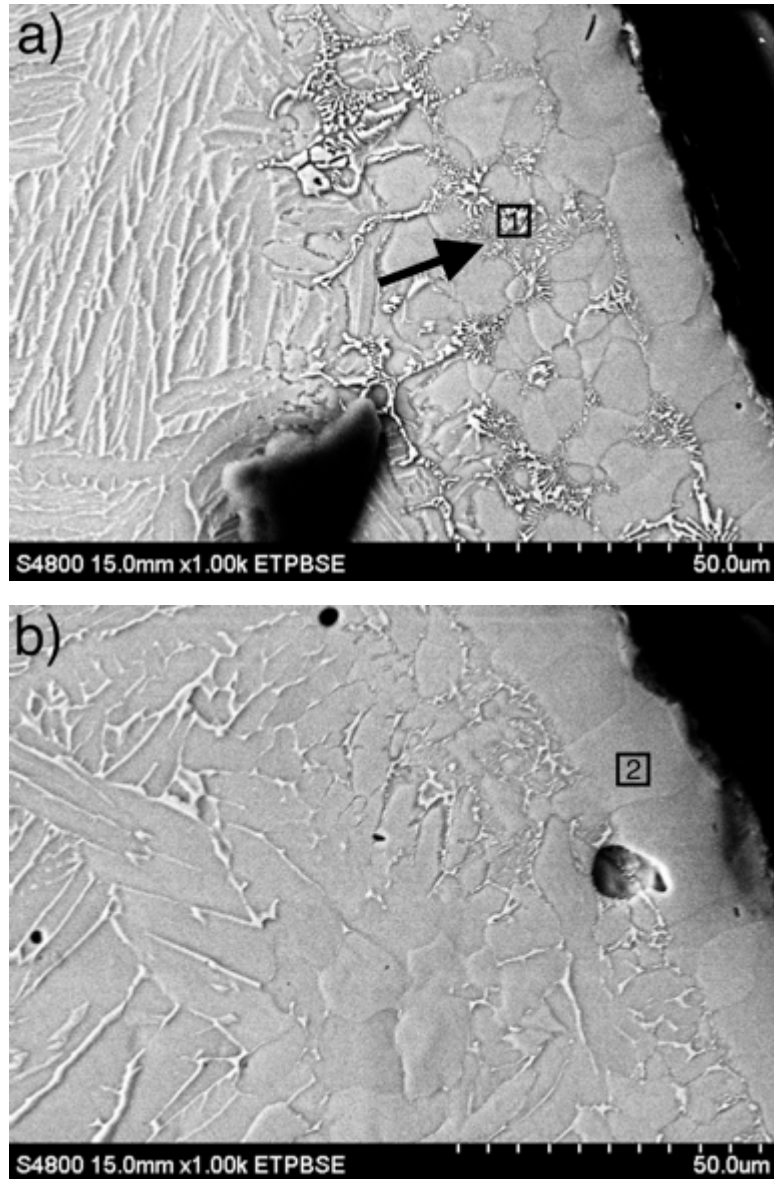


Figure 6.19. Backscattered electron image of star-like morphology (a) granular features in both (a) and (b) in Class III arc-jet specimen 28.

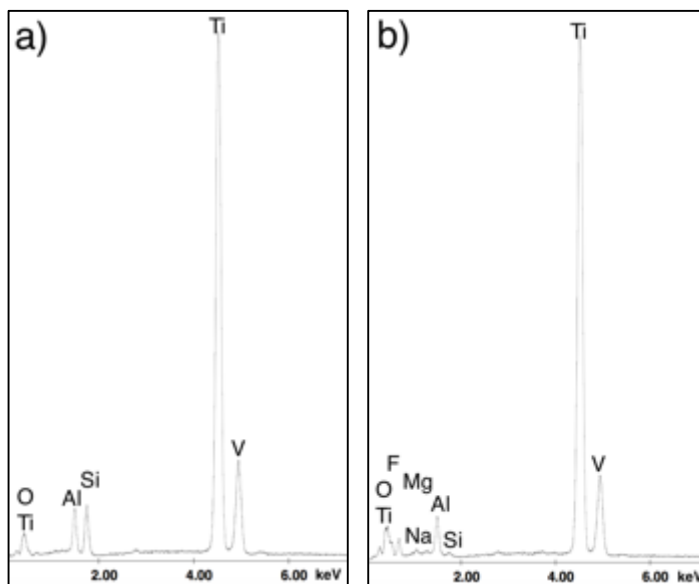


Figure 6.20. EDS spectra for Class III arc-jet specimen 28 of box 1, star-like solidification features in Figure 6.5a (a) and box 2, granular top layer in Figure 6.5b (b).

6.2.3 X-ray Diffraction

For comparative purposes, diffraction patterns of Class II and Class III specimens are shown in Figure 6.21 and Figure 6.22, respectively. Non-stoichiometric titanium nitrides were observed in the Class II samples, but not in the Class III samples. This is likely due to the volatilization of titanium nitrides as the reaction progresses. This presence of nitrogen in the arc-jet samples versus the X-links could also be due to differences in air content of the arc-jet versus the actual re-entry environment, the combustion reactions in these pieces not progressing in the same manner as X-links did, similar lattice parameters between titanium oxides and nitrides shadowing the presence of nitrides, or limited instrument resolution.

Titanium rich oxides Ti_3O and Ti_6O , also found in the X-link samples, were observed. Higher concentrations of the hexagonal structured titanium rich oxide Ti_2O , were found in the more physically degraded Class III material. The hexagonal lattice suggests that the Ti_2O formed as oxygen diffused interstitially into titanium to form an ordered lattice. These titanium rich phases are most likely detected at the surfaces where the scale and metal meet. Ti_2O_3 is found in the Class II samples and in less physically degraded material X-link sections D.6 and G.1. The Magneli-type phase Ti_4O_7 appears in Class III reactions. Ti_3O_5 is less stable than Ti_2O_3 , but is still present in the Class III samples. Noting

Figure 2.4, Ti_2O_3 and Ti_3O_5 fall within the same region in the phase diagram with high temperatures ($T > 1000^\circ\text{C}$) and oxygen concentrations above $\sim 30\%$.

The Class II specimens show more diverse oxide species than the Class III specimens. As discussed in Chapter 5.3.3, it is highly probable that as the reaction progressed, lower level oxides volatilized and higher oxides remained.

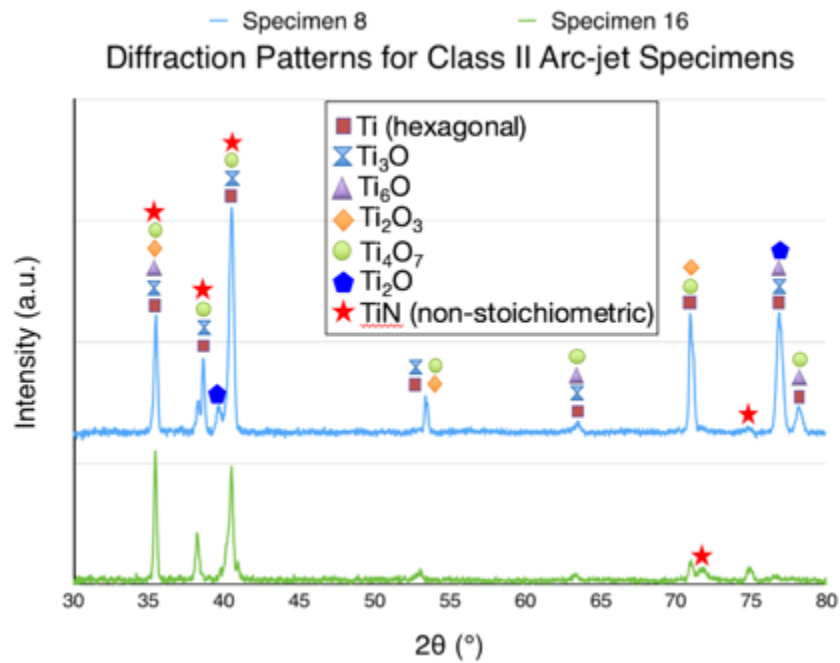


Figure 6.21. Diffraction patterns for Class II arc-jet specimens 8 and 16.

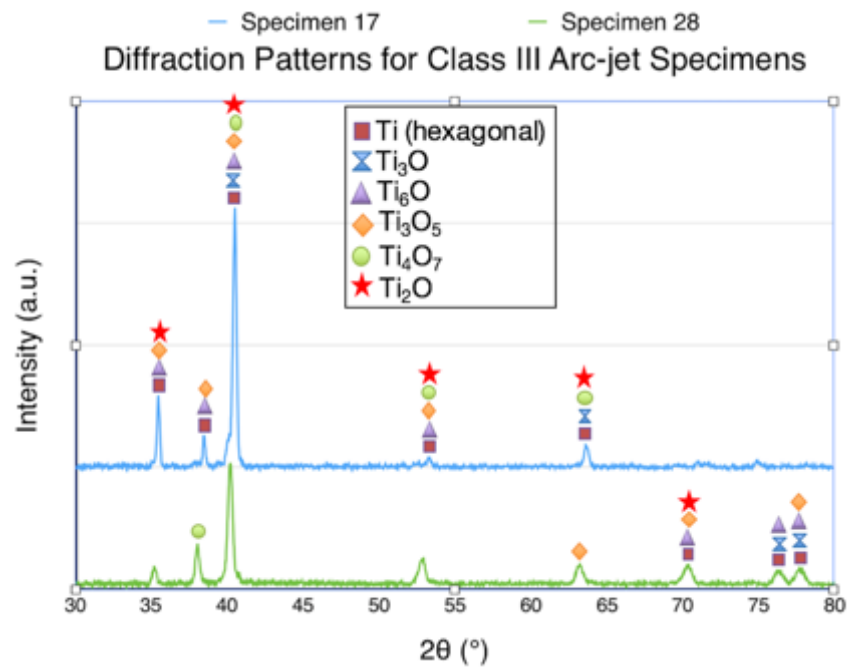


Figure 6.22. Diffraction patterns Class III arc-jet specimens 17 and 28.

Chapter 7: Heat Treatment Study Results

A heat treatment study was designed to determine the effect of higher solutionizing temperatures on microstructural features. This is not a commercially valued aspect, as it requires “burning” the material and diminishing properties. Regardless, these structures were pertinent to the research question, given that the vehicle met and exceeded temperatures above the melting temperature of titanium. It is understood that this study does not encompass all factors that affect microstructural features, to include cooling rate, solutionizing time, and deformation. This study functioned as an exploratory attempt at relating observed microstructural features to possible temperature exposure ranges. A quick cooling rate (water quench) was chosen based on the known structures and most likely history of the X-links. The arc-jet samples did not have anomalistic microstructural features, and therefore a slower air cool was not of interest. A test matrix is shown in Table 7.1. All 1/8 in. thick samples were wrapped in titanium getter foil to minimize metal oxidation. Two samples per heat treatment were treated, and all samples were quenched in room temperature water after solutionizing for 15 minutes at the target temperature. Heat Treat 12 was included as a single data point to examine the effect of solutionizing time on microstructural features. Five microhardness readings were recorded from the centers of the samples and averaged for the averages shown.

Heat Treat 6 experienced a delay in water quench while testing, producing a lower microhardness and thus lower overall microhardness average, seen in Figure 7.3. For Heat Treat 6, the microstructure shown in Figure 7.1 corresponds to that which did not experience a delay in quenching.

Table 7.1. Test matrix for heat treatment study.

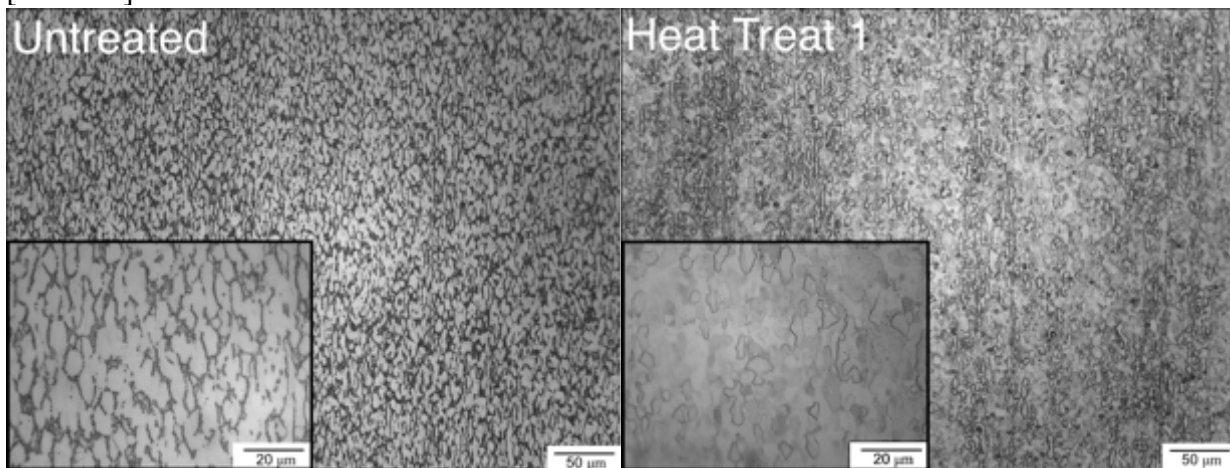
Set #	Solutionizing Temperature (°F)	Solutionizing Time (minutes)
Untreated	Untreated	N/A
Heat Treat 1	1650	15
Heat Treat 2	1750	15
Heat Treat 3	1850	15
Heat Treat 4	1950 (β -transus)	15
Heat Treat 5	2050	15
Heat Treat 6	2150	15
Heat Treat 7	2250	15
Heat Treat 8	2350	15
Heat Treat 9	2450	15
Heat Treat 10	2550	15
Heat Treat 11	2650	15
Heat Treat 12	2650	30

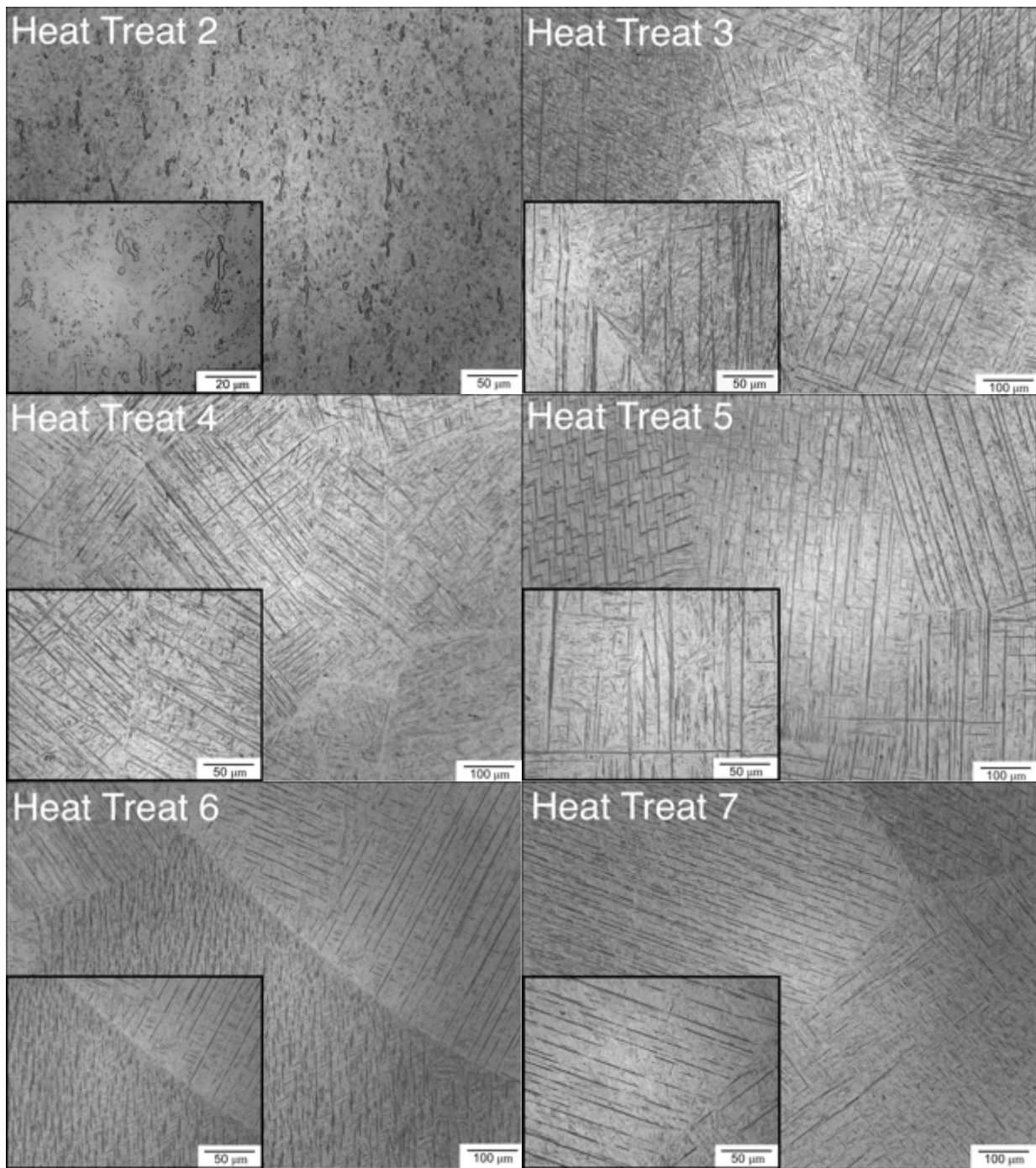
7.1. MICROSTRUCTURAL FEATURES

Original magnifications of all images are 100X with a 200X inlay, with the exception of the Untreated, Heat Treat 1, and Heat Treat 2 samples, which are shown at 200X with a 500X inlay, in order to properly display features of interest. The Untreated sample corresponds to the initial microstructural features of the arc-jet coupons, discussed previously in Chapter 5.3.1. Figure 7.1 catalogs the microstructural features of all heat treated samples.

The microstructure begins in the untreated state as a slightly aligned, fine grained primary α in a lamellar $\alpha+\beta$ matrix. In Heat Treats 1 and 2 (below the β -transus temperature), some primary α islands remain within a dispersed β matrix. It is noted that the β shown for Heat Treats 1 and 2 is quite similar to the diffuse β existing at the outboard sides of the starboard X-link. Heat Treat 3, performed just below the β -transus, produced a large grained, acicular α structure. Heat Treats 3 through 5 (1950°F-2050°F) maintain this acicular, large grained structure, with a slight increase in grain size. The α and β within the

grains appears as a Widmanstätten structure. Heat Treats 6 and 7 (2150°F-2250°F) transition to a more aligned β structure, suggesting that higher temperatures lead to a larger prior β grain size during the solutionizing step. Heat Treats 8 and 9 (2350°F-2450°F) consist of “stringy” α , and are very β heavy, which commonly occurs when held at a high solutionizing temperature [106]. The “stringy” alpha is like due to formation of the martensitic alpha on a habit plane. Heat Treats 10 and 11 (2550°F-2650°F) produced microstructures with increased α and a β that appeared to align and emanate from the grain boundaries. The increased α could be due to higher temperatures, increasing the diffusion rate of oxygen into the surface and thus increasing the percentage of α within the grains. Heat Treat 12, treated at 2650°F for 30 minutes, has α lamellae segments divided into recrystallized grains, with an acicular α + β mixture between α lamellae. The getter foil provided insufficient protection given the extended exposure time, and this structure very strongly corresponds to an α case. In summary, the microstructure transitions from α in a lamellar α + β matrix, to disperse β in acicular α , to acicular α in large prior β grains, with an increasing then decreasing percentage of β with increasing temperature. Grain boundaries become difficult to distinguish at the given magnifications in Heat Treats 8-11, which is consistent with literature findings that larger β grains result from higher solutionizing temperatures [106-107].





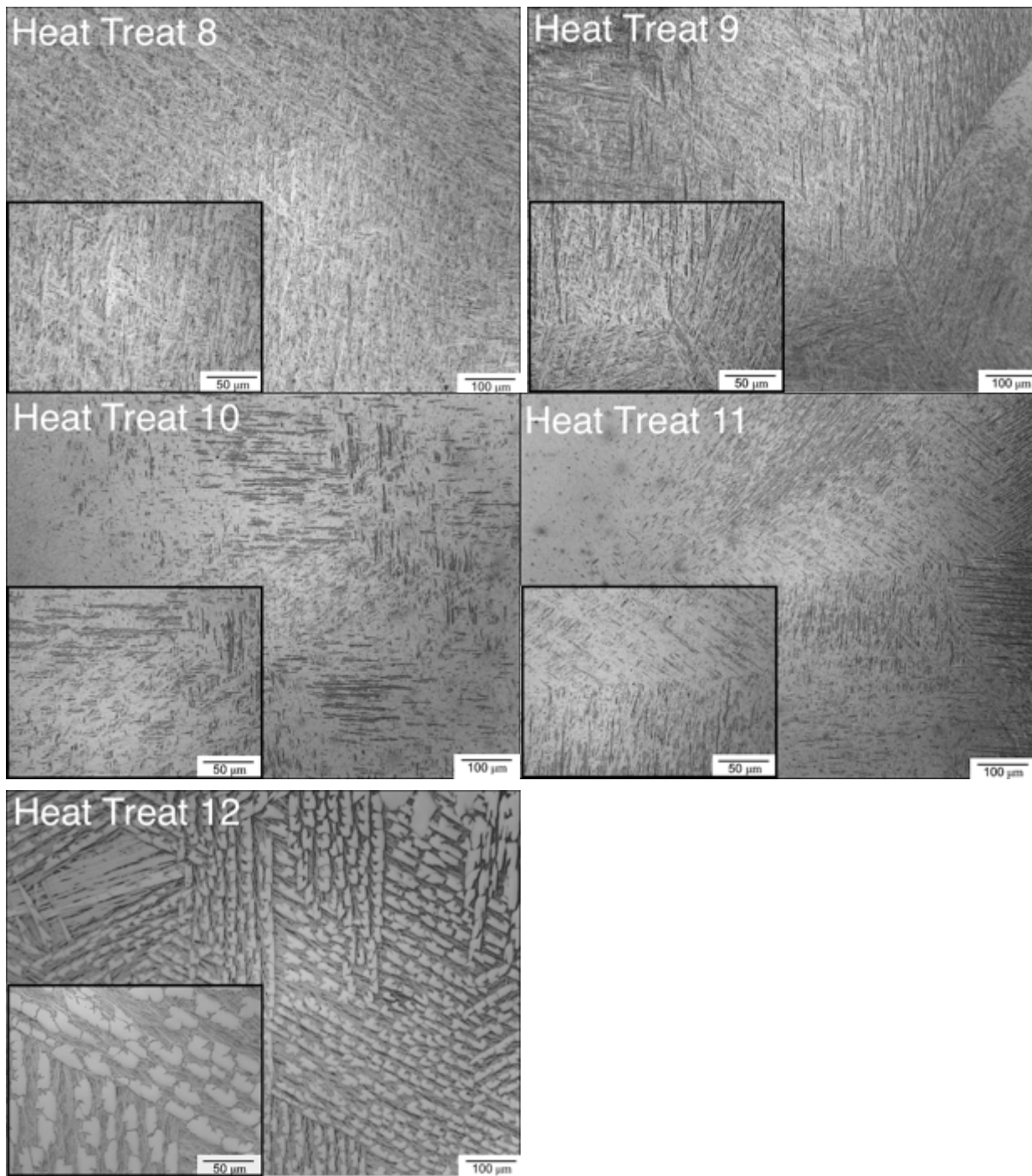


Figure 7.1. Microstructural features of samples in heat treatment study.

7.2 MICROHARDNESS TESTING

A plot of average microhardness values of the heat treated samples is shown in Figure 7.2. There were slight differences in the microhardness values between samples of the same heat treatment, attributed to the dependence of indentation location and phase constituents present (Figure 7.3). An

initial increase in microhardness is observed in Heat Treats 1 through 3 until the β -transus (1950°F) is reached at Heat Treat 4, at which point microhardness decreases slightly. The initial microhardness increase is associated with the formation of acicular structures; the slight plateau at the β -transus temperature is consistent with findings in literature [107]. It was previously noted that a delay in water quench of Heat Treat 6 could have caused a more exaggerated decrease in microhardness. The microhardness reading of the sample with a quench delay was 316 HV, while the optimum sample was recorded as 398 HV. Compared to the microhardness value of the Heat Treat 6 sample that did not have a delayed quench and those of the other heat treatments, it can be inferred that had this quench delay not occurred, the average microhardness value for Heat Treat 6 would have been similar to those for Heat Treats 5, 7, and 8. If this inference is made, the trend would instead be a plateau for Heat Treats 5 through 8, and then an increase from Heat Treats 9-12, corresponding to large grains and increasing α in the structure.

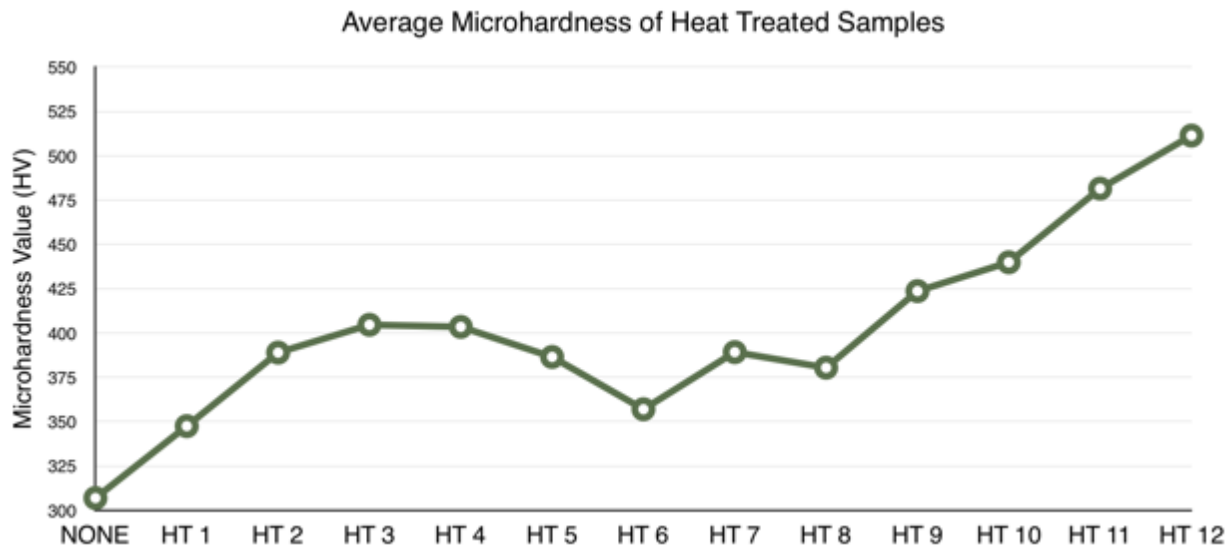


Figure 7.2. Average microhardness readings of the heat treated samples.

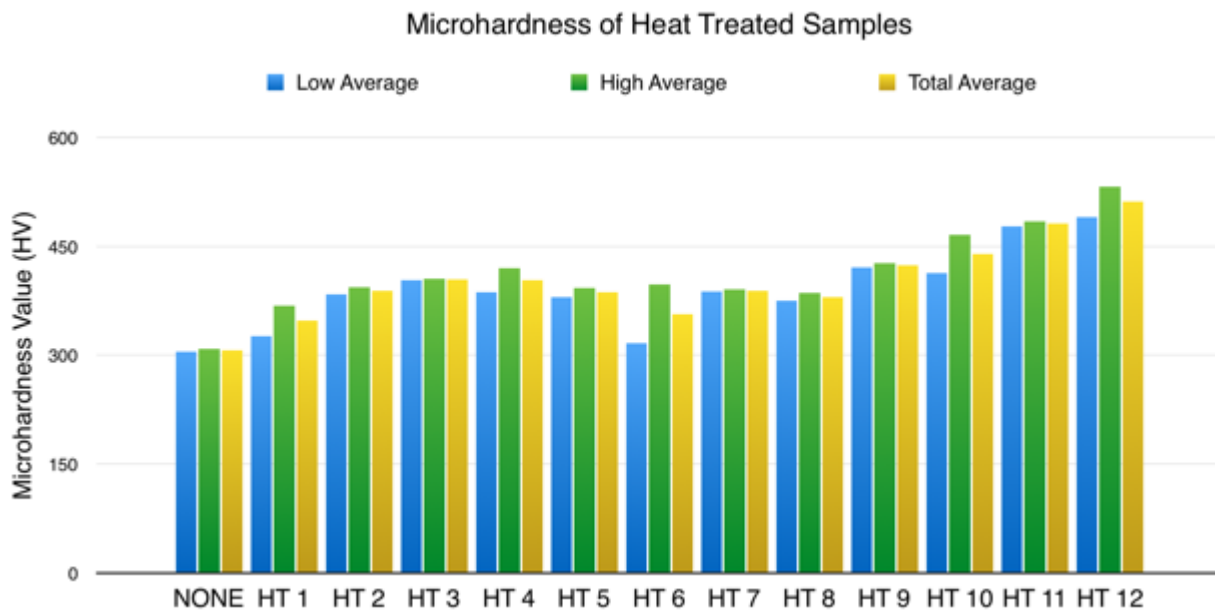


Figure 7.3. Plot showing average microhardness readings versus low and high reading from the two samples analyzed per heat treatment.

7.3 SUMMARY/FINDINGS

Unfortunately, this study did not shed light on the interesting microstructural features observed to the features of the X-links (see Chapter 4 and 5). Further discussion into X-link and arc-jet structures and possible theories for their formations can be found in Chapter 5.4.

The average microhardness values recorded for the X-links and arc-jet samples did not correlate to the average microhardness values of heat treatment; the recorded values were much higher for the heat treated samples and correlate more closely to alpha case microhardness values. Heat treatment 3 is where the characteristic martensitic α structures began, and the recorded microhardness was well above even the highest average microhardness of the X-links and arc-jet samples. The general increasing trend of hardness shown in Figures 7.2 and 7.3 is likely caused by increased permeation of α into the material that increased with increasing temperature.

Chapter 8: Conclusions

8.1 SUMMARY AND CONCLUSIONS

8.1.1 Microstructural Features: LOM

Microstructures have been compiled to produce a suggested temperature exposure map of the starboard X-link, shown in Figure 9.1. All inboard micrographs are at an original magnification of 100X. All outboard micrographs are shown at the original magnification of 200X, with a 500X inlay. They are separated into inboard and outboard side and was compiled using scientific knowledge and microstructures located in [108], [109], and [110]. All microstructures appear to have undergone a quick cool, similar to a water quench, based upon findings in the literature.

The inboard microstructures changed from large grained martensitic α within large prior β grains (section D.2) to progressively smaller grains (sections D.6 and E.2), then to a smaller grained serrated α structure (section G.1). A temperature gradient is proposed, with the martensitic α forming at the highest temperature, smaller grained martensitic alpha corresponding at a lower, and serrated α being the lowest temperature structure.

Comparison with the features observed at the outboard sides, this temperature gradient is confirmed. At the outboard side, there existed a basketweave of diffuse β forming between acicular α colonies. Outboard material further away from the burn through in the flange, and more aggravated flow, exhibited more α islands than those closer to the flange. This basketweave structure was similar to the initial microstructural state of the X-links observed through metallographic replication. The resemblance suggests that the outboard side is an intermediate structure that occurs upon exposure to a higher temperature, or is held at temperature for a longer period of time. Further evidence substantiating this finding can be found in [108] and [109], which show micrographs exhibiting complementary diffuse β features with some α islands. The sources do not elaborate further on the nature of the alpha islands. Conference proceedings previously presented and published as a conference proceeding through MS&T 2015, Chapter 4 in this dissertation, recorded that these α islands were remnants of primary α in the microstructures. This previous conclusion was created during the early stages of data gathering and analysis. Later research suggested that these were not primary α islands, but structures analogous to

serrated α . Thorough viewing of the samples revealed that these islands were often polygonal and irregular. The literature also suggests that the diffuse β structures form upon exposure to temperatures slightly above the β -transus, above which primary α would no longer exist. The drastic change in microstructural features from inboard to outboard side is likely due to conductive heating effects caused by the transition from a relatively thin section of titanium ($\sim 1/4$ inch) to a thicker piece of titanium (~ 1 inch), causing the outboard side to stay hotter for a longer period of time. Considering that the outboard side of the X-links appears to have remained at higher temperatures longer as a result of the geometry of the X-link, the material likely remained hot long enough to transform all of the primary α .

Several microstructural relationships were noted regarding the inboard side of the X-link and arc-jet samples. The arc-jet microstructural characteristics were generally uniform, and coincided with the inboard side of the X-link. Uniform features are to be expected from arc-jet samples because quasi-stable conditions are maintained. From leading edge to trailing edge, a slight decrease in grain size could be discerned, but the changes were so minute that the quality was not believed to be of major consequence. Data of arc-jet samples not analyzed in this work [111] showed that even amongst the same classes of material response, and even identical enthalpy and dynamic pressure values, microstructural differences between samples were found. These differences appear to be inherent to the material response and testing conditions. Some of the titanium plates ignited within seconds of testing, while some stayed in the arc-jet conditions for several minutes before ignition. The indicated illustrates the complexity of the titanium combustion. Temperature, time, testing parameters, and many other factors can account for this information. Initially, α case thickness was of interest, but the dynamic and ambiguous nature of the environment led to incongruous results. Hence, α case thickness quantification did not provide any further clarification of environmental conditions or material history.

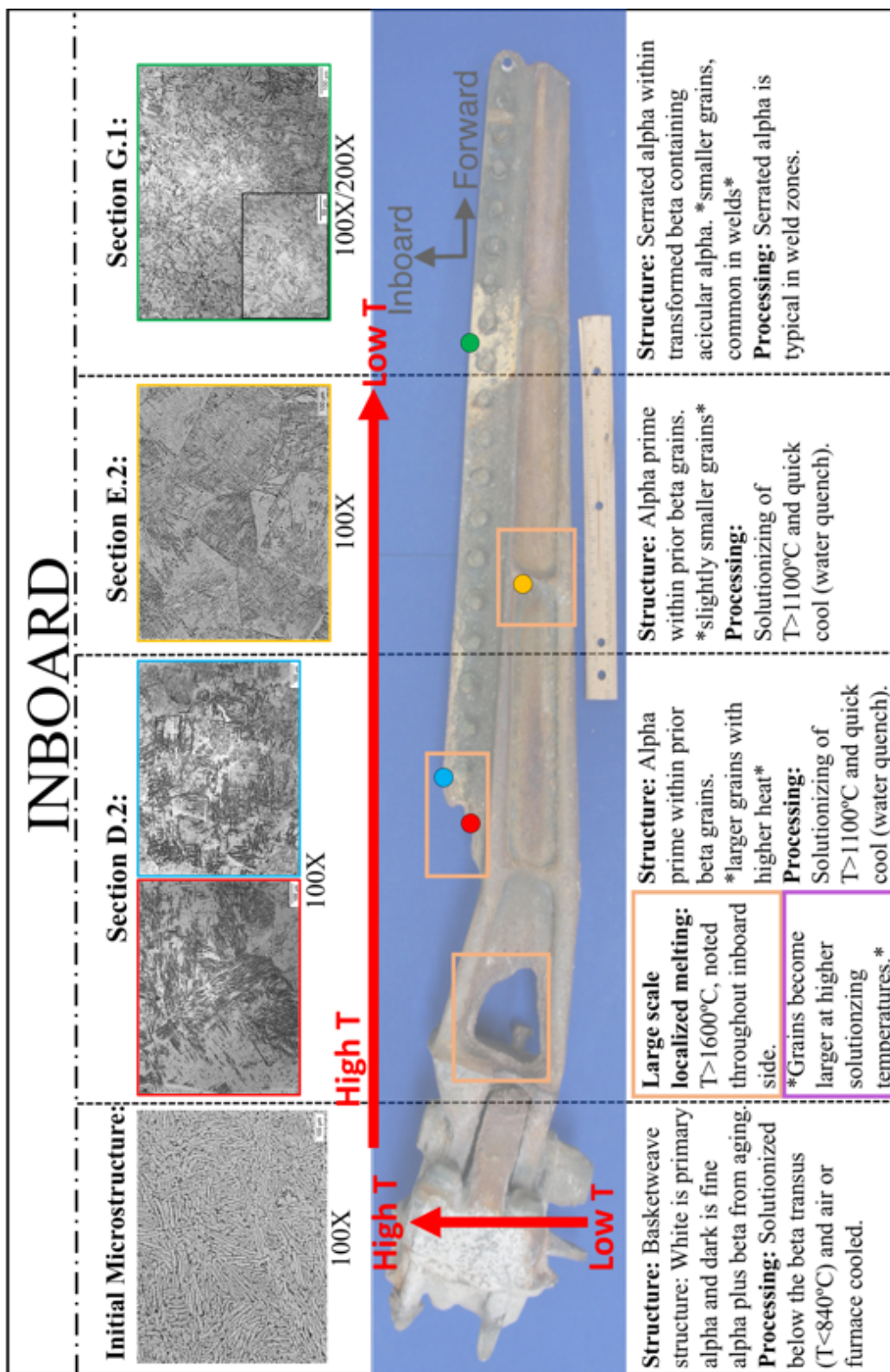


Figure 8.1. Suggested temperature map of the X-links based on microstructural features observed at the inboard side.

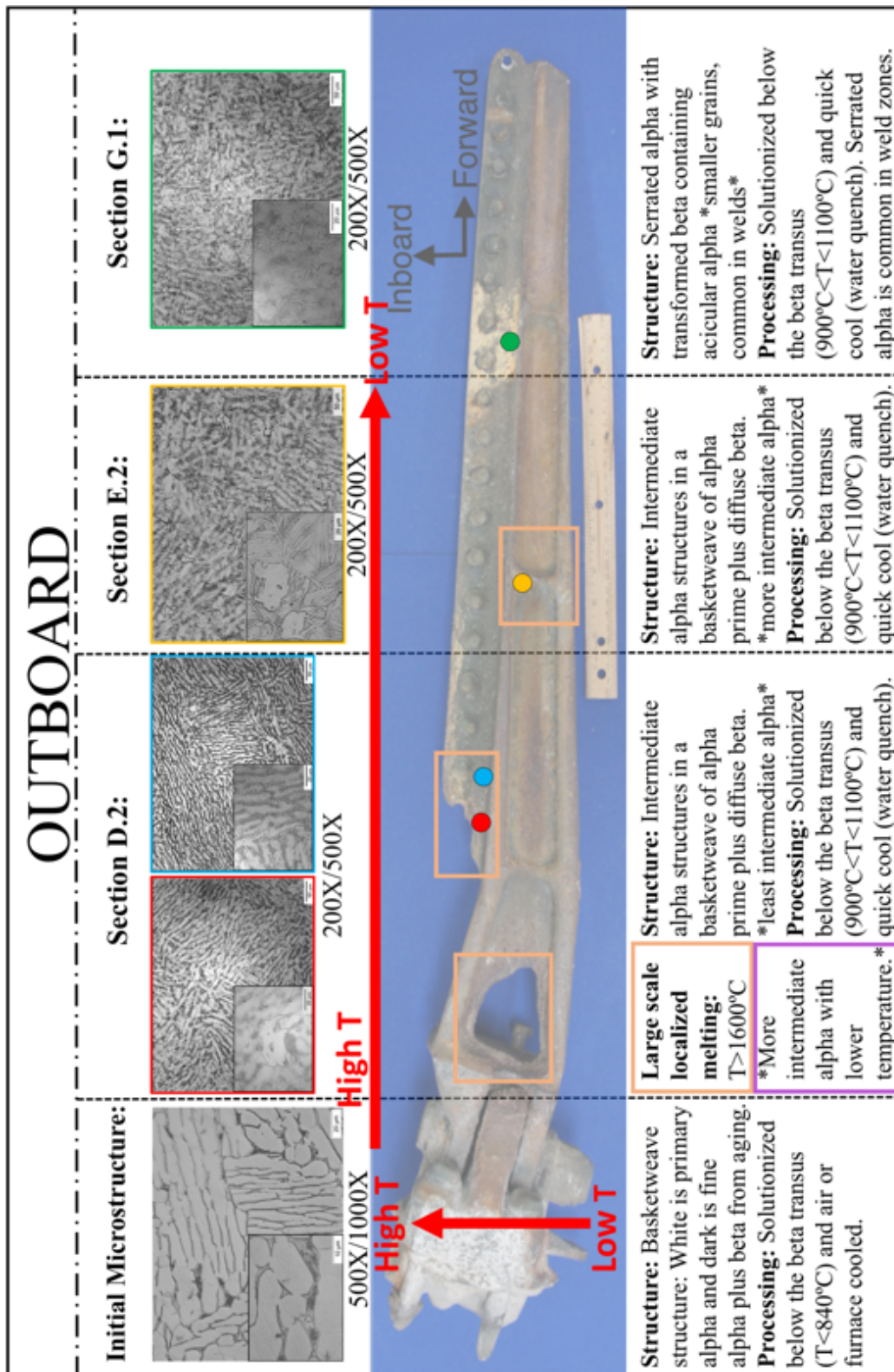


Figure 8.2. Suggested temperature map of the X-links based on microstructural features observed at the outboard side.

8.1.2 Deposit Characteristics: SEM/EDS

An effort was made to quantify data observed in the deposit features, but meaningful conclusions could not be drawn based on that data alone. The deposits were non-uniform, dissimilar, and thickness of deposit was highly dependent of locational relationship to the burn through in the flange for the X-link samples. Correspondingly, arc-jet deposit thickness was dependent on amount of melted titanium during testing. As to be expected, areas where large mass loss was prominent had larger concentrations of solidified deposit. Coincidentally, the inboard side (where flow appeared to be more pronounced) had more deposits than the outboard side. Sections E and G.1, further from the aggravated flow, had less deposits than section D. Gravitational and relational dependences to other components also came into play. The arc-jet samples possessed thicker deposits at the trailing edge, since the arc-jet flow forced molten material from leading to trailing edge. Therefore, there is difficulty in drawing definitive from the layering, thickness, or individual nature of the deposits.

Generally, the deposits consisted of titanium oxides, with some foreign contamination within the oxides. Relationships between location of foreign contamination were difficult to confirm for the X-links. Foreign contamination within arc-jet samples appeared more heavily nearer the surface. EDS spectra of the X-links showed MP35N fastener, structural steel, and copper mixed in with the titanium oxides. EDS spectra of the arc-jet samples showed silicon carbide fixture plate material, magnesium, sodium, and fluorine mixed in with the titanium oxides. The origin of the magnesium, sodium, and fluorine are not known, but may originate from the thermocouples, fixture screw, or other testing equipment present in the arc-jet.

A notable difference in EDS spectra was the presence of nitrogen only in the arc-jet Class II and X-link section G.1 samples. In perspective, section G.1 was furthest from the aggravated flow, and exhibited negligible mass loss compared to the other X-link samples. Small amounts of nitrogen (<1 wt.%) were observed in arc-jet samples and section G.1. Lack of nitrogen resolution in the other arc-jet samples can be attributed to several reasons: volatilization/reduction of nitrides prior to the quench, according to the Ellingham diagram and lower stability of titanium nitrides versus titanium oxides; release of nitrogen from the melt, as literature suggests that nitrogen may have initially been a part of the combustion reaction to volatilize later in reaction; a difference in environmental conditions and air

content between the atmosphere the X-links and arc-jet samples were exposed to; or potential mixing of the oxides and nitrides paired with the small documented concentrations prevented resolution of these compounds within XRD patterns (discussed in more detail below).

Granular features coalescing to form a boundary were observed in the top-most layers of the deposits. The granular features of the arc-jet were more polygonal and faceted, while the X-link features were more spherical and rounded. Of interest were the granular features observed in the Class III samples, in which the features had already coalesced and formed a stable matrix of grains. This suggests that the grains in Class III samples reached some critical condition in which grains were allowed to grow. The scales in this area were also quite thick (~ 0.5-2 mm), and literature reports that thicker scales tend to form stable grains. Rotational and gravitational effects produced by break-up of the vehicle likely prohibitive for the stable oxide grain formation in the X-links.

8.1.3 Oxide Characteristics: XRD

X-ray diffraction data revealed a wealth of oxides present on the samples. The nature of the data also suggests non-stoichiometric oxides and mixing due to observed peak broadening and shifting. The oxides indicated by the XRD data were of the form Ti_xO and Ti_xO_{2x-1} . Oxides of the form Ti_xO_{2x-1} form when TiO_2 (rutile) and titanium metal react at higher temperatures ($T > 800^\circ C$). Referencing the titanium-oxygen binary phase diagram, the oxides form suggesting oxygen contents in excess of 30%. This portion of the graph has not yet been experimentally confirmed, and there may be some higher oxides present in this section.

Some relationships were found in the oxide data, but solid correlations could not be formed. For example, orthorhombic TiO_2 , typically associated with the brookite phase, was found in sections E.2 and G.1. Both of these were less thermally degraded than section D. Magneli phases with higher “x” values were found on the more reacted material of sections D.2, D.6, E.2, G.1 inboard side, and Class III arc-jet samples. Ti_2O_3 was resolved in Class II arc-jet samples and section D.6, which is relatively less degraded material. Lastly, nitrides were observed through EDS in section G.1 and by EDS and XRD in the Class II arc-jet samples. Because section G.1 is the least thermally degraded of the X-link samples, it is theorized that all other samples surpassed some thermodynamic threshold that resulted in

volatilization of the nitrides, leaving only oxides to be resolved. For section G.1, the low nitrogen concentration makes it plausible that the nitrogen peak lies within the other titanium oxide peaks, owing to their similar lattice parameter; another explanation is instrument sensitivity was not great enough to resolve that specific nitride.

A significant finding discussed in Chapter 5 was that more diverse oxide species were resolved within less physically degraded material (section D.2 and Class II) than the more physically degraded material (section D.6 and Class III). This is believed to have occurred due to volatilization of lower oxides, leaving more oxides to be detected in the less physically degraded material. This once again references some threshold condition above which oxides volatilize and below which they remain, and is consistent with literature. Also of note is lack of TiO_2 (rutile) detection, which is consistent with combustion of the alloy, producing higher temperature oxides upon reduction of the rutile phase.

8.1.4 Mechanical Properties: Microhardness Testing

All microhardness readings were recorded traversing from inboard to outboard side and leading edge to trailing edge for the X-link and arc-jet samples, respectively. Section E.2 is the exception as those microhardness readings were taken from top to bottom sides. There were no preferential testing sites; all readings were taken through the center of the sample at fixed distances. The microhardness testing data was difficult to interpret due to the intrinsic nature of the two-phase alloy. The harder α phase produced sharp increases in the data while the softer β phase produced sharp decreases. At the inboard sides and leading edges, a high hardness was observed at the α case. No correlation could be made between the location along the X-link or classification of arc-jet material response in α case hardness. It is difficult to ascertain how long the pieces were subjected to the atmosphere when accounting physical removal processes of the protective scale, vehicle rotations, and length of oxidation and ignition processes taking place. Metal oxide rich deposits were harder than the α cases, and were around 600-700 HV.

Arc-jet samples tended to have α cases that permeated further into the sample; these samples also had higher average microhardness readings than the X-links. This can be due to the fine-grained initial microstructure, the nature of the cooling event, or the thicker α case increasing average hardness.

For the X-links, listed from the highest to lowest average microhardness are: section E.2, D.2, D.6, and G.1. Focusing only on those samples in the forward-to-aft flow region that existed along the fastener heads (sections D.2, D.6, and G.1), a discovery of higher average hardness nearest the burn through in the flange was made. This can be attributed to the changing microstructures discussed previously, which are shown in Figures 8.1 and 8.2. Data suggested that martensitic α is harder than serrated α , and that the presence of increased α islands produces a lower microhardness.

8.2 RECOMMENDATIONS AND FUTURE WORK

This work was performed to determine the material response and identify a mechanism of material combustion under differing re-entry conditions. As with any materials characterization effort, one can always dig deeper. The materials characterization work presented here provides an introductory understanding of the response of Ti-6Al-4V in the high enthalpy, oxygen rich environment of re-entry. Some results obtained raised questions fit fuel future research directions.

Based on the complex nature of the microstructures observed at the outboard side of the X-links, electron backscattered diffraction (EBSD) would be helpful to further understand the orientation and phase distribution within the microstructure. While similar microstructures have been observed possessing the diffuse beta quality, little is known about the actual nature of the phases. Furthermore, the complex nature of the non-stoichiometric oxides caused by mixing warrants further explanation. A suitable tool with which to analyze is microprobe analysis; microprobe analysis could provide quantitative analysis of the deposits, allowing for a full understanding of chemical constituents present. This analysis could help discern trace amounts of nitrogen within the deposits, allowing for the researcher to differentiate between conditions where titanium nitrides still remain a reaction product. Lastly, transmission electron microscopy (TEM) would be helpful in understanding the α'' structures, given that those are only resolvable with TEM. Knowledge of the concentration and morphology of the α'' within the microstructure would yield information regarding material processing. Knowledge of the diffuse beta phase and dislocation structure between phase could also be gained with TEM work.

This introductory investigation into the oxidation, ignition, and combustion behavior of the Ti-6Al-4V alloy has uncovered information on the microstructural constituents and morphology, titanium

oxide and nitride formation, and mechanical properties of the common aerospace titanium alloy when subjected to extreme heats associated with combustion reactions. The results of this work demand a thorough safety verification of the alloy in re-entry conditions, in the case that an exposure ever occurs, so that degradation mechanisms can be predicted and severity of material response understood. Future work will enhance current knowledge of the subtleties and complexities associated with bulk metal combustion and aid in problem solving efforts when utilizing this alloy in a space environment.

References

- [1] "Columbia Accident Investigation Report," National Aeronautics and Space Administration, 2003.
- [2] T. Schlatter, "Atmospheric Composition and Vertical Structure," *Environmental Impact and Manufacturing*, vol. 6, 2009.
- [3] "Columbia Crew Survival Investigation Report," National Aeronautics and Space Administration, 2008.
- [4] R. Savino, M. De Stefano Fumo, D. Paterna, A. Di Maso and F. Monteverde, "Arc-jet testing of ultra-high-temperature-ceramics," *Aerospace Science and Technology*, vol. 14, pp. 178-187, 2010.
- [5] National Aeronautics and Space Administration, [Online]. Available: http://www.nasa.gov/centers/johnson/engineering/human_space_vehicle_systems/atmospheric_re-entry_materials/index.html.
- [6] J. D. Olivas, B. Mayeaux, P. Melroy and Cone, D.M., "Study of Ti Alloy Combustion Susceptibility in Simulated Entry Environments," in *AIAA Space 2009 Conference and Symposium*, Pasadena, CA, 2009.
- [7] J. Olivas, M. Wright, R. Christoffersen, D. Cone and S. McDanel, "Crystallographic Oxide Phase Identification of char deposits obtained from the space shuttle Columbia," *Acta Astronautica*, vol. 67, pp. 553-560, 2010.
- [8] R. Boyer, G. Welsch and E. Collings, *Materials Properties Handbook: Titanium*, Materials Park, OH: ASM International, 2007.
- [9] T. Strobridge, J. Moulder and A. Clark, "Titanium combustion in turbine engines," Boulder, CO, 1979.
- [10] E. B. K. Borisova, "Ignition of Titanium Alloys in Media Containing Oxygen," *Metal Science and Heat Treatment*, pp. 37-40, 1963.
- [11] V. Bolobov, V. Zinov'ev, Y. Shneerson and P. Chernyshev, "Conditions of using titanium alloys in pressure leaching of sulfides," *Tsvet. Met.*, vol. 3, pp. 31-33, 1998.
- [12] A. Grosse and J. Conway, "Combustion of metals in oxygen," *Ind. Eng. Chem.*, vol. 50, pp. 663-672, 1958.
- [13] A. Clark and J. Hust, "A review of the compatability of structural materials with oxygen," *AIAA*, vol. 12, no. 4, pp. 441-454, 1974.
- [14] J. Kutcha and R. Clodfelter, "Aircraft mishap fire pattern investigation," Wright Patterson Air Force Base, 1985.
- [15] R. Boyer, "An overview on the use of titanium in the space industry," *Materials Science and Engineering A*, vol. 213, no. 1-2, pp. 103-114, 1996.
- [16] C. Brooks, *Heat Treatment, Structure and Properties of Nonferrous Alloys*, Metals Park, OH: American Society for Metals, 1982.
- [17] G. Lutjering and J. Williams, *Titanium*, vol. 1, Berlin: Springer, 2003.
- [18] National Fire Protection Association, "Guide for fire and explosion investigations," 2014.
- [19] R. Pederson, O. Babushkin, F. Skystedt and R. Warren, "The use of high temperature X-ray diffractometry to study phase transitions in Ti-6Al-4V," in *Titanium alloys at elevated temperature: Structural development and service behaviour*, London, 2001.
- [20] W. Smith, *Structures and properties of engineering alloys*, McGraw-Hill Publishing, 1981.

- [21] M. Motyka, K. Kubiak, J. Sieniawski and W. Ziaja, *Comprehensive Processing: Hot Plasticity of Alpha Beta Alloys*, Amsterdam: Elsevier, 2014.
- [22] ASM International, *Metals Handbook Desk Edition*, Materials Park, OH: ASM International, 1998.
- [23] A. Khanna, *Introduction to High Temperature Oxidation and Corrosion*, 1st edition ed., Materials Park, OH: ASM International, 2002.
- [24] P. Kofstad, "High-temperature oxidation of titanium," *Journal of the Less-Common Metals*, vol. 12, pp. 449-464, 1967.
- [25] O. Kubaschewski and B. Hopkins, *Oxidation of Metals and Alloys*, 1st edition ed., London: Butterworths Scientific Publications, 1953.
- [26] N. Greenwood and A. Earnshaw, *Chemistry of the Elements*, 2nd edition ed., Boston: Butterworth-Heinemann, 1997.
- [27] I. Kornilov, "Interaction of titanium with elements of the periodic system," in *The Science, Technology, and Application of Titanium*, London, 1968.
- [28] H. Ding and L. Hihara, "Effect of embedded titanium containing particles on the corrosion of particulate alumina reinforced aluminum-matrix composite," *ECS Transactions-Light Alloys 3*, vol. 11, no. 15, pp. 109-120, 2008.
- [29] T. Reed, *Free energy of formation of binary compounds*, Cambridge, MA: MIT Press, 1971.
- [30] J. Hong, Ed., *Preparation and Characterization of materials*, New York: Elsevier, 2012, p. 588.
- [31] N. Birks, G. Meier and F. Pettit, *High temperature oxidation of metals*, 2 ed., Cambridge University Press, 2006.
- [32] ASM International, *Metals Handbook: Alloy Phase Diagrams*, vol. 3, Materials Park, OH: ASM International, 1992, p. 1167.
- [33] A. Abbud-Madrid, G. Fiechtner, M. Branch and J. Daily, "Ignition and combustion characteristics of pure bulk metals: Normal-gravity test results," in *32nd Aerospace Sciences Meeting and Exhibit*, Reno, 1994.
- [34] T. Uihlein and H. Schlegel, "Titanium Fire in Jet Engines," Munich, 1997.
- [35] T. Hirano, K. Sato, Y. Sato and J. Sato, "Prediction of metal fire spread in high pressure oxygen," *Combustion Science and Technology*, vol. 32, pp. 137-159, 1983.
- [36] C. Baukal Jr., Ed., *Oxygen Enhanced Combustion*, 2nd ed., Boca Raton, FL: CRC Press, 2013, p. 111.
- [37] A. Abbud-Madrid, C. McKnight, M. Branch and J. Daily, "36th AIAA Aerospace Sciences Meeting and Exhibit," in *Buoyancy and Pressure effects of bulk metal-oxygen reactions*, Reno, NV, 1998.
- [38] G. Markstein, "Combustion of metals," *AIAA*, vol. 1, pp. 550-563, 1963.
- [39] W. Rochelle, "Survey of titanium testing at NASA, DOE, and DOD test facilities," 2006.
- [40] V. Bolobov, "Mechanism of Self-Ignition of Titanium Alloys in Oxygen," *Combustion, Explosion, and Shock Waves*, vol. 38, pp. 639-645, 2002.
- [41] J. Stoltzfus, N. Jeffers and T. Gallus, "Burning of CP titanium (Grade 2) in oxygen enriched atmospheres," *Flammability and Sensitivity of Materials in oxygen enriched atmospheres*, vol. 13, pp. 182-197, 2012.
- [42] O. Kubaschewski and J. Catterall, *Thermochemical data of alloys*, 1st ed., London: Pergamon Press, 1956.

- [43] W. Reynolds, "Investigation of ignition temperatures of solids," Washington, DC, 1959.
- [44] J. Stoltzfus and T. Gallus, "A Method for Autogenous Ignition Temperature Determination of Metal using Induction Heating," in *Fourteenth International Symposium on Flammability and Sensitivity of Materials in Oxygen-Enriched Atmospheres*, San Antonio, 2016.
- [45] S. Kharatyan, Y. Grigor'ev and A. Merzhanov, "Ignition of titanium in nitrogen," *Combustion, Explosion, and Shock Waves*, vol. 11, no. 11, pp. 21-26, 1976.
- [46] A. Abbud-Madrid, M. Branch and J. Daily, "Ignition and Combustion of bulk metals under elevated, normal and reduced gravity conditions," in *The 3rd International Microgravity Combustion Workshop*, Cleveland.
- [47] I. Glassman, A. Mellor, H. Sullivan and N. Laurendeau, "A review of metal ignition and flame models," in *NATO AGARD Annual Meeting*, Paris, 1970.
- [48] A. Abbud-Madrid, *The influence of gravity on the ignition and combustion of bulk titanium and magnesium*, Boulder, CO: Dissertation, University of Colorado at Boulder, 1996.
- [49] P. Harrison, "The combustion of titanium and zirconium," in *Seventh International Symposium on Combustion*, London, 1959.
- [50] P. Harrison and A. Yoffe, "The burning of metals," *Proceedings of the Royal Society*, vol. A 261, pp. 357-370, 1961.
- [51] T. Brzustowski and I. Glassman, "Spectroscopic Investigation of Metal Combustion," Aeronautical Engineering Laboratory, Princeton, 1961.
- [52] M. Branch, J. Daily and A. Abbud-Madrid, "Ignition and Combustion of Bulk Metals in a Microgravity Environment," NASA, 1994.
- [53] E. Borisova and Bardanov, K.V., "Ignition of titanium alloys in media containing oxygen," *Metal Science and Heat Treatment*, pp. 37-40, 1963.
- [54] V. Bolobov, "Possible mechanism of autoignition in titanium alloys in oxygen," *Combustion, Explosion, and Shock Waves*, vol. 39, pp. 677-680, 2003.
- [55] N. Bakhman, G. Kuznetsov and V. Puchkov, "Combustion of titanium plates," *Combustion, Explosion, and Shock Waves*, vol. 36, pp. 470-475, 2000.
- [56] B. Efimov and P. Kuzyaev, "Influence of angle of attack on the combustion characteristics of titanium plates in an airstream," *Combustion, Explosion, and Shock Waves*, vol. 31, pp. 653-654, 1995.
- [57] M. Gunaji, S. Sircar and H. Beeson, "Ignition and Combustion of titanium and titanium alloys," *Flammability and sensitivity of materials in oxygen enriched atmospheres*, vol. 7, pp. 81-85, 1995.
- [58] A. Breiter, V. Mal'tsev and E. Popov, "Models of metal ignition," *Combustion, Explosion, and Shock Waves*, vol. 13, no. 4, pp. 558-570, 1977.
- [59] V. Bolobov, "Deflagration of titanium in an oxygen flow," *Combustion, Explosion, and Shock Waves*, vol. 29, no. 2, pp. 12-15, 1993.
- [60] F. Littman, F. Church and E. Kinderman, "A study of metal ignitions: The spontaneous ignition of titanium," *Journal of less common metals*, vol. 3, pp. 367-378, 1961.
- [61] J. Jackson, W. Boyd and P. Miller, "reactivity of metals with liquid and gaseous oxygen," *Materials Protection*, vol. 4, no. 1, pp. 30-33, 1965.
- [62] V. Bolobov and N. Podlevskikh, "Mechanism of Metal Ignition Due to Fracture," *Combustion, Explosion, and Shock Waves*, vol. 43, no. 4, pp. 405-413, 2007.
- [63] V. Bolobov, "Mechanism of metal ignition in an oxygen flow," *Combustion, Explosion, and Shock*

Waves, vol. 34, no. 1, pp. 44-50, 1998.

- [64] V. Bolobov, "Theory of ignition of metals at fracture," *Combustion, Explosion, and Shock Waves*, vol. 48, no. 6, pp. 689-693, 2012.
- [65] B. Efimov and L. Zaklayz'minskii, "Initiation of combustion of titanium plates in an air stream by pulsed radiation," *Combustion, Explosion, and Shock Waves*, vol. 30, no. 2, pp. 178-182, 1994.
- [66] L. Strakovskii, "Ignition of titanium by means of CO₂ laser radiation," *Combustion, Explosion, and Shock Waves*, vol. 18, no. 5, pp. 96-100, 1982.
- [67] V. Bolobov, "Deflagration of titanium in an oxygen flow," *Combustion, Explosions, and Shock Waves*, vol. 29, no. 2, pp. 12-15, 1993.
- [68] V. Kovalev and V. Mel'nikov, "High temperature oxidation and thermal ignition of titanium and zirconium plates," *Combustion, Explosions, and Shock Waves*, vol. 14, no. 3, pp. 14-21, 1978.
- [69] M. Derevyaga, L. Stesik and E. Fedorin, "Ignition of titanium in oxygen," *Fizika Goreniya i Vzryva*, vol. 12, no. 4, pp. 548-555, 1976.
- [70] P. Hill, D. Adamson, D. Foland and W. Bresette, "High temperature oxidation and ignition of metals," 1956.
- [71] H. Schmidt and D. Forney, "ASRDI Oxygen technology Survey," Washington, D.C., 1975.
- [72] L. Dean and W. Thompson, "Ignition Characteristics of Metals and Alloys," *ARS Journal*, vol. 31, no. 7, pp. 917-923, 1961.
- [73] R. Pape and F. Schmidt, "Combustibility Analysis of Metals," *Advanced Materials and Processes*, pp. 41-44, Nov. 2009.
- [74] A. Breiter, V. Mal'tsev and E. Popov, "Models of metal ignition," *Combustion, Explosions, and Shock Waves*, vol. 13, no. 4, pp. 475-484, 1977.
- [75] A. Zolotko, Y. Vovchuk, V. Shevchuck and N. Poletaev, "Ignition and combustion of dust-gas suspensions," *Combustion, Explosions, and Shock Waves*, vol. 41, pp. 611-621, 2005.
- [76] J. Arulmoli, B. Vu, M. Sung, F. Mohamed and J. Earthman, "Spark production by abrasion of titanium alloys in golf club heads," *Fire and Materials*, vol. 39, no. 2, pp. 119-126, 2015.
- [77] E. Shafirovich, S. Teoh and A. Varma, "Combustion of levitated titanium particles in air," *Combustion and Flame*, vol. 152, pp. 262-271, 2008.
- [78] O. Glotov, "Combustion of Spherical Agglomerates of Titanium in Air. II. Results of Experiments," *Combustion, Explosion, and Shock Waves*, vol. 49, no. 3, pp. 307-319, 2013.
- [79] V. Grachukho, M. Gurevich and M. Savel'ev, "Ignition of isolated titanium particles in oxygen containing media," *Combustion, Explosions, and Shock Waves*, vol. 14, no. 1, pp. 35-41, 1976.
- [80] S. Voyuev, V. Maslov, S. Poletaev, V. Rozenband, E. Chernenko, S. Shmurak and V. Barzykin, "Mechanical activation of titanium powder ignition and combustion," *Combustion, Explosion, and Shock Waves*, vol. 19, no. 3, pp. 18-22, 1983.
- [81] E. Shafirovich and O. Roslyakova, "Influence of grinding of a titanium powder on explosion characteristics of its aerosuspension," *Journal of Engineering Physics and Thermophysics*, vol. 65, no. 4, pp. 945-948, 1993.
- [82] L. Nelson, "Combustion of metal droplets ignited by flash heating," in *Symposium on Combustion*, 1966.
- [83] A. Khomenko, V. Mukasyan, V. Ponomarev, I. Borovinskaya and A. Merzhanov, "Dynamics of phase forming processes in metal-gas system during combustion," *Combustion and Flame*, vol. 92, pp. 201-208, 1993.

- [84] T. Andrzejak, E. Shafirovich and A. Varma, "On the mechanisms of titanium particle reactions in O₂/N₂ and O₂/Ar atmospheres," *Propellants Explosion Pyrotechnology*, vol. 34, pp. 53-58, 2009.
- [85] I. Molodetsky, E. Vicenzi, E. Dreizin and C. Law, "Phases of titanium combustion in air," *Combustion and Flame*, vol. 112, pp. 522-532, 1998.
- [86] National Aeronautics and Space Administration, "Columbia Accident Investigation Report," 2003.
- [87] R. Boyer, "An overview on the use of titanium in the space industry," *Material Science and Engineering:A*, vol. 213, no. 1-2, pp. 103-114, 1996.
- [88] "Columbia Crew Survival Investigation Report," 2008.
- [89] J. Olivas, M. Wright, R. Christoffersen, D. Cone and S. McDaniels, "Crystallographic oxide phase identification of char deposits obtained from space shuttle Columbia window debris," vol. 67, pp. 553-560, 2010.
- [90] J. D. Olivas, B. Mayeaux, P. Melroy and D. Cone, "Study of Ti Alloy Combustion Susceptibility in Simulated Entry Environments," in *AIAA Space 2009 Conference and Symposium*, Pasadena, CA, 2009.
- [91] A. Grosse and J. Conway, "Combustion of metals in oxygen," *Ind. Eng. Chem.*, vol. 50, pp. 663-672, 1958.
- [92] G. Markstein, "Combustion of Metals," *AIAA*, vol. 1, pp. 550-563, 1963.
- [93] G. Lutjering and J. Williams, *Titanium*, 1st ed., Berlin: Springer, 2003, pp. 48-50.
- [94] W. Rochelle, "Survey of Titanium Testing at NASA, DOE, and DOD Test Facilities," 2006.
- [95] E. Borisova and K. Bardanov, "Ignition of Titanium Alloys in Media Containing Oxygen," *Metal Science and Heat Treatment*, pp. 37-40, 1963.
- [96] B. K. P. Efimov, "Influence of the Angle of Attack on the Combustion Characteristics of Titanium Plates in an Airstream," *Combustion, Explosion, and Shock Waves*, vol. 31, pp. 652-654, 1995.
- [97] J. H. D. C. H. M. G. Talkington, "Development of Titanium Weld Color Inspection Tools," *Welding Journal*, pp. 35-38, 2000.
- [98] W. Rochelle, "Suvery of titanium testing at NASA, DOE, and DOD test facilities," 2006.
- [99] I. Kornilov, "Effect of oxygen on titanium and its alloys," *Metal Science and Heat Treatment*, vol. 15, no. 10, pp. 826-829, 1973.
- [100] J. Olivas, B. Mayeaux, P. Melroy and D. Cone, "AIAA Space 2009 Conference and Symposium," in *Study of Ti alloy combustion susceptibility in simulated entry environments*, Pasadena, CA, 2009.
- [101] American Society for Metals, *Atlas of microstructures of industrial alloys*, 8 ed., vol. 7, Metals Park, OH: American Society for Metals, 1972.
- [102] F. Hogue, "Take a closer look at titanium," *The International Metallographic Society Newsletter*, vol. 31, no. 2, pp. 8-9, June 2003.
- [103] A. Paola, M. Bellardita and L. Palmisano, "Brookite, the least known TiO₂ Photocatalyst," *Catalysts*, vol. 3, pp. 36-73, 2013.
- [104] E. Shafirovich, S. Teoh and A. Varma, "Combustion of levitated titanium particles in air," *Combustion and Flame*, vol. 152, pp. 262-271, 2008.
- [105] V. Kovalev and V. Mel'nikov, "High temperature oxidation and thermal ignition of titanium and zirconium plates," *Combustion, Explosion, and Shock Waves*, vol. 14, no. 3, pp. 14-21, 1978.
- [106] G. Lujering and J. Williams, *Titanium*, vol. 1, Berlin: Springer, 2003.
- [107] R. Boyer, G. Welsch and E. Collings, *Materials Properties Handbook: Titanium Alloys*, Materials

Park, OH: ASM International, 1994.

- [108] American Society for Metals, Metals Handbook: Atlas of Microstructures, vol. 7, Materials Park, OH: American Society for Metals, 1972.
- [109] G. Lujering and J. Williams, Titanium, Berlin.
- [110] C. Brooks, Heat Treatment, Structure, and Properties of Nonferrous Alloys, Materials Park, OH: American Society for Metals, 1982.
- [111] A. Smith, J. Buckner, Cone, D.M., C. Bradley and S. Stafford,, "Thermal Alteration and Characterization of Exemplar Space Shuttle Alloy Systems," in *COURI Symposium 2016 Poster Session*, El Paso, TX, 2016.

Appendix A

Permission to include material from Proceedings of MS&T 2015

CONCERNING: Copyright Release

Matt Baker <mbaker@tms.org>

Tue 8/2/2016 5:45 AM Inbox

To: Buckner, Jessica <jlmorris@miners.utep.edu>;

Dear Jessica, Permission is granted to reprint your MS&T paper in the manner described below.
Best regards, Matt Baker

From: Buckner, Jessica [mailto:jlmorris@miners.utep.edu] **Sent:** Tuesday, August 02, 2016 7:44 AM **To:** Matt Baker <mbaker@tms.org> **Subject:** Re: Copyright Release

Hello, No, it does not have a particular connection to ASM. I worded the question in that manner because of the copyright release required upon submission.

I will properly credit the source within the dissertation as you mentioned. If I could just have an email stating plainly that I have this permission.

Thank you for your help!

Regards, Jessica Buckner

Sent from my iPhone On Aug 2, 2016, at 5:34 AM, Matt Baker <mbaker@tms.org> wrote:

Dear Jessica,

Your message below mentions “permission from ASM.” Does your paper have a particular connection to ASM? If not, I can grant you permission to include the paper as a chapter in your thesis. The first page of the chapter should have a credit line that indicates the original source. Please let me know if you have any other questions about this.

RE: Copyright Release - Buckner, Jessica 8/14/16, 11:44 AM

Best regards, Matt Baker

Matt Baker | Content Senior Manager The Minerals, Metals & Materials Society 184 Thorn Hill Road, Warrendale PA 15086

Direct: 724-814-3176 | Fax: 724-814-3177 | Toll Free: 800.759.4TMS (Ext. 280) mbaker@tms.org | <http://www.tms.org>

From: Programming **Sent:** Friday, July 29, 2016 12:28 PM **To:** 'Buckner, Jessica' <jlmorris@miners.utep.edu> **Cc:** Matt Baker <mbaker@tms.org> **Subject:** RE: Copyright Release

Dear Jessica, I am forwarding this email to Matt Baker for assistance. Patricia

Patricia Warren | Programming & Proceedings Specialist The Minerals, Metals & Materials Society 184 Thorn Hill Road, Warrendale PA 15086

Direct: 724-814-3152 | Fax: 724-814-3153 | Toll Free: 800.759.4TMS (Ext. 239)

pwarren@tms.org | <http://www.tms.org>

From: Buckner, Jessica [mailto:jlmorris@miners.utep.edu] **Sent:** Friday, July 29, 2016 11:39 AM **To:** Programming <programming@programmester.org> **Subject:** Copyright Release

Hello, I presented at MS&T 2015 this past October in Columbus, Ohio. When I submitted my paper, I signed the copyright form with my submission. I am trying to use the paper as a chapter in my dissertation, so I will need permission from ASM to do so. Can you please provide this approval, or point me to who can? Email confirmation is sufficient.

I appreciate your help.

Thank you,

Jessica Buckner

Appendix B

Permission to include material from Proceedings of IAASS 2016

Re: IAASS 2016 Submission Questions

Tommaso Sgobba

Mon 8/8/2016 4:45 PM

To: Buckner, Jessica <jlmorris@miners.utep.edu>; Cc: Carmen Felix <carmen.felix.c@gmail.com>;

Dear Jessica, Yes, you are authorized to use your paper as a chapter of your dissertation. Best regards, T. Sgobba

International Association for the Advancement of Space Safety Tommaso Sgobba Executive Director

Kapteynstraat 1 2201BB Noordwijk The Netherlands Phone: +31(0)712020023 Mob. :
+31(0)643552918 <http://iaass.space-safety.org> <http://www.spacesafetymagazine.com>

On Mon, Aug 8, 2016 at 8:49 PM, Buckner, Jessica <jlmorris@miners.utep.edu> wrote: Hello,

I was just checking the status of this. I appreciate your time.

Thank you, Jessica

Sent from my iPhone

On Jul 29, 2016, at 11:30 AM, Carmen Felix <carmen.felix.c@gmail.com> wrote:

Dear Jessica, I don't think there is a problem for you to use it. Tommaso, can you confirm?

Re: IAASS 2016 Submission Questions - Buckner, Jessica 8/14/16, 11:45 AM

Thanks, Carmen

Carmen Felix On Fri, Jul 29, 2016 at 5:34 PM, Buckner, Jessica <jlmorris@miners.utep.edu> wrote:

Hi Carmen,

I presented at IAASS this past May in Melbourne, FL. When I submitted my paper, I signed the copyright form with my submission. I am trying to use the paper as a chapter in my dissertation, so I will need permission from IAASS to do so. Can you please provide this approval, or point me to who can. Email confirmation is sufficient.

I appreciate your help.

Thank you,

Jessica Buckner

Vita

Jessica was born and raised in El Paso, TX. She graduated from Eastwood High School in 2009, finishing 4th in her class, and began courses at El Paso Community College shortly after high school graduation. She began at UTEP in August of 2009 under the Presidential Scholarship. She received her Bachelors in Metallurgical and Materials Engineering in May of 2013 and joined the Ph.D. program in the Materials Science and Engineering department the following August.

As an undergraduate, Jessica participated in undergraduate research in biomedical sciences. As a graduate student, Jessica acted as a teaching assistant for Dr. Stephen Stafford and Dr. Shalayna Smith in support of the Introduction to Materials, Failure Analysis, Advanced Failure Analysis, Composite Materials, and Materials Synthesis and Processing courses. She also functioned as a graduate mentor for undergraduates and research assistant for the Center for Advancement of Space Safety and Mission Assurance Research. Jessica secured funding through the National Science Foundation under the NSF S-STEM grant, the Department of Defense sponsored Science, Mathematics, and Research for Transformation grant, and several private scholarships sponsored by UTEP, local, and international organizations. Jessica completed three summer internships, two with the Air Force Research Laboratory in 2014 and 2016, and one with NASA-White Sands Test Facility in 2015. She presented at multiple international conferences to include Materials Science and Technology 2015, The Minerals, Metals, and Materials Society 2016, and the International Advancement of Space Safety 2016. Jessica published in the Journal of Failure Analysis and Prevention in 2015.

Permanent Address: 11109 Malaguena Ln. NE
Albuquerque, NM, 87111

This thesis/dissertation was typed by Jessica Lynn Buckner.